

Light Curve Analysis of a Young Type II-L Supernova  
KSP-ZN7090 from the KMTNet Supernova Program

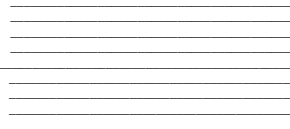
by

Matthew Ching Ho Leung

Supervised by  
Prof. Dae-Sik Moon

April 2022

**B.A.Sc. Thesis**



Division of Engineering Science  
**UNIVERSITY OF TORONTO**

This page intentionally left blank.

# Light Curve Analysis of a Young Type II-L Supernova KSP-ZN7090 from the KMTNet Supernova Program

by

Matthew Ching Ho Leung

Supervised by

Prof. Dae-Sik Moon

A thesis submitted in conformity with the requirements for the degree of  
Bachelor of Applied Science in Engineering Science

Division of Engineering Science  
University of Toronto  
Canada  
April 2022

# Abstract

Supernovae (SNe) play a crucial role in our understanding of the Universe. These fatal stellar explosions have enabled us to explain the origin of the elements and to discover universal expansion. Despite this, we still do not fully understand how SNe explode, largely due to a lack of early observational data for certain types of SNe, in particular for the rare Type II-L subclass. This thesis investigates a young Type II-L SN called KSP-ZN7090, first discovered by the KMTNet Supernova Program on 2020 October 12, less than one day after its explosion. As one of the earliest Type II-L SNe discovered to date, KSP-ZN7090 could offer pivotal natal information on how SNe explode. In this thesis, photometry was conducted in order to construct the multi-band light curves of KSP-ZN7090 and to identify KSP-ZN7090's host galaxy. KSP-ZN7090's temporal parameters, such as its peak epoch and epoch of first light, were estimated using high-order polynomials and power law functions. KSP-ZN7090's bolometric light curve was constructed using blackbody fitting and bolometric corrections, but the latter method gave more reasonable results. Analytic models for the early light curve were used to estimate KSP-ZN7090's physical parameters and to determine the mechanisms behind the early light curve's rise. The results suggest that is likely for KSP-ZN7090's early light curve to be powered primarily by shock cooling emission, rather than radioactive decay. Ultimately, the work in this thesis has added another SN to the limited sample of Type II-L SNe, which, in and of itself, is valuable.

# Acknowledgements

The work in this thesis would not have been possible without the support of many others.

First and foremost, I am deeply grateful to my supervisor, Prof. Dae-Sik Moon, for his continued support and guidance throughout this project. I am grateful to him for the opportunity to work on this project, which has opened a door for me to pursue a future research career in astrophysics. I would like to thank him greatly for all of his invaluable advice and insights during our weekly KSP group meetings and beyond. I would also like to thank him for being accommodating when I moved abroad to Cambridge, MA for an internship.

I would like to extend my sincere thanks to Chris Ni for his advice and help in this project. I thank him for his invaluable insights and for answering all my questions regarding models, code, and other technical problems. His Supernova Analysis Python Package has been useful for PSF photometry and data reduction.

I would like to express my gratitude to Hao Xu for his help and advice in this project, especially with modelling.

I would like to thank Prof. Maria Drout for her invaluable advice and suggestions during our weekly KSP group meetings.

I would also like to thank all my friends, family, and colleagues who have supported me during these times.

Finally, I would like to extend my thanks to the KMTNet staff who acquired the images of KSP-ZN7090, making this project possible.

# Table of Contents

<b>Abstract</b>	<b>i</b>
<b>Acknowledgements</b>	<b>ii</b>
<b>List of Figures</b>	<b>ix</b>
<b>List of Tables</b>	<b>xii</b>
<b>List of Abbreviations</b>	<b>xiii</b>
<b>I Introduction and Background</b>	<b>1</b>
<b>1 Introduction</b>	<b>2</b>
<b>2 Background</b>	<b>4</b>
2.1 Introduction . . . . .	4
2.2 Overview of Core-Collapse Supernovae . . . . .	5
2.2.1 Core-Collapse Supernova Explosion Mechanism . . . . .	5
2.2.2 Core-Collapse Supernova Classes . . . . .	6
2.3 Type II SN Light Curves and Type Classification . . . . .	6
2.3.1 Type II SN Light Curve Phases . . . . .	6
2.3.1.1 Cooling Phase . . . . .	7
2.3.1.2 Plateau Phase . . . . .	7
2.3.1.3 Nebular Phase or Radioactive Tail . . . . .	7
2.3.2 Classifying Type II-L and Type II-P SNe . . . . .	8
2.3.3 Comparing Type II-L and Type II-P SNe . . . . .	9
2.4 The Supernova Problem . . . . .	10
2.5 Research Gap and Significance of KSP-ZN7090 . . . . .	11
2.6 Models for Early Light Curve . . . . .	12

## TABLE OF CONTENTS

---

2.6.1	Analytic Models . . . . .	12
2.6.2	Power Law Models . . . . .	12
2.6.3	Empirical Models . . . . .	14
2.6.4	Choosing which Models to Use . . . . .	14
2.7	Methods to Construct Bolometric Light Curve . . . . .	15
2.7.1	Blackbody Spectrum Fitting and Integration . . . . .	15
2.7.2	Bolometric Corrections . . . . .	16
2.8	Models for Bolometric Light Curve . . . . .	17
2.8.1	Finding Nickel-56 mass . . . . .	18
2.8.1.1	Scaling with SN 1987A . . . . .	18
2.8.1.2	Radioactive Decay-Based Models . . . . .	18
2.8.2	Finding Ejecta Mass and Ejecta Kinetic Energy . . . . .	19
2.8.2.1	Incomplete Trapping of Gamma Rays . . . . .	19
2.8.2.2	Hydrodynamical and Radiative Transfer Models . . . . .	20
2.8.2.3	Analytic Models and Scalings . . . . .	20
2.8.3	Choosing which Models to Use . . . . .	21
2.9	Conclusion . . . . .	21

<b>II</b>	<b>Photometry and Preliminary Analysis</b>	<b>23</b>
-----------	--	-----------

<b>3</b>	<b>Photometry and Light Curve Construction</b>	<b>24</b>
3.1	Overview . . . . .	24
3.2	KMTNet and Observations of KSP-ZN7090 . . . . .	24
3.2.1	About KMTNet . . . . .	24
3.2.2	Overview of Discovery and Observations of KSP-ZN7090 . . . . .	25
3.2.3	Preprocessing by KMTNet . . . . .	26
3.3	Image Subtraction . . . . .	26
3.3.1	Image Subtraction Overview . . . . .	26
3.3.2	Reference Images . . . . .	27
3.4	PSF Photometry . . . . .	28
3.4.1	Brief Overview of Photometry Methods . . . . .	28
3.4.2	Instrumental Flux and Magnitude . . . . .	29
3.4.3	PSF Photometry Process . . . . .	30
3.4.4	Photometric Calibration . . . . .	32
3.4.5	Confirming the Position of KSP-ZN7090 . . . . .	34
3.5	Discarding Bad Quality Images . . . . .	35

## TABLE OF CONTENTS

---

3.5.1	Bad Images due to Sky Conditions . . . . .	36
3.5.2	Bad Images due to Detector Issues and Image Artifacts . . . . .	36
3.6	Light Curve Binning and Image Stacking . . . . .	37
3.6.1	Binning Data before the First Detection . . . . .	37
3.6.2	Binning of Early Data . . . . .	38
3.6.3	Rolling Window Binning . . . . .	39
3.6.4	Results from Binning and Stacking . . . . .	42
3.7	Colour Correction . . . . .	43
3.7.1	Overview of Colour Corrections for KMTNet . . . . .	43
3.7.2	Finding the “offset” term . . . . .	43
3.7.3	Finding the $c$ term . . . . .	45
3.7.4	Applying the Colour Correction . . . . .	46
3.8	Interstellar Extinction Correction . . . . .	47
3.8.1	About Interstellar Extinction . . . . .	47
3.8.2	Correcting Interstellar Extinction . . . . .	47
3.9	Key Results for Photometry and Light Curves . . . . .	50
<b>4</b>	<b>Host Galaxy of KSP-ZN7090</b> . . . . .	<b>52</b>
4.1	Overview . . . . .	52
4.2	The Field around KSP-ZN7090 and its Host Galaxy . . . . .	52
4.3	Fitting to Cropped Rectangular Region Only . . . . .	54
4.3.1	Preliminary Fitting to Cropped Region . . . . .	54
4.3.2	Background Circle Subtraction . . . . .	54
4.4	Fitting and Subtracting Out the Nearby Object with a Moffat Function . . .	56
4.5	Fitting with a Combined PSF . . . . .	57
4.5.1	Moffat and Moffat . . . . .	57
4.5.2	Moffat and Gaussian . . . . .	57
4.6	Fitting with a Binary Star Model . . . . .	58
4.7	Final Results . . . . .	60
<b>5</b>	<b>Preliminary Light Curve Analysis</b> . . . . .	<b>61</b>
5.1	Overview . . . . .	61
5.2	Peak Epoch . . . . .	61
5.3	Early Power Law Fitting . . . . .	64
5.3.1	Single Power Law and Epoch of First Light . . . . .	64
5.3.2	Rise Time . . . . .	65
5.4	KSP-ZN7090 Type Classification . . . . .	65

---

## TABLE OF CONTENTS

---

<b>III Bolometric Light Curve</b>	<b>67</b>
<b>6 Bolometric Light Curve from Blackbody Fitting</b>	<b>68</b>
6.1 Overview . . . . .	68
6.2 Magnitude Definitions . . . . .	68
6.2.1 Magnitudes and Fluxes . . . . .	68
6.2.2 Spectral Flux Density . . . . .	69
6.3 Converting Magnitude to Spectral Flux Density . . . . .	70
6.4 Blackbody . . . . .	71
6.4.1 Planck's Function . . . . .	71
6.4.2 Spectral Flux Density and Planck's Function . . . . .	72
6.4.3 Blackbody Fit . . . . .	72
6.5 Bolometric Flux and Bolometric Luminosity . . . . .	73
6.6 Verifying this Method with the Sun's Parameters . . . . .	74
6.7 Luminosity Distance to KSP-ZN7090 . . . . .	75
6.7.1 The Effect of Universal Expansion . . . . .	76
6.7.2 Comoving Distance . . . . .	77
6.7.3 Luminosity Distance . . . . .	78
6.7.4 Results . . . . .	78
6.8 Blackbody Fitting for KSP-ZN7090 . . . . .	79
6.8.1 Fitting using Nonlinear Least Squares . . . . .	79
6.8.2 Fitting using Monte Carlo Simulations of Nonlinear Least Squares . .	81
6.8.3 Limitations of Blackbody Fitting Method for Finding Bolometric Light Curve . . . . .	82
<b>7 Bolometric Light Curve from Bolometric Corrections</b>	<b>84</b>
7.1 Overview . . . . .	84
7.2 Method of Bolometric Corrections . . . . .	84
7.2.1 Equations . . . . .	84
7.2.2 Uncertainty Estimation . . . . .	85
7.2.3 Light Curve Interpolation . . . . .	85
7.3 A More Complete Description of Light Curve Rise and Phases . . . . .	86
7.3.1 Light Curve Sources . . . . .	86
7.3.1.1 Shock Cooling Emission . . . . .	87
7.3.1.2 Radioactive Decay of $^{56}_{28}\text{Ni}$ . . . . .	87
7.3.2 Three Scenarios for Light Curve Rise . . . . .	87
7.3.2.1 Light Curve Rise Dominated by Shock Cooling Emission . .	87

---

## TABLE OF CONTENTS

---

7.3.2.2	Light Curve Rise Powered by Radioactive Decay Only . . . . .	88
7.3.2.3	Double Peaked Light Curve from both Shock Cooling Emission and Radioactive Decay . . . . .	88
7.4	Phases in the Light Curve of KSP-ZN7090 . . . . .	88
7.4.1	Models to Identify Light Curve Phases . . . . .	88
7.4.2	Results . . . . .	90
7.5	Applying the Bolometric Corrections . . . . .	91
7.5.1	Martinez et al. (2021) Method . . . . .	91
7.5.2	Lyman et al. (2013) Method . . . . .	92
7.5.2.1	Lyman et al. (2013) Cooling Phase, $\xi = x = B, y = V$ . . .	93
7.5.2.2	Lyman et al. (2013) Radiatively-/Recombination-Powered Phase, $\xi = x = B, y = V$ . . . . .	94
7.5.2.3	All Results of Lyman et al. (2013) Bolometric Correction .	95
7.5.3	Comparison and Selection of Results . . . . .	95
7.6	Bolometric Apparent Magnitude to Bolometric Absolute Magnitude and Bolometric Luminosity . . . . .	97
7.6.1	Bolometric Apparent Magnitude to Bolometric Absolute Magnitude .	97
7.6.2	Bolometric Absolute Magnitude to Bolometric Luminosity . . . . .	98
<b>IV</b>	<b>Light Curve Modelling</b>	<b>99</b>
<b>8</b>	<b>Radioactive Decay Powered Rise</b>	<b>100</b>
8.1	Overview . . . . .	100
8.2	Valenti et al. (2007) Model . . . . .	100
8.2.1	The Model . . . . .	100
8.2.2	Method to Fit the Model . . . . .	101
8.3	Fitting the Valenti et al. (2007) to KSP-ZN7090's Bolometric Light Curve .	102
8.3.1	Fitting with Fixed Explosion Time . . . . .	102
8.3.2	Fitting with Explosion Time as Another Fit Parameter . . . . .	103
8.4	Discussion on the Results from the Valenti et al. (2007) Model Fits . . . . .	106
8.4.1	Model Validity and Fit Region . . . . .	106
8.4.2	Comparing the Results to Other Type II-L SNe . . . . .	106
8.5	Rise Time Comparison of SNe with Radioactive Decay Powered Rise . . . . .	107
<b>9</b>	<b>Shock Cooling Emission Powered Rise</b>	<b>109</b>
9.1	Overview . . . . .	109

## TABLE OF CONTENTS

---

9.2	Sapir & Waxman (2017) Model . . . . .	109
9.2.1	Bolometric Luminosity . . . . .	109
9.2.2	Temperature and Blackbody . . . . .	111
9.2.3	Method to Fit the Model to KSP-ZN7090's Light Curve . . . . .	112
9.3	Fitting the Sapir & Waxman (2017) Model to KSP-ZN7090's Light Curve . .	112
9.3.1	Fitting with Fixed Explosion Time . . . . .	113
9.3.1.1	Results of Fit . . . . .	113
9.3.1.2	Contour Plots and Discussion . . . . .	114
9.3.2	Fitting with Explosion Time as Another Fit Parameter . . . . .	115
9.3.2.1	Results of Fit . . . . .	115
9.3.2.2	Contour Plots and Discussion . . . . .	115
9.4	Rise Time Comparison of SNe with Shock Cooling Emission Powered Rise .	118
<b>10</b>	<b>Conclusion</b>	<b>119</b>
10.1	Summary and Significance of Work . . . . .	119
10.2	Future Work . . . . .	121
<b>Bibliography</b>		<b>122</b>

# List of Figures

3.1	False colour RGB image of KSP-ZN7090 . . . . .	25
3.2	How image subtraction is performed . . . . .	27
3.3	Comparison between Gaussian PSF and Moffat PSF fits for a star from a KMTNet image . . . . .	31
3.4	Some reference stars near KSP-ZN7090 . . . . .	33
3.5	Histograms of right ascension and declination coordinates of KSP-ZN7090, from PSF fitting . . . . .	35
3.6	Example of a relatively good quality image of KSP-ZN7090 . . . . .	35
3.7	Examples of bad images of KSP-ZN7090 due to poor sky conditions . . . . .	36
3.8	Examples of bad images of KSP-ZN7090 due to detector issues and image artifacts . . . . .	37
3.9	Effect of lunar illumination on the rough $B$ band light curve . . . . .	39
3.10	Comparison of light curves before and after daily window binning . . . . .	41
3.11	Binned light curves . . . . .	42
3.12	Plot of $m_B - m_V$ versus $m_B - m_{B,\text{inst}}$ for a $B$ band image . . . . .	45
3.13	Colour correction applied to the $B$ band light curve of KSP-ZN7090 . . . . .	46
3.14	Extinction corrected light curves of KSP-ZN7090 . . . . .	49
3.15	Important $B$ band images of KSP-ZN7090 at key epochs . . . . .	50
3.16	Final $BVI$ light curves of KSP-ZN7090 . . . . .	51
4.1	Field around KSP-ZN7090 and its host galaxy . . . . .	53
4.2	Preliminary host galaxy fit with cropped rectangular region . . . . .	54
4.3	Host galaxy fit with cropped rectangular region and subtracted background circle . . . . .	55
4.4	Fitting and subtracting out the nearby object with a Moffat function . . . . .	56
4.5	Fitting a combined Moffat and Gaussian function . . . . .	57
4.6	Fitting a combined Moffat and Gaussian function . . . . .	58
4.7	Fitting a binary star model . . . . .	59

## LIST OF FIGURES

---

5.1	Fitted peaks of KSP-ZN7090's $B$ , $V$ , and $I$ band light curves . . . . .	63
5.2	Single power law fits to KSP-ZN7090's early light curve. $\chi^2/\text{dof} = 0.986$ . . .	65
5.3	$V$ band apparent magnitude light curve of KSP-ZN7090 . . . . .	66
6.1	Fitted blackbody for the Sun using Equation (6.14) . . . . .	74
6.2	Comoving distance $D_c$ and luminosity distance $D_L$ . . . . .	79
6.3	Blackbody fits to KSP-ZN7090 at two different epochs, using nonlinear least squares fitting . . . . .	80
6.4	Blackbody temperature and bolometric luminosity of KSP-ZN7090, using nonlinear least square fitting . . . . .	80
6.5	Blackbody fits to KSP-ZN7090 at two different epochs, using Monte Carlo simulations of nonlinear least squares fitting; compare this with Figure 6.3 .	81
6.6	Blackbody temperature and bolometric luminosity of KSP-ZN7090, using Monte Carlo simulations of nonlinear least square fitting; compare this with Figure 6.4 .	82
7.1	Linearly interpolated light curve for band $x = B$ , interpolated from times of band $\xi = y = V$ . . . . .	86
7.2	Piecewise linear function with 2 sections of constant slope, fitted to the $V$ band light curve of KSP-ZN7090. Comparing with the values in Table 7.1, we can conclude that this fit does not make sense and that the nebular phase is not present in this light curve. . . . .	90
7.3	Bolometric corrections using the cooling phase in Martinez et al. (2021); $\xi = y = V$ , $x = B$ . . . . .	92
7.4	Bolometric corrections using the cooling phase in Lyman et al. (2013); $\xi = x = B$ , $y = V$ . . . . .	93
7.5	Bolometric corrections using the radiatively-/recombination-powered phase in Lyman et al. (2013); $\xi = x = B$ , $y = V$ . . . . .	94
7.6	Comparison of results using bolometric coefficient coefficients in Lyman et al. (2013) . . . . .	95
7.7	Light curve with bolometric absolute magnitudes, based on Figure 7.6b . .	97
7.8	Light curve with bolometric luminosity, based on Figure 7.6b . . . . .	98
8.1	Fit of Valenti et al. (2007) model, with explosion time fixed at 0.191 days before first detection . . . . .	103
8.2	Fit of Valenti et al. (2007) model, with explosion time as a fit parameter, to the first 4 days after first detection. $\chi^2/\text{dof} = 1.721$ . . . . .	104

## LIST OF FIGURES

---

8.3	Fits of Valenti et al. (2007) model, with explosion time as a fit parameter, for the first 6, 10, and 25 days after first detection . . . . .	105
9.1	Fit of Sapir & Waxman (2017) model, with explosion time fixed at 0.191 days before first detection (see Section 5.3), to the first 10 days after first detection of KSP-ZN7090’s <i>B</i> band light curve . . . . .	113
9.2	Contour plots of $\chi^2/\text{dof}$ values when fitting the Sapir & Waxman (2017) model, with explosion time fixed at 0.191 days before first detection, to the first 10 days after first detection of KSP-ZN7090’s <i>B</i> band light curve. . . . .	114
9.3	Fit of Sapir & Waxman (2017) model, with explosion time as a fit parameter, to the first 10 days after first detection of KSP-ZN7090’s <i>B</i> band light curve	115
9.4	Contour plots of $\chi^2/\text{dof}$ values when fitting the Sapir & Waxman (2017) model, with explosion time as a fit parameter, to the first 10 days after first detection of KSP-ZN7090’s <i>B</i> band light curve. . . . .	116
9.5	Fit of Sapir & Waxman (2017) model to the first 10 days after first detection of KSP-ZN7090’s <i>B</i> band light curve, with explosion time as a fit parameter and progenitor radius set to $R_* = 1500R_\odot$ . . . . .	117

# List of Tables

3.1	Images used to construct the reference images . . . . .	28
3.2	AAVSO record numbers of selected APASS reference stars used for photometric calibration of KSP-ZN7090 . . . . .	34
3.3	Values of $A_x/E(B-V)_{\text{SFD}}$ from Table 6 of Schlafly & Finkbeiner (2011), with $R_V = 3.1$ . . . . .	48
3.4	Interstellar extinction in the direction of KSP-ZN7090, from the updated Schlafly & Finkbeiner (2011) dust map with $R_V = 3.1$ . . . . .	48
4.1	Apparent magnitudes of KSP-ZN7090’s host galaxy . . . . .	60
6.1	Zero point spectral flux densities per unit frequency, for the Vega and AB magnitude systems . . . . .	70
6.2	Zero point spectral flux densities per unit wavelength for the Vega system . .	70
6.3	The Sun’s apparent magnitudes, obtained from Table 3 of Willmer (2018) . .	74
6.4	Fitted parameters of blackbody function for the Sun . . . . .	75
6.5	Results of the Sun’s bolometric flux and luminosity values from blackbody fitting . . . . .	75
7.1	Comparison of light curve decline rates for the cooling phase and nebular phase	90
8.1	Results of fitting the Valenti et al. (2007) model to the bolometric light curve of KSP-ZN7090, in the first 4 days after first detection . . . . .	104
8.2	Comparison between some physical parameters of Type II-L SNe and the fitted physical parameters from the Valenti et al. (2007) model . . . . .	107

# List of Abbreviations

Abbreviation	Meaning
AAVSO	American Association of Variable Star Observers
APASS	AAVSO Photometric All-Sky Survey
CCD	Charged-Coupled Device
CCSN(e)	Core Collapse Supernova(e)
CGS	Centimetre-gram-second System of Units
CTIO	Cerro Tololo Inter-American Observatory
decl.	Declination
FWHM	Full Width at Half Maximum
KASI	Korea Astronomy and Space Science Institute
KMTNet	Korea Microlensing Telescope Network
KSP	KMTNet Supernova Program
PREBT	Pre-burst
PRESN	Pre-supernova
PSF	Point Spread Function
R.A.	Right Ascension
RMS	Root Mean Square
RSG	Red Supergiant
SAAO	South African Astronomical Observatory
SBO	Shock Breakout
SDSS	Sloan Digital Sky Survey
SED	Spectral Energy Distribution
SFD	Schlegel et al. (1998) Dust Map
SI	International System of Units
SN(e)	Supernova(e)
SNLS	Supernova Legacy Survey
SSO	Siding Spring Observatory
S&F	Schlafly & Finkbeiner (2011) Dust Map
UTC	Coordinated Universal Time
UV	Ultraviolet
WMAP	Wilkinson Microwave Anisotropy Probe

## Part I

### Introduction and Background

# Chapter 1

## Introduction

Supernovae (SNe) play a crucial role in our understanding of the Universe. These fatal stellar explosions are the origin of most of the elements and have led to the discovery of the accelerated expansion of the Universe (Riess et al. 1998). However, despite their importance, we still do not have a clear picture of how SNe explode. This is largely due to a lack of early observations within a day of the explosions, which could contain pivotal natal information on how SNe explode. In my thesis, I will address this issue by investigating the unprecedentedly early observations of a young Type II-L SN called KSP-ZN7090, which is one of the earliest detected Type II-L SNe to date.

KSP-ZN7090 was first detected on 2020 October 12, less than one day after its explosion, by the Korea Microlensing Telescope Network (KMTNet) Supernova Program (KSP; Moon et al. 2016). KMTNet is a network of three 1.6 m wide-field telescopes located in Australia, Chile, and South Africa, providing 24 hour continuous observations of the southern sky. This continuous monitoring is what enabled KSP-ZN7090 to be among the earliest detected Type II-L SNe to date. Out of all SNe, the Type II-L subclass in particular is rare, accounting for only 6%-10% of all core-collapse SNe (Elias-Rosa et al. 2011). Consequently, the early behaviour of Type II-L SNe has been described as “largely uncharted territory” (Gall et al. 2015) due to a lack of early observational data, thus motivating an investigation into KSP-ZN7090. KSP-ZN7090’s exceptionally early multi-colour observations (in *BVI* bands) are expected to provide novel information on SNe early behaviour.

Hence, the main end goals of this project are to derive KSP-ZN7090’s physical parameters and to provide information on how KSP-ZN7090 evolves during its early phases. This information, in and of itself, is relatively rare and valuable since KSP-ZN7090 is a Type II-L SN. First, I will construct KSP-ZN7090’s *BVI* band light curves (which are plots of the SN’s

brightness over time) from images taken by KMTNet, and then analyze them in order to estimate key temporal parameters such as the SN’s peak epoch and epoch of first light. I will do this by using Monte Carlo simulations to fit the light curves with high-order polynomials (Tartaglia et al. 2021) and power law functions (Gonzalez-Gaitan et al. 2015). From the *BVI* light curves, I will then construct KSP-ZN7090’s bolometric light curve, which is its light curve over all wavelengths. This process will require some iteration since most methods to construct the bolometric light curve have been based on Type II-P SNe, which are much more common. The methods of blackbody fitting (Tartaglia et al. 2021) and bolometric corrections (Lyman et al. 2013; Martinez et al. 2021) will be investigated. After the bolometric light curve is constructed, I will then fit analytic models (e.g. from Valenti et al. (2007) and Sapir & Waxman (2017)) to it, in order to estimate the SN’s explosion parameters and to determine the mechanisms powering the light curve’s rise.

The results of my research will shed light on the physical processes behind the early behaviour of the rare Type II-L subclass of SNe, adding another SN to the limited sample of Type II-L SNe. Collectively, samples of the physical parameters and evolution of Type II-L SNe will provide useful information to constrain models of SNe explosion. Ultimately, the success of my project will be a step forward in understanding how SNe explode and evolve, building onto our knowledge of the Universe.

# Chapter 2

## Background

### 2.1 Introduction

When a massive star reaches the end of its life, it can undergo a spectacular explosion known as a supernova (SN), releasing an enormous amount of energy on a short timescale of hours or days. If close enough to Earth, a SN can appear like a new bright star in the night sky, brighter than an entire galaxy. The topic of this thesis is about a recently discovered Type II-L SN called KSP-ZN7090, first observed by the KMTNet Supernova Program (KSP; Moon et al. 2016) on 2020 October 12. KSP-ZN7090 is an example of a SN that exploded by core-collapse, which is one of the two explosion mechanisms for SNe. Core-collapse SNe (CCSNe) can be divided into several classes based on a SN’s spectrum and light curve, with KSP-ZN7090 belonging to the rare Type II-L subclass. In this chapter, an overview of the current state of SNe research will be given, with a specific focus on CCSNe and the rare Type II-L subclass which KSP-ZN7090 belongs to.

Section 2.2 will provide an overview of the modern interpretation of CCSN explosion mechanism, and will also briefly introduce where the Type II-L subclass fits in among CCSNe. Section 2.3 will discuss about the light curve phases in Type II SNe following the mechanisms in Section 2.2, and will make a comparison between Type II-L and Type II-P SNe. Section 2.4 will discuss about the shortcomings of the modern interpretation of CCSN explosion mechanism, and in particular, how the leading theory is incompatible with Type II-L SN observations due to limited data. Section 2.5 will synthesize the discussions in the previous sections to raise a research gap, and will explain the significance of KSP-ZN7090 and the motivation behind investigating it. The remaining sections will explain and compare different models and methods for Type II SN light curves. Section 2.6 will discuss about models for the early light curve and how a SN’s temporal parameters could be estimated from these.

Section 2.7 will analyze the two main methods in the literature to construct bolometric light curves. Finally, Section 2.8 will discuss about models for the bolometric light curve and how a SN's physical parameters could be estimated from these. These discussions will inform a path forward for investigating KSP-ZN7090.

## 2.2 Overview of Core-Collapse Supernovae

### 2.2.1 Core-Collapse Supernova Explosion Mechanism

Stars support themselves through nuclear fusion, in which lighter nuclei combine to form heavier nuclei, starting from hydrogen. These nuclear reactions are exothermic, releasing energy to create a radially outward pressure gradient in the star, which supports the star against gravitational collapse (Woosley et al. 2002). As a massive star undergoes fusion in its life, heavier elements are produced, and the elements are arranged in a shell-like structure inside the star, with heavier elements in deeper shells (Weaver et al. 1978). This process continues until  $^{56}_{28}\text{Fe}$  forms and an iron core is produced. Now, since  $^{56}_{28}\text{Fe}$  has the highest nuclear binding energy per nucleon, any further reactions to create heavier nuclei are endothermic and hence are impeded (Carroll & Ostlie 2017). At this point, the iron core is supported against gravitational collapse by electron degeneracy pressure. But as more and more iron is produced from fusion, the iron core will reach a critical mass where gravity will overcome electron degeneracy pressure, known as the Chandrasekhar mass (Baron & Cooperstein 1990). At this critical mass, with very high temperatures,  $^{56}_{28}\text{Fe}$  and other nuclei would undergo a process known as photodisintegration or photodissociation, where photons have enough energy to destroy nuclei (Carroll & Ostlie 2017; Couch 2017). At the same time, electron capture processes deprive the iron core of electron degeneracy pressure support (Couch 2017; Janka et al. 2007). As a result, the core begins collapsing rapidly in a runaway process.

The inner iron core collapses and is compressed until it is limited by the repulsive strong nuclear force, which rebounds the falling inner core and sends a shock wave outwards in a process called the “bounce” (Couch 2017). This now outward moving shock wave will crash supersonically into outer material that is still falling down, which stalls the shock wave, becoming an accretion shock (Janka 2012). In a successful SN explosion which is ultimately observable, this stalled shock is able to continue moving outwards through some mechanism. Below the stalled shock, a neutrionosphere develops (Carroll & Ostlie 2017), and it is hypothesized that neutrino energy deposited in the material behind the shock front will allow the shock to continue outwards (Colgate & White 1966). However, this mechanism

is still uncertain, and is an active problem in SNe research which will be elaborated upon in Section 2.4. As the shock continues moving outward, it will also drive the star’s envelope and material outward. Once the shock arrives at the stellar surface and the material becomes optically thin enough, photons will start diffusing outwards and the shock will be visible. This epoch is called shock breakout (SBO), when the first electromagnetic signal from the SN is observable (Martinez et al. 2021).

### 2.2.2 Core-Collapse Supernova Classes

The mechanism by which CCSNe explode as discussed in Section 2.2.1 applies to a wide variety of SNe. All SNe, other than Type Ia SNe which are a product of the thermonuclear explosion of accreting white dwarfs, explode by core-collapse (Turatto 2003). Hence, it is worthwhile to briefly put into perspective where KSP-ZN7090, which is of the rare Type II-L subclass of CCSNe, fits in among CCSNe. Based on a CCSN’s spectrum, a CCSN can be generally classified as either Type II or Type Ib/Ic. Type II SNe show strong hydrogen lines in their spectra, while Type I SNe do not (Carroll & Ostlie 2017). The Type II class generally has two subclasses: II-P and II-L, based on photometric characteristics (Smartt 2009) which will be elaborated upon in Section 2.3.2. There are also two further Type II subclasses: IIIn and IIb, but these are not applicable to KSP-ZN7090. The remainder of this chapter will focus more on Type II-L SNe and the closely-related Type II-P SNe subclass.

## 2.3 Type II SN Light Curves and Type Classification

### 2.3.1 Type II SN Light Curve Phases

Equipped with the knowledge of CCSN explosion mechanism from Section 2.2.1, let us now look at what happens after SBO, when the SN becomes observable. Since the SN is observable, let us consider its light curve, which is a plot of its brightness as a function of time. In particular, this discussion will focus on Type II SNe, but will disregard the Type IIIn and IIb subclasses since they are not applicable for KSP-ZN7090. In general, there are 3 phases for the light curves of Type II SNe: the cooling phase, plateau phase, and nebular phase (Martinez et al. 2021). These different phases can be identified using methods and models from Anderson et al. (2014) and Olivares E. et al. (2010). Note that the description provided here is simplified and for a particular case, and that the mechanisms for each of these phases can actually occur at the same time, producing a variety of light curve shapes. The description here is for Type II SNe with a light curve rise powered mainly by shock cooling emission (also called shock-heated cooling), which is common for most Type II SNe

(Gonzalez-Gaitan et al. 2015). A more complete description is provided later in Section 7.3, and it is encouraged that the reader consult that section.

### 2.3.1.1 Cooling Phase

While the shock described in Section 2.2.1 was moving outwards, it was also depositing energy into the SN's envelope and surrounding material. This heated material will expand and cool, and immediately after SBO, the SN's light curve rises sharply as photons diffuse out of this heated material, which is ejected. Throughout this process in which the heated material is cooling (in which photons are diffusing out of this heated material), the SN's spectrum shifts to longer wavelengths. As a result, after a certain point, the light curve (of a single band) will reach a peak and start to decline. This phase is called the cooling phase (Martinez et al. 2021; Lyman et al. 2013). The mechanism powering the light curve throughout this process is called shock cooling emission, in which photons are diffusing out of cooling material which was heated by the shock (Piro et al. 2021).

### 2.3.1.2 Plateau Phase

Now, most Type II SNe also have a hydrogen-rich envelope. As the shock was moving outwards and depositing energy into the envelope, hydrogen in the envelope was being ionized (Carroll & Ostlie 2017). Over a prolonged period of time, this ionized hydrogen slowly undergoes recombination (Bose et al. 2015b), which reduces the opacity of the material and hence lets radiation pass through (Martinez et al. 2021). As a result, the light curve then has a plateau shape, in a phase called the plateau phase. During this plateau phase, the light curve can also be supplemented by energy released by the ongoing radioactive decay of  $^{56}\text{Ni}$  and other radioactive isotopes produced by the shock front (Carroll & Ostlie 2017; Martinez et al. 2021). Energy released by radioactive decay can ionize the envelope, hence extending the hydrogen recombination process and the duration of the plateau phase (Kasen & Woosley 2009).

### 2.3.1.3 Nebular Phase or Radioactive Tail

After all the hydrogen in the envelope has undergone recombination, the light curve drops and is only powered by radioactive decay, at this point mainly by the decay of  $^{56}\text{Co}$  to  $^{56}\text{Fe}$  (Bose et al. 2015b; Terreran et al. 2016). This  $^{56}\text{Co}$  was produced by the decay of  $^{56}\text{Ni}$ , with the decay scheme  $^{56}\text{Ni} \rightarrow ^{56}\text{Co} \rightarrow ^{56}\text{Fe}$  (Colgate & McKee 1969). The decay reactions are

presented below, from [Carroll & Ostlie \(2017\)](#):



Energy released by radioactive decay in the form of gamma rays (note the  $\gamma$  in the above equations) are deposited into the SN remnant, which is then radiated away. Hence, the derivative of the SN's light curve is proportional to the rate of radioactive decay ([Carroll & Ostlie 2017](#)). This is why the decay of  $^{56}_{27}\text{Co}$  dominates instead of  $^{56}_{28}\text{Ni}$ , since  $^{56}_{28}\text{Ni}$  has a shorter half-life. The decay of  $^{56}_{28}\text{Ni}$  dominates the earlier part of the light curve ([Terreran et al. 2016](#)), hence the contribution to the plateau phase. This phase of the light curve powered by radioactive decay is called the radioactive tail or the nebular phase, and is the last phase of the light curve ([Bose et al. 2015b; Martinez et al. 2021](#)). Note that in some cases, the gamma rays will not be fully trapped and deposited into the SN remnant, and hence the light curve will decline faster and will be steeper than that of  $^{56}_{27}\text{Co}$  decay. This will be discussed further in Section 2.8.2.1.

### 2.3.2 Classifying Type II-L and Type II-P SNe

Historically, Type II SNe have been classified as Type II-P or Type II-L based on the shape of their light curves ([Barbon et al. 1979](#)). Type II-P SNe exhibit a plateau phase, hence the letter “P”. On the other hand, Type II-L SNe do not exhibit a plateau phase or they exhibit a less visible plateau; they exhibit a linear decline from the nebular phase, hence the letter “L”. However, more recent studies with large samples of Type II SNe have suggested that Type II-P and Type II-L SNe are actually the same thing, and that the II-P and II-L subclasses exist along a continuum of Type II SNe ([Anderson et al. 2014; Sanders et al. 2015](#)). As discussed in Section 2.3.1, the plateau phase is due to hydrogen in the envelope. Thus, Type II-L SNe just have less hydrogen in their envelope and therefore a less visible plateau; conversely, Type II-P SNe just have more hydrogen in their envelope and therefore a more visible plateau ([Bose et al. 2015b](#)).

Although Type II-L and Type II-P SNe exist along a continuum, there are differences between them besides just the light curve shape, and these will be elaborated upon in Section 2.3.3. Besides the light curve shape, there are other ways to classify SN in these two subclasses. [Faran et al. \(2014\)](#) distinguishes between Type II-L and Type II-P SNe by photometrically defining a Type II-L SN to be one which has a  $V$  band light curve that declines by more than 0.5 mag from its peak brightness in the first 50 days after its explosion.

Many other authors have also used this definition in order to classify what is a Type II-L SN.

### 2.3.3 Comparing Type II-L and Type II-P SNe

The definition from Faran et al. (2014) was based on the fact that in general, Type II-L SNe have light curves which decline faster than those of Type II-P SNe, as seen from empirical data. Type II-L SNe light curves are also brighter (Smartt 2009). Besides the light curves, there are also differences between the progenitors of these two subclasses. Progenitors of Type II-L SNe usually have a higher mass compared to those of Type II-P SNe, with Type II-L SN progenitors having a mass of at least  $17M_{\odot}$  to  $25M_{\odot}$ , (Woosley et al. 2002; Smartt 2009). CCSNe progenitors have a minimum mass of  $\sim 8M_{\odot}$  (Carroll & Ostlie 2017), and Type II-P SN progenitors have an estimated mass of  $8.5M_{\odot}$  to  $16.5M_{\odot}$  (Smartt et al. 2009), occupying the lower range. In addition, Type II-L SN progenitors have larger radii and less hydrogen compared to those of Type II-P SNe (Terreran et al. 2016). The less hydrogen is consistent with the discussion in Section 2.3.2.

Despite these differences, Type II-L and Type II-P SNe are actually the same thing, as mentioned in Section 2.3.2. It is likely that these differences in progenitor properties are what led to the different light curve shapes between Type II-L and Type II-P SNe. Indeed, simulations have shown that Type II-L and Type II-P SNe are likely both produced by the same explosion mechanism, and that observational differences are due to progenitor parameters such as radius, pre-SN wind, and the amount of hydrogen in the envelope (Blinnikov & Bartunov 1993). It has been proposed that the difference in light curve shapes is due to a single parameter, likely the progenitor's mass (Sanders et al. 2015).

One of the most significant differences between Type II-L and Type II-P SNe is how rare Type II-L SNe are (Smartt 2009). Type II-L SNe account for only 6%-10% of all CCSNe, and are the most poorly studied subclass of CCSNe (Elias-Rosa et al. 2011). To put this into perspective, Type II-P SNe account for about 60% of all CCSNe (Li et al. 2011; Smartt et al. 2009). In particular, the early rise time behaviour of Type II-L SNe has been described as “largely uncharted territory” (Gall et al. 2015). This is what makes KSP-ZN7090 an interesting SN.

## 2.4 The Supernova Problem

Section 2.2.1 provided a brief overview of the modern interpretation of CCSN explosion mechanism. Despite this, we still do not have a definitive picture of how SNe explode, due to questions which still remain regarding how the rebounding shock wave can continue outwards past the infalling outer material and ultimately reach the surface, becoming observable. The problem is that the “bounce” alone does not produce enough energy for this to occur (Smartt 2009). Couch (2017) calls this the “Supernova Problem”, asking how the stalled shock wave could continue moving outwards and ultimately provide observable characteristics. The leading theory for how this is possible is the neutrino mechanism proposed by Colgate & White (1966), briefly touched upon in Section 2.2.1. Most of the energy set free by gravitational collapse of the core is radiated by neutrinos, and if a fraction of this radiated energy can be deposited in the stalled shock, then the shock can continue outwards (Couch 2017; Janka et al. 2007). Neutrino heating increases the pressure behind the shock front, hence driving the shock outwards (Bethe & Wilson 1985).

However, the neutrino mechanism is “still uncertain and controversial” (Janka et al. 2007) because it has not been fully verified with simulations and real observational data. Nevertheless, the neutrino mechanism is the most promising theory so far, and has been the focus of CCSNe research for several decades (Couch 2017). This mechanism was first supported by observations of the canonical SN 1987A (Foglizzo et al. 2015; Smartt 2009), from which a neutrino burst was detected with the Kamiokande II detector (Hirata et al. 1987). Simulations of the neutrino mechanism have been conducted in order to see if they match real observational data, but there have been difficulties in reconciling the simulated observations with real observations. A part of the difficulties is due to the high computational cost in simulating SNe explosions in 2D and 3D (Couch 2017; Foglizzo et al. 2015). 1D simulations, such as from Sukhbold et al. (2016), have been used more often instead, and they are more reliable and consistent with real observations. However, there are still issues, and in general, simulated results of whether an explosion will be ultimately successful and observable are very sensitive to the progenitor star’s physical parameters and structure. 1D simulations of the neutrino mechanism have consistently failed for the lowest mass progenitors (Pejcha 2020), giving results that they would not successfully explode even though they actually do. In addition, simulated results of the neutrino mechanism cannot explain more energetic explosions, and hence some have argued that an alternative mechanism to the neutrino mechanism is necessary (Ugliano et al. 2012).

In particular, simulated observations of the neutrino mechanism are less consistent for Type II-L SNe compared to other types of Type II SNe. Most studies, such as Pejcha (2020), tend to focus on Type II-P SNe instead due to their prevalence. For example, Sukhbold et al. (2016) showed that simulated observations from the neutrino mechanism in 1D are consistent with real observational data for Type II-P SNe, but were inconsistent with Type II-L SNe. They noted that this could “reflect a deficiency in pre-SN modeling” for Type II-L SNe. In addition, they mentioned that Type II-L SNe progenitors have a mass range where rotation and other mechanisms could be important, and that “more study is clearly needed” for Type II-L SNe. Furthermore, since simulated observations cannot explain more energetic explosions (Ugliano et al. 2012), this may be problematic for Type II-L SNe, which are brighter (as discussed in Section 2.3.3) and hence more energetic. These shortcomings in simulated observations are likely because Type II-L SNe are rarer; there is limited observational data from Type II-L SNe which could be used to develop and verify explosion models.

## 2.5 Research Gap and Significance of KSP-ZN7090

From the discussions in the previous sections, we can identify a research gap in the field of SNe astrophysics. As discussed in Section 2.3.3, Type II-L SNe are a rare class of CCSNe. Since they are relatively uncommon, there is less data which could be used to develop models for SNe explosions, compared to more common SNe subclasses such as Type II-P SNe. The results of this are adverse. For example, simulations of the neutrino mechanism (the leading explanation for the “Supernova Problem” in Section 2.4) have failed in particular for Type II-L SNe but not for Type II-P SNe. Furthermore, methods to analyze Type II SNe have mostly focused on the more common Type II-P SNe instead. In order to better understand how SNe explode, there is a need to further investigate Type II-L SNe, as many authors have suggested. Early observations of Type II-L SNe are particularly valuable and less studied because they are rare.

This is where KSP-ZN7090 comes in. KSP-ZN7090 is one of the earliest observed Type II-L SNe to date, being first detected by KMTNet less than one day after its explosion. These early observations of KSP-ZN7090, which were taken in different bands as well ( $B$ ,  $V$ , and  $I$  bands), are particularly rare and valuable, and are expected to provide novel information on SNe evolution. With this motivation, the main end goals of this thesis are to generate and analyze KSP-ZN7090’s light curves (in particular during its early phases) and to estimate KSP-ZN7090’s physical parameters. An investigation into KSP-ZN7090 will add another

SN to the limited sample of Type II-L SNe, which are collectively useful in developing and verifying models of SNe explosion. In the remaining portion of this chapter, methods and models for Type II SN light curves will be discussed.

## 2.6 Models for Early Light Curve

After the *BVI* light curves of KSP-ZN7090 are generated from the raw data (images), the next step is to fit models to the early light curve in order to obtain the SN's temporal parameters. An example of a temporal parameter is the epoch of first light, which is when the SN is first visible after SBO. This parameter is commonly used to describe when the SN exploded. Models of the early light curve should capture the light curve's rise after SBO. There are several types of functions used to fit early light curves of SNe, and these will be discussed in this section.

### 2.6.1 Analytic Models

Analytic models have been developed for the early light curves of SNe, in which luminosity is a function of physical parameters such as ejecta energy, ejecta mass, and progenitor radius. Examples of analytic models for SNe early light curves include Rabinak & Waxman (2011), Nakar & Sari (2010), and Shussman et al. (2016). The former two models are relatively popular for Type II SNe with peaks powered by shock cooling emission. In these analytic models, luminosity has a power law relationship with time. Hence, simplified power law models are often used, as will be discussed in the next section.

### 2.6.2 Power Law Models

A common type of model for the early light curves of SNe are power law models, in which the luminosity  $L$  of the SN is proportional to  $t^n$ , where  $n$  is some power law index. One power law model is the single power law model (e.g. Ben-Ami et al. 2012; Gonzalez-Gaitan et al. 2015; Parrag et al. 2021). Let  $F_\lambda(t)$  be flux of the SN in band  $\lambda$  at time  $t$  after the first observation. The single power law is:

$$F_\lambda(t) = \begin{cases} 0 & \text{if } t < t_0 \\ C_\lambda(t - t_0)^n & \text{if } t \geq t_0 \end{cases} \quad (2.3)$$

where  $t_0$  is the epoch of first light and  $C_\lambda$  is some constant which depends on the band  $\lambda$ . Note that sometimes authors may indicate that they fit a polynomial to the early light curve

(e.g. Gal-Yam et al. 2014), but this is just a power law with  $n \geq 1$ ,  $n \in \mathbb{Z}$ . There are different variants of the single power law, such as one with an additive constant factor (Terreran et al. 2022).

Gonzalez-Gaitan et al. (2015) used Equation (2.3) to fit the early light curves of 223 Type II SNe from the Sloan Digital Sky Survey (SDSS) and the Supernova Legacy Survey (SNLS), in order to determine the epoch  $t_0$  of when the SN exploded. The power law index  $n$  can tell us what physical processes are contributing to the light curve’s rise. For example,  $n \sim 1.5$  for a light curve dominated by shock cooling emission (Piro & Nakar 2013). Gonzalez-Gaitan et al. (2015) found median power indices of  $n = 0.96^{+1.10}_{-0.77}$  and  $n = 0.91^{+1.42}_{-0.59}$  for Type II SNe in SDSS and SNLS respectively. The power indices they found mostly followed  $n \lesssim 1.4$ , implying that most Type II SNe light curves have peaks that are powered by shock cooling emission.

In the case where there are two physical processes contributing to the rise of the early light curve, a double power law model could be used (Shappee et al. 2018). The double power law is:

$$F_\lambda(t) = \begin{cases} 0 & \text{if } t < t_0 \\ C_\lambda(t - t_0)^n & \text{if } t_0 \leq t < t_1 \\ C_\lambda(t - t_0)^n + D_\lambda(t - t_1)^m & \text{if } t \geq t_1 \end{cases} \quad (2.4)$$

where  $n$  and  $m$  are two different power law indices, and  $C_\lambda$  and  $D_\lambda$  are some band-dependent constants. This model builds on the single power model, and here another physical process starts at time  $t_1$ .

Another power law model is a “smooth broken power law”, which combines two power law models with a smoothing parameter. An example of this is the “broken power law” in Zheng et al. (2017), which has the form:

$$F_\lambda(t) = A_\lambda \left( \frac{t - t_0}{t_b} \right)^n \left[ 1 + \left( \frac{t - t_0}{t_b} \right)^{sm} \right]^{-2/s} \quad (2.5)$$

where  $t_b$  is when the break occurs,  $s$  is a smoothing parameter, and  $A_\lambda$  is some band-dependent constant. This, however, is more applicable to Type Ia SNe. Nevertheless, broken power laws could be applicable to some Type II SNe, especially for the later phases, such as in Tartaglia et al. (2021) for the Type II SN 2017ahn.

### 2.6.3 Empirical Models

Another type of model for the early light curves are empirical models, which were created based on actual light curve data points. For example, Bazin et al. (2009) came up with the following model based on 3 years of light curve data from SNLS:

$$F_\lambda(t) = A_\lambda \frac{\exp(-[t - t_0]/\tau_{\text{fall}})}{1 + \exp([t - t_0]/\tau_{\text{rise}})} + B_\lambda \quad (2.6)$$

Here,  $t_0$ ,  $\tau_{\text{fall}}$ ,  $\tau_{\text{rise}}$ ,  $A_\lambda$ , and  $B_\lambda$  are fit parameters. They noted that this model has no physical motivation, but that it is general enough to work for all types of SNe. Empirical models like this, based on actual light curve data from many SNe, are good options for modelling the early light curve. They are relatively less complicated than the analytic models mentioned in Section 2.6.1.

### 2.6.4 Choosing which Models to Use

Given the different types of models in Sections 2.6.1, 2.6.2, and 2.6.3, one may wonder about which model to use for the early light curve of a SN. However, rather than picking one single model, oftentimes authors would use several different models and then compare the results. It is common for authors to first start with the power law models in Section 2.6.2, since they are simpler and also a good approximation for the more complicated analytic models, due to the proportionality relationship between luminosity and time. In particular, the single power law is often used. If the single power law fits fail to capture the early light curve, then fits with other power law models (e.g. double power law or broken power law) could be attempted. After fitting an appropriate power law model to determine the SN's epoch of first light, more complicated models, such as empirical models or analytic models, could be used. The resulting epoch of first light estimates could then be compared and even averaged together. For example, Gonzalez-Gaitan et al. (2015) and Parrag et al. (2021) used the single power law to model the early light curves Type II SNe, and then used the empirical model from Bazin et al. (2009). In addition, Gonzalez-Gaitan et al. (2015) then used analytic models from Rabinak & Waxman (2011) and Nakar & Sari (2010) to fit the early light curves, and then compared the resulting light curve fits from the different models. A similar process could be used when analyzing the early light curves of KSP-ZN7090.

## 2.7 Methods to Construct Bolometric Light Curve

After obtaining the *BVI* light curves of KSP-ZN7090, it is important to generate the SN's bolometric light curve, which is its light curve over all wavelengths. Models can then be fitted to the bolometric light curve in order to estimate the SN's explosion parameters. Two methods which are commonly used in the literature to obtain the bolometric light curve are blackbody fitting and bolometric corrections (Martinez et al. 2021).

### 2.7.1 Blackbody Spectrum Fitting and Integration

Oftentimes, a SN can be modelled as an object that emits blackbody radiation. A SN has a spectrum which is similar to a blackbody spectrum in certain epochs (Fassia et al. 2000). By modelling a SN as a blackbody source, a bolometric light curve can be constructed from the light curve of the SN in several photometric bands. The *BVI* light curves of KSP-ZN7090 can tell us the flux of the SN in the *B*, *V*, and *I* bands. To get its flux over all wavelengths (i.e. its bolometric flux), the following could be done: at each observation epoch, a blackbody function could be fitted to the *BVI* photometric data, and then integrated over all wavelengths to obtain the bolometric flux (Soumagnac et al. 2020; Tartaglia et al. 2021). In other words, for each obervation epoch, a function  $F(\lambda) = AB_\lambda(T)$  is fit to the photometric data at that epoch, where  $B_\lambda(T)$  is the Planck function and  $A$  is some proportionality constant. Then the bolometric flux at that epoch is  $F_{\text{bol}} = \int_0^\infty F(\lambda) d\lambda$ . The bolometric fluxes can then be converted to bolometric luminosities if the redshift (and hence distance) to the SN is known, and thus the bolometric light curve could be obtained.

However, there are some problems and limitations with this method. Firstly, this method works best if there are observations of the SN in a greater number of different bands. If there are more bands, then there are more points to fit the blackbody function at each epoch, and the fit would become more reliable. For example, Soumagnac et al. (2020), Martinez et al. (2021), and Tartaglia et al. (2021) used this method for Type II SNe with observations in 11, 9, and 11 different photometric bands respectively. In the case of KSP-ZN7090, with only observations in 3 bands, the blackbody fit may not be too reliable at times. Martinez et al. (2021) suggests that if there is no extensive photometric coverage over a variety of different bands, then the bolometric corrections method is better. Bolometric corrections will be discussed in Section 2.7.2.

In addition, oftentimes authors in the literature would refer to a bolometric light curve generated by blackbody fitting as “psuedo-bolometric” because they do not integrate the

fitted blackbody function over all wavelengths, but rather only over a certain wavelength range. Some authors may only integrate over the optical and NIR regime, and not the UV range and redder wavelengths (Martinez et al. 2021; Tartaglia et al. 2021). As a result, the luminosities are underestimated, and hence the light curve is called a “pseduobolometric” light curve (Tartaglia et al. 2021). There is a valid reason why this is done though. If the fitted blackbody is integrated over the UV regime, this integration is being performed over an extrapolated region (since light curves are usually given only in optical bands), which may give unreliable results (Fassia et al. 2000). Hence, bolometric light curves from blackbody fitting may be underestimates or unreliable. “Pseudo-bolometric” light curves are still useful though, since they provide a lower limit on the actual bolometric light curve.

Another problem with this method is that a SN is not a perfect blackbody, and hence a blackbody model would not be a good representation for a SN at certain times. At early epochs, a Type II SN can be sufficiently modelled as a blackbody in all optical and NIR bands (Martinez et al. 2021). However, as time goes on, a blackbody is not a good representation of a SN because the SN’s spectrum would become increasingly affected by emission and absorption features (Fassia et al. 2000). At later times, the SN’s spectrum would be unlike a blackbody’s, and blackbody fits would become increasingly poor in quality. For Type II SNe, line blanketing from iron-group elements would cause the SN’s spectrum to deviate from a blackbody spectrum at bluer wavelengths (Martinez et al. 2021). As a result, the bolometric luminosity may be overestimated in this case. Martinez et al. (2021) addressed this line blanketing problem by removing bluer bands from the blackbody fit at later epochs. For Fassia et al. (2000), which was about the Type II SN 1998S, the authors fit a spline instead of a blackbody function to the photometric data  $\gtrsim 30$  days after the SN explosion, due to poor quality in the blackbody fits at these later epochs. More appropriate results for the bolometric luminosity were obtained by integrating the spline. In general, a SN spectrum has the shape of a blackbody spectrum only when  $h\nu \sim k_B T$ , where  $h$  is the Planck constant and  $k_B$  is the Boltzmann constant (Faran et al. 2017).

### 2.7.2 Bolometric Corrections

As mentioned in Section 2.7.1, the method of bolometric corrections may be better if observations are only in a few bands, as in KSP-ZN7090. A bolometric correction is a factor that is applied to a SN’s light curve in a particular single band in order to make it bolometric. From Lyman et al. (2013), a bolometric correction to band  $\xi$  is defined as  $BC_\xi = m_{\text{bol}} - m_\xi$  where  $m_\xi$  is the apparent magnitude of the SN in band  $\xi$ , and  $m_{\text{bol}}$  is the bolometric apparent

magnitude of the SN. From the light curve of a SN in band  $\xi$ ,  $m_\xi$  can be obtained. Hence the bolometric light curve can be obtained with the relationship  $m_{\text{bol}} = BC_\xi + m_\xi$ , if the bolometric correction  $BC_\xi$  is known. The factor  $BC_\xi$  is not just a simple constant, but is often a function of the difference between the apparent magnitudes of different bands. For example, in Lyman et al. (2013), the bolometric correction to the  $B$  band (which is  $BC_B$ ) is a quadratic function of  $m_B - m_I$ , which is the difference in apparent magnitudes between the  $B$  and  $I$  bands.

Bolometric corrections for CCSNe light curves in a particular band can be obtained from the literature, for example from Martinez et al. (2021), Lyman et al. (2013), or Bersten & Hamuy (2009). Authors derived the bolometric corrections from large samples of CCSNe. For example, Martinez et al. (2021) derived bolometric corrections from the light curves of 74 Type II SNe from the Carnegie Supernova Project-I. As more SNe are detected over the years, the bolometric corrections are being revised and updated. Martinez et al. (2021) is one of the more recent publications on bolometric corrections which follows up on earlier work by Lyman et al. (2013) and Bersten & Hamuy (2009).

The bolometric correction  $BC_\xi$  may be different depending on the different SN light curve phases discussed in Section 2.3.1. Lyman et al. (2013) splits up the bolometric corrections into 2 phases: the cooling phase and a “radiatively-/recombination-powered” phase which encompasses the plateau phase and nebular phase in Section 2.3.1. Martinez et al. (2021) splits up the bolometric corrections into the same 3 phases as in Section 2.3.1 (cooling phase, plateau phase, and tail (nebular) phase). In each phase, the bolometric corrections are different.

## 2.8 Models for Bolometric Light Curve

With the bolometric light curve constructed using one of the two methods in Section 2.7, the next step is to fit models to the bolometric light curve in order to estimate the SN’s physical parameters, such as its Nickel-56 mass, ejecta mass, and ejecta kinetic energy. In this section, some prominent examples of bolometric light curve models will be discussed. It is interesting to note that many authors studying Type II-L SNe used methods designed for Type II-P SNe rather than Type II-L SNe, but this is possible to the reasons mentioned in Section 2.3.2.

### 2.8.1 Finding Nickel-56 mass

As discussed in Section 2.3.1, the decay of  $^{56}\text{Ni}$  produces  $^{56}\text{Co}$ , whose decay mainly powers the nebular phase of Type II SN light curves. Hence, from the shape of the bolometric light curve in the nebular phase, the initial mass of the  $^{56}\text{Ni}$  in the ejecta can be estimated. There are several methods to do this, based on different models.

#### 2.8.1.1 Scaling with SN 1987A

One way to find the Nickel-56 mass of the SN is to scale the bolometric light curve of the SN with that of SN 1987A, which was briefly mentioned in Section 2.4. SN 1987A is a peculiar Type II SN (Lyman et al. 2013) and is “one of the most well-studied and well-observed events” (Bose et al. 2015b). The Nickel-56 mass of SN 1987A was  $M_{56\text{Ni},1987\text{A}} = 0.075M_\odot$  (Suntzeff et al. 1991). Given the bolometric luminosity light curve of a SN of interest,  $L_{\text{SN}}(t)$ , and the bolometric luminosity light curve of SN 1987A,  $L_{1987\text{A}}(t)$ , the Nickel-56 mass of the SN could be estimated with the relation:

$$M_{56\text{Ni},\text{SN}} = M_{56\text{Ni},1987\text{A}} \frac{L_{\text{SN}}(t)}{L_{1987\text{A}}(t)} = 0.075M_\odot \frac{L_{\text{SN}}(t)}{L_{1987\text{A}}(t)} \quad (2.7)$$

where  $M_{56\text{Ni},\text{SN}}$  is the estimated Nickel-56 mass of the SN of interest. It is important that the luminosities of SN 1987A and of the SN of interest are compared at the same epoch or at similar phases (Spiro et al. 2014). This should be during the nebular phase. Several authors have used this method to estimate the Nickel-56 mass of SNe. For example, this method was used for the Type II-L SN 2013ej (Bose et al. 2015b), Type II-L SN 2013hj and Type II-L SN 2014G (Bose et al. 2015a), Type II SN 2017ahn (Tartaglia et al. 2021), and for several Type II-P SNe (Spiro et al. 2014). However, Tartaglia et al. (2021) noted that this method assumes full gamma ray trapping in the SN ejecta. In other words, this method assumes that all gamma rays emitted from radioactive decay of  $^{56}\text{Co}$  will be deposited into the ejecta and hence contribute to the light curve. This may not be the case for some SNe if the slope of the light curve is steeper than that of  $^{56}\text{Co}$  decay.

#### 2.8.1.2 Radioactive Decay-Based Models

The Nickel-56 mass of a SN could also be found based on models which account for the radioactive decay of  $^{56}\text{Ni}$  and  $^{56}\text{Co}$  during the nebular phase. For example, Hamuy (2003) gives the Nickel-56 mass  $M_{56\text{Ni}}$  of a SN as:

$$M_{56\text{Ni}} = (7.866 \times 10^{-44}) L_t \exp \left[ \frac{(t_t - t_0)/(1+z) - 6.1}{111.26} \right] M_\odot \quad (2.8)$$

where  $L_t$  is the bolometric tail luminosity of the SN in erg/s,  $t_t$  is the time at which  $L_t$  is measured,  $t_0$  is the explosion epoch,  $z$  is the redshift, 6.1 is the half-life of  $^{56}\text{Ni}$  in days, and 111.26 is the  $e$ -folding time of  $^{56}\text{Co}$  in days. The  $e$ -folding time is just the half-life divided by  $\ln 2$ . Hamuy (2003) derived this formula by investigating 24 Type II-P SNe. This method again assumes that all gamma rays from the decay of  $^{56}\text{Co}$  to  $^{56}\text{Fe}$  are fully trapped and thermalized. This method was used for the Type II-L SNe in Bose et al. (2015b) and Bose et al. (2015a).

Another method for finding the Nickel-56 mass is given by Jerkstrand et al. (2012), which provides a model for the bolometric light curve in the early nebular phase:

$$L_0(t) = (9.92 \times 10^{41}) \left( \frac{M_{56\text{Ni}}}{0.07 M_\odot} \right) \left( \exp \left[ -\frac{t}{111.4} \right] - \exp \left[ -\frac{t}{8.8} \right] \right) \text{ erg/s} \quad (2.9)$$

Here,  $L_0(t)$  is the bolometric luminosity in the early nebular phase, 8.8 is the  $e$ -folding time of  $^{56}\text{Ni}$  in days, and  $t$  is in days. By fitting Equation (2.9) to the bolometric light curve of the nebular phase, the Nickel-56 mass  $M_{56\text{Ni}}$  could be estimated. Equation (2.9) is a theoretical model for the bolometric luminosity which assumes that gamma rays from  $^{56}\text{Co}$  are fully trapped, that there are no other energy sources contributing to the light curve, and that the deposited energy is instantaneously re-emitted (Jerkstrand et al. 2012). Jerkstrand et al. (2012) derived this model for the Type II-P SN 2004et. This method was used by Tartaglia et al. (2021) for the Type II SN 2017ahn and Terreran et al. (2016) for the Type II-L SN 2014G, but with some modifications which will be discussed in Section 2.8.2.1.

## 2.8.2 Finding Ejecta Mass and Ejecta Kinetic Energy

### 2.8.2.1 Incomplete Trapping of Gamma Rays

In Section 2.8.1, methods for finding the Nickel-56 mass were discussed. However, all these methods assumed full trapping of gamma rays from the radioactive decay of  $^{56}\text{Co}$ . If this is not the case, there is another model given by Clocchiatti & Wheeler (1997) that can account for this, which includes the ejecta mass  $M_{\text{ej}}$  and ejecta kinetic energy  $E_{\text{ej}}$  of the SN. If there is incomplete trapping of gamma rays, then the bolometric luminosity of the SN can be modelled by:

$$L(t) = L_0(t) \times (1 - \exp[-\tau_\gamma(t)]) \quad (2.10)$$

where  $\tau_\gamma(t)$  is the optical depth for gamma rays and  $L_0(t)$  is the bolometric luminosity assuming complete gamma ray trapping. With this optical depth factor  $\tau_\gamma(t)$ , incomplete gamma ray trapping could be modelled. Equation (2.9) could be used for  $L_0(t)$  (Tartaglia

et al. 2021; Terreran et al. 2016). Clocchiatti & Wheeler (1997) relates the gamma ray optical depth  $\tau_\gamma(t)$  to a full trapping characteristic timescale  $T_0$  using the relation  $\tau_\gamma(t) = (T_0/t)^{-2}$ . This full trapping characteristic timescale is:

$$T_0 = \sqrt{\frac{C\kappa_\gamma M_{\text{ej}}^2}{E_{\text{ej}}}} \quad (2.11)$$

where  $\kappa_\gamma$  is the opacity for gamma rays,  $M_{\text{ej}}$  is the ejecta mass, and  $E_{\text{ej}}$  is the ejecta kinetic energy.  $C$  is a constant given by  $C = (\eta - 3)^2[8\pi(\eta - 1)(\eta - 5)]^{-1}$ , where  $\eta$  is a number describing the density profile  $\rho(r, t)$  of the ejecta with respect to radius  $r$  and time  $t$ :  $\rho(r, t) \propto [r(t)]^{-\eta}$ . Equation (2.10) could then fitted (along with Equation (2.9) and Equation (2.11) substituted in) to the nebular phase bolometric light curve of a SN in order to estimate its Nickel-56 mass  $M_{56\text{Ni}}$ , ejecta mass  $M_{\text{ej}}$ , and ejecta kinetic energy  $E_{\text{ej}}$ . Some authors who used this method include Tartaglia et al. (2021) for the Type II SN 2017ahn, Terreran et al. (2016) for the Type II-L SN 2014G, and Bose et al. (2018) for the Type II SN ASASSN-15nx. In particular, Terreran et al. (2016) used  $C = 9/40\pi$  for uniform density ( $\eta = 0$ ).

### 2.8.2.2 Hydrodynamical and Radiative Transfer Models

Another method for estimating explosion parameters is with hydrodynamical and radiative transfer models. An example of this is Bersten et al. (2011), which numerically integrates hydrodynamical equations for Type II-P SNe. These types of models are usually more accurate, but they are computationally expensive and time consuming (Bose et al. 2015b). Hence, analytic and semi-analytic models are often used instead.

### 2.8.2.3 Analytic Models and Scalings

Another method for estimating Nickel-56 mass, ejecta mass, and ejecta energy is with analytic scalings and models. Analytic scalings relate a SN's bolometric luminosity to its physical parameters. An example of this is Kasen & Woosley (2009), which gives proportionality relations between the bolometric luminosity and a variety of variables such as explosion energy, ejecta mass, progenitor radius,  $^{56}\text{Ni}$  decay energy, and  $^{56}\text{Co}$  decay energy. From this, the progenitor's parameters could also be estimated.

Analytic models for early light curves, such as Rabinak & Waxman (2011), Nakar & Sari (2010), and Shussman et al. (2016) mentioned in Section 2.6.1, could also be used to estimate the ejecta mass and energy. Another example of an analytic model is Arnett (1980) which

was developed for Type II SNe and discussed by [Gall et al. \(2015\)](#).

Another method is using semi-analytic models, which offer a faster way to get reliable estimates of explosion parameters. One example is [Nagy et al. \(2014\)](#), which is a semi-analytic model for Type II-P SNe based on [Arnett & Fu \(1989\)](#). The method in [Nagy et al. \(2014\)](#) involves numerically solving an ordinary differential equation (ODE) for the temporal component of temperature. This ODE incorporates parameters such as the Nickel-56 mass and internal energy of the SN. This method was used by [Bose et al. \(2015b\)](#) for the Type II-L SN 2013ej.

### 2.8.3 Choosing which Models to Use

Similar to Section 2.6.4, oftentimes it is best to start with the simpler models, then the more complicated ones, and then compare the results. For example, in order to estimate the Nickel-56 mass of Type II SNe, [Tartaglia et al. \(2021\)](#) and [Terreran et al. \(2016\)](#) first used the simple SN 1987A luminosity scaling given by Equation (2.7). The authors then used the bolometric luminosity model from [Jerkstrand et al. \(2012\)](#) (Equation (2.9)) based on radioactive decay with the incomplete gamma ray trapping model from [Clocchiatti & Wheeler \(1997\)](#) (Equations (2.10) and (2.11)) to estimate the Nickel-56 mass, ejecta mass, and ejecta kinetic energy. The Nickel-56 mass they reported for their SNe was an average from these two different methods. A similar approach could be used for KSP-ZN7090.

## 2.9 Conclusion

CCSNe encompass a wide variety of SNe, but their explosion mechanism is not fully understood. For example, there are questions related to how the shock could continue moving outwards after stalling. The leading theory to explain this is the neutrino mechanism, but simulated observations of this are incompatible with the rare Type II-L subclass of CCSNe, due to limited observational data. Hence, many authors have suggested that there is a need to further investigate Type II-L SNe. An investigation into the unprecedentedly early observations of KSP-ZN7090 could shed light on the physical processes behind the early behaviour of Type II-L SNe, knowledge of which are currently limited in the literature. Thus, the end goals of this thesis will be to estimate the physical parameters of KSP-ZN7090, and to construct and analyze its light curves, which are important pieces of information in and of themselves. Collectively, samples of the physical parameters and evolution of Type II-L

## CHAPTER 2. BACKGROUND

---

SNe will provide useful information to constrain models of SNe explosion.

Currently, methods for analyzing the light curves of Type II SNe have focused more on Type II-P SNe. However, more recent studies have shown that Type II-P and Type II-L SNe are actually the same thing, and that Type II SNe exist along a continuum. Hence, a variety of light curve models could be used, even those originally deigned for Type II-P SNe. In order to estimate KSP-ZN7090's temporal parameters, power law models could be first fitted to the early light curve of KSP-ZN7090, and then these could be compared to fits with empirical and analytic models. In order to construct the bolometric light curve of KSP-ZN7090, it may be better to use the bolometric correction method since observations of KSP-ZN7090 were only acquired in 3 bands. However, the blackbody fitting method is also worthwhile since it could provide an estimate of the bolometric light curve, or even a lower limit if a “pseduo-bolometric” light curve is constructed. After KSP-ZN7090's bolometric light curve is constructed, a variety of different models could be fitted to the bolometric light curve in order to estimate KSP-ZN7090's physical parameters. It is best to start with simpler models first, then more complicated ones, and then compare the results. Ultimately, the success of my project will be a step forward in understanding how SNe explode and evolve, building onto our knowledge of the Universe.

## Part II

# Photometry and Preliminary Analysis

# Chapter 3

## Photometry and Light Curve Construction

### 3.1 Overview

In this chapter, photometry will be performed on images of KSP-ZN7090 in order to generate its *BVI* light curves. The purpose of photometry is to measure the amount of light coming from KSP-ZN7090. By doing this for every image of KSP-ZN7090, a light curve can be generated. Section 3.2 will provide an overview of KMTNet’s observations of KSP-ZN7090 and the initial discovery of KSP-ZN7090. Section 3.3 will discuss about image subtraction, which was used to mitigate the effect of nearby sources in KSP-ZN7090’s field when doing photometry. After image subtraction was completed, PSF photometry was conducted on the subtracted images, in Section 3.4. From this process, a rough light curve was generated. In order to improve the quality of the light curve, bad quality images were discarded in Section 3.5, and the light curve was binned using several methods in Section 3.6. Finally, corrections to colour and interstellar extinction were applied to the light curve in Sections 3.7 and 3.8 respectively. The key results from photometry are presented and summarized in Section 3.9.

### 3.2 KMTNet and Observations of KSP-ZN7090

#### 3.2.1 About KMTNet

Let us begin by introducing the Korea Microlensing Telescope Network (KMTNet; Kim et al. 2016), which was used to observe KSP-ZN7090. KMTNet is a network of three wide-field 1.6 m telescopes providing near 24-hour continuous coverage of the southern sky. KMTNet is operated by the Korea Astronomy and Space Science Institute (KASI), with telescopes

located at the Siding Spring Observatory (SSO) in Australia, Cerro Tololo Inter-American Observatory (CTIO) in Chile, and South African Astronomical Observatory (SAAO) in South Africa. These telescopes are each equipped with an identical mosaic CCD camera covering a wide  $2^\circ \times 2^\circ$  field of view. The cameras are 18k by 18k pixels, with  $0.4''/\text{pixel}$  sampling. KMTNet acquires images in  $BVRI$  bands.

### 3.2.2 Overview of Discovery and Observations of KSP-ZN7090

KMTNet's continuous wide-field coverage in several bands makes it suitable for observing rapidly evolving transient objects such as SNe, hence the creation of the KMTNet Supernova Program (KSP; Moon et al. 2016). Between 2020 July 17 and 2020 December 11, KSP observed a  $2^\circ \times 2^\circ$  patch of sky centred at (R.A., decl.) =  $(322^\circ 18' 31''.14, -54^\circ 13' 13''.83)$  (J2000), obtaining 692 images in total in the  $BVI$  bands. All images were taken with 60s exposure time, and the limiting magnitudes were in the range of  $\sim 20.5\text{-}22.5$  mag for a signal-to-noise ratio (SNR) of 3. KSP-ZN7090 was first detected as a new point source in a  $B$  band image taken on 2020 October 12 at 14:44 UTC (MJD = 59134.61389), at the location (R.A., decl.) =  $(322^\circ 45' 45''.72, -53^\circ 55' 49''.91) = (21^{\text{h}} 31^{\text{m}} 3^{\text{s}}.05, -53^\circ 55' 49''.91)$  (J2000). A false colour RGB image of KSP-ZN7090 near its  $I$  band peak is shown in Figure 3.1. At the time of this work, this SN was called KSP-ZN7090 because it was detected in a field which included galaxy NGC 7090.

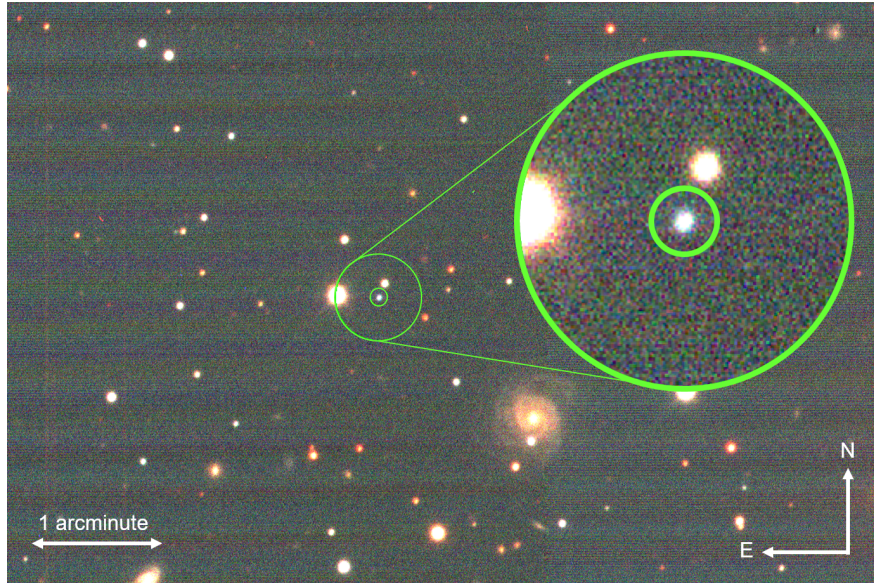


Figure 3.1: False color RGB image ( $R = I$ ,  $G = V$ ,  $B = B$ ) of KSP-ZN7090 taken on 21 October 2020 near the  $I$  band peak. The inset (with radius of  $20''$ ) shows a closer view of the SN, at (R.A., decl.) =  $(21^{\text{h}} 31^{\text{m}} 3^{\text{s}}.05, -53^\circ 55' 49''.91)$  (J2000).

### 3.2.3 Preprocessing by KMTNet

A preprocessing step was applied by KMTNet to the raw images, which included bias subtraction, cross-talk removal, and flat-fielding. Astrometry was then conducted, in which the images were calibrated with the World Coordinate System (WCS) using the SCAMP package (Bertin 2006), using around 10,000 stars from the Guide Star Catalog II (Lasker et al. 2008) in KSP-ZN7090’s field. The resulting astrometric solution from this process typically has a precision of  $0.12''$  (Afsariardchi et al. 2019). Finally, the resulting processed images were saved as FITS files, which are then used by researchers. The remainder of this chapter will discuss about how photometry was conducted on these FITS images, and how light curves were generated from them.

## 3.3 Image Subtraction

### 3.3.1 Image Subtraction Overview

The first step in photometry is to perform image subtraction. As seen in Figure 3.1, the field around KSP-ZN7090 is crowded with other objects. These nearby sources could interfere with photometry of KSP-ZN7090. For example, if there is poorer seeing, then light from a nearby object could spill over to the SN. Hence, it is necessary to subtract out these nearby sources; this process is called image subtraction, in which a reference image taken before the SN explosion is subtracted from a convolved version of each science image. A simplified schematic of the image subtraction process is shown in Figure 3.2. Firstly, a reference image of the field much before the SN explosion is obtained. This image must not contain any signs of the SN. Then, for each science image, a certain point spread function (PSF) is convolved with the science image. This PSF is selected so that the convolved image has stars which have a similar average FWHM value as that of the reference image. Finally, the reference image is then subtracted from the convolved image. If this process was done properly, then all of the non-transient objects should be subtracted out of the image, and only the SN should remain.

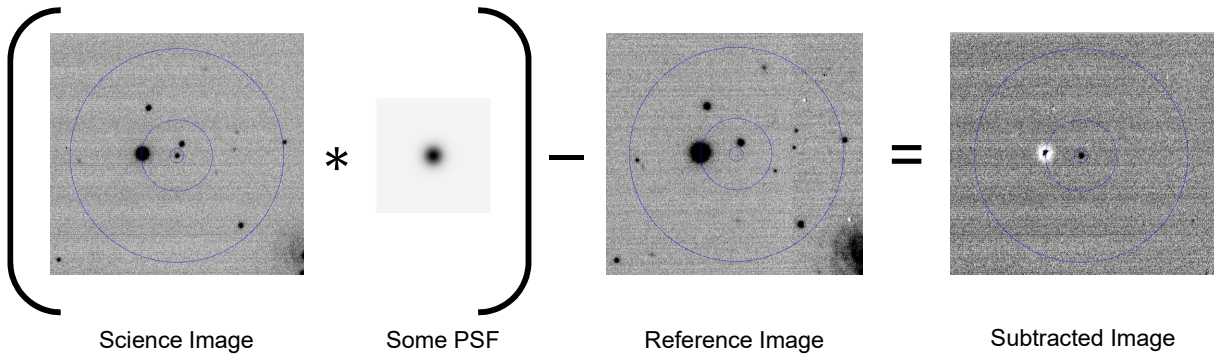


Figure 3.2: How image subtraction is performed: the science image is convolved with some PSF (not to scale in the above image) which is based on the reference image. The reference image is then subtracted from this convolved image. Note that the images here have an inverted colourmap.

Image subtraction was performed using HOTPANTS ([Becker 2015](#)) and WCSREMAP (for astrometric alignment), both software created by Andrew Becker. In order to make this process less computationally expensive, all images were cropped to a radius of 1600 pixels ( $10.66''$ ), centred about the position of KSP-ZN7090, and image subtraction was then applied to these cropped images.

### 3.3.2 Reference Images

The reference image used for image subtraction was specific to each band. Each of the  $B$ ,  $V$ , and  $I$  bands needed a separate reference image. In order to create the reference images, for each band, the 5 images with the best seeing, which were taken at least 3 weeks before the SN explosion, were stacked together. The images were selected so that they did not have any detector issues or image artifacts such as streaks. Stacking was performed using the SWarp program ([Bertin et al. 2002](#)), with a `COMBINE_TYPE` flag of `AVERAGE`. There are several reasons for why a reference image was created by stacking multiple images. Firstly, by stacking multiple images, the reference image will be a good averaged representation of the patch of sky before the explosion. The effect of outliers and artifacts in single images will be less significant if multiple images are used to create the reference image. More importantly, by stacking multiple images, a deeper image could be obtained with a higher limiting magnitude.

In order to determine which images had good seeing, Moffat point spread functions were fitted to selected reference stars within the vicinity of KSP-ZN7090, and the average FWHM of these stars were determined (FWHM calculation for a Moffat point spread function will

be discussed later in Section 3.4.3). The average FWHM was then used as a metric for seeing. Images with a lower average FWHM were considered to have better seeing, since poor seeing causes stars to appear more spread out. For images of KSP-ZN7090, an average FWHM greater than  $\sim 4$  pixels was considered bad seeing. The images used to construct the reference images are shown in Table 3.1. Notice that the average FWHM of each of these images is small.

Band	Time Taken	Telescope	Average FWHM [pixels]
<i>B</i>	2020-07-22 19:28	SSO	2.507616
	2020-09-14 15:16	SSO	2.913344
	2020-07-22 17:24	SSO	3.008146
	2020-07-22 18:31	SSO	3.093844
	2020-07-22 16:25	SSO	3.228569
<i>V</i>	2020-07-22 19:30	SSO	2.489078
	2020-08-13 15:11	SSO	2.506985
	2020-07-22 17:26	SSO	2.608034
	2020-07-31 17:04	SSO	2.885592
	2020-07-22 18:33	SSO	2.935065
<i>I</i>	2020-07-22 19:32	SSO	2.199690
	2020-07-22 17:28	SSO	2.315153
	2020-07-22 18:35	SSO	2.649514
	2020-08-01 15:56	SSO	2.670478
	2020-07-18 17:58	SSO	2.991016

Table 3.1: Images used to construct the reference images

## 3.4 PSF Photometry

### 3.4.1 Brief Overview of Photometry Methods

With image subtraction completed, the next step is to find the apparent magnitude of KSP-ZN7090 in the subtracted images. There are two commonly used methods to do this: aperture photometry and point spread function (PSF) photometry. Both of these methods are used to measure the amount of light coming from an object, which in our case is a SN. To briefly explain, aperture photometry quantifies the brightness of an object by summing the pixel values inside an aperture (typically circular in shape) centred about the object, and then subtracting the sky background, which is estimated by summing the pixels in an annulus centred about the object (Laher et al. 2012). PSF photometry instead fits a PSF to the object, and uses the integrated value of the fitted PSF to quantify the brightness of the

object (Stetson 1987; Anderson & King 2000). Aperture photometry does not work well in the case of crowded fields, which is the case for KSP-ZN7090, as seen in Figure 3.1. Hence, PSF photometry will be used. This section will explain the process of PSF photometry.

### 3.4.2 Instrumental Flux and Magnitude

Suppose that we want to find the apparent magnitude of some object of interest in an image, such as a star. The first step would be to find the instrumental flux  $F_{\text{inst}}$  of the object, which is number of counts on the detector in the instrument which are contributed by the object. Note that this is not the same as the number of photon counts contributed by the object. The instrumental flux is not a useful physical value, except when compared to the instrumental fluxes of other objects in the same image. For example, consider an image which contains two stars called star 1 and star 2. If star 1 has an instrumental flux of  $F_{\text{inst},1} = 100$  and star 2 has an instrumental flux of  $F_{\text{inst},2} = 500$ , then we can only say that star 2 is  $F_{\text{inst},2}/F_{\text{inst},1} = 5$  times brighter than star 1. These numbers, 100 and 500, do not have useful physical meaning though; they are not in the standard units of flux ( $\text{W/m}^2$ ), but are rather just sums of the pixel values on the detector of the instrument.

Suppose our object of interest has an instrumental flux  $F_{\text{inst}}$  with an uncertainty of  $\delta F_{\text{inst}}$ . Then the instrumental magnitude  $m_{\text{inst}}$  of this object is:

$$m_{\text{inst}} = -2.5 \log_{10} (F_{\text{inst}}) \quad (3.1)$$

The uncertainty in the instrumental magnitude is:

$$\begin{aligned} \delta m_{\text{inst}} &= \sqrt{\left(\frac{\partial m_{\text{inst}}}{\partial F_{\text{inst}}}\right)^2 (\delta F_{\text{inst}})^2} \\ &= \left(-2.5 \cdot \frac{1}{(F_{\text{inst}})(\ln 10)}\right) (\delta F_{\text{inst}}) \\ &= -2.5 \log_{10} (e) \cdot \frac{\delta F_{\text{inst}}}{F_{\text{inst}}} \\ \Rightarrow |\delta m_{\text{inst}}| &= \left| 2.5 \log_{10} (e) \cdot \frac{\delta F_{\text{inst}}}{F_{\text{inst}}} \right| \end{aligned} \quad (3.2)$$

The exact definition of magnitudes will be explained in Section 6.2. Like instrumental fluxes, instrumental magnitudes do not have useful physical meaning unless when compared to those of other objects in the same image. Instrumental magnitudes will then be converted

to apparent magnitudes, which have useful physical meaning. This will be discussed in Section 3.4.4.

### 3.4.3 PSF Photometry Process

Let us now find the instrumental flux  $F_{\text{inst}}$  of our object of interest by PSF photometry. In PSF photometry, a PSF is fitted to the object, and then the fitted PSF is integrated over all space. This integrated value is  $F_{\text{inst}}$ . Two commonly used PSFs are a Gaussian function (Stetson 1987) and a Moffat function (Moffat 1969). A Gaussian function, with a background term  $B$ , has the form:

$$f(x, y) = A \exp \left[ -\frac{(x - \mu_x)^2}{2\sigma_x^2} - \frac{(y - \mu_y)^2}{2\sigma_y^2} \right] + B \quad (3.3)$$

where  $A$ ,  $B$ ,  $\mu_x$ ,  $\mu_y$ ,  $\sigma_x$ , and  $\sigma_y$ , are some fit parameters. A Moffat function, with a background term  $B$ , has the form:

$$f(x, y) = A \left[ 1 + \frac{(x - x_0)^2}{\alpha_x^2} + \frac{(y - y_0)^2}{\alpha_y^2} \right]^{-\beta} + B \quad (3.4)$$

where  $A$ ,  $B$ ,  $x_0$ ,  $y_0$ ,  $\alpha_x$ ,  $\alpha_y$ , and  $\beta$  are some fit parameters. In both equations, the term  $B$  could be used to model the sky background. A Moffat PSF is a better model for stars in comparison to a Gaussian PSF, especially for the “wings” of the PSF (Trujillo et al. 2001). An example of this is shown in Figure 3.3, in which a Gaussian PSF and Moffat PSF were both fitted to a star from a KMTNet image. The Moffat PSF is clearly a better model. Moving forward, Moffat PSFs will be used to fit objects.

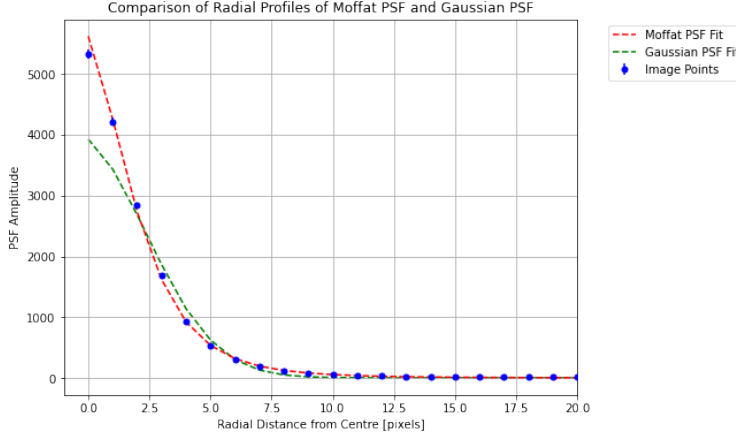


Figure 3.3: Comparison between Gaussian PSF (green curve) and Moffat PSF (red curve) fits for a star (radial points in blue) from a KMTNet image. The Moffat PSF is a better model.

After fitting the object with a Moffat PSF, the instrumental flux  $F_{\text{inst}}$  can be calculated by integrating the fitted Moffat PSF over  $\mathbb{R}^2$ . This is:

$$\begin{aligned}
 F_{\text{inst}} &= \iint_{\mathbb{R}^2} (f(x, y) - b) \, dx \, dy \\
 &= \int_{-\infty}^{\infty} \int_{-\infty}^{\infty} A \left[ 1 + \frac{(x - x_0)^2}{\alpha_x^2} + \frac{(y - y_0)^2}{\alpha_y^2} \right]^{-\beta} \, dx \, dy \\
 &= A \int_{-\infty}^{\infty} \int_{-\infty}^{\infty} \left[ 1 + \frac{x^2}{\alpha_x^2} + \frac{y^2}{\alpha_y^2} \right]^{-\beta} \, dx \, dy \\
 &= A \int_{-\infty}^{\infty} \int_{-\infty}^{\infty} \left[ 1 + \frac{(\alpha_x u)^2}{\alpha_x^2} + \frac{(\alpha_y v)^2}{\alpha_y^2} \right]^{-\beta} \alpha_x \alpha_y \, du \, dv \quad (\text{Let } x = \alpha_x u, y = \alpha_y v) \\
 &= A \alpha_x \alpha_y \int_{-\infty}^{\infty} \int_{-\infty}^{\infty} [1 + u^2 + v^2]^{-\beta} \alpha_x \alpha_y \, du \, dv \\
 &= A \alpha_x \alpha_y \int_0^{2\pi} \int_0^{\infty} [1 + r^2]^{-\beta} r \, dr \, d\theta \quad (\text{Let } r = u^2 + v^2) \\
 &= \dots \\
 &= -\frac{2\pi A \alpha_x \alpha_y (1 + r^2)(r^2 + 1)^{-\beta}}{2(\beta - 1)} \Big|_{r=0}^{\infty} \\
 &= \frac{\pi A \alpha_x \alpha_y}{\beta - 1} \tag{3.5}
 \end{aligned}$$

The uncertainty in  $F_{\text{inst}}$  is then:

$$\delta F_{\text{inst}} = F_{\text{inst}} \sqrt{\left( \frac{\delta \alpha_x}{\alpha_x} \right)^2 + \left( \frac{\delta \alpha_y}{\alpha_y} \right)^2 + \left( \frac{\delta \beta}{\beta} \right)^2 + \left( \frac{\delta A}{A} \right)^2} \tag{3.6}$$

where  $\delta\alpha_x$ ,  $\delta\alpha_y$ ,  $\delta\beta$ , and  $\delta A$  are the uncertainties in the fit parameters  $\alpha_x$ ,  $\alpha_y$ ,  $\beta$ , and  $A$  respectively. The instrumental flux and its associated uncertainty value can then be converted to an instrumental magnitude with an uncertainty value, using Equations (3.1) and (3.2). In addition, the full width at half maximum (FWHM) of the Moffat PSF, which is a useful metric in a variety of situations (e.g. for determining the seeing in Section 3.3.2), can also be found:

$$\begin{aligned} \frac{1}{2}A &= A \left[ 1 + \frac{(\text{FWHM}/2)^2}{\alpha^2} \right]^{-\beta} \\ \left( \frac{1}{2} \right)^{-1/\beta} &= 1 + \frac{(\text{FWHM}/2)^2}{\alpha^2} \\ \alpha^2 \left[ \left( \frac{1}{2} \right)^{-1/\beta} - 1 \right] &= (\text{FWHM}/2)^2 \\ \Rightarrow \text{FWHM} &= 2\alpha\sqrt{2^{1/\beta} - 1} \end{aligned} \quad (3.7)$$

### 3.4.4 Photometric Calibration

As discussed in the previous sections, instrumental magnitudes only have meaning when comparing between objects in the same image. It is necessary to convert instrumental magnitudes to apparent magnitudes, from which a physical flux value with units of  $\text{W/m}^2$  could be determined. This process is called photometric calibration. Let  $m_{\text{app}}$  be the apparent magnitude of the object. Let us define a zero point magnitude  $\text{ZP}_{\text{inst}}$  such that:

$$m_{\text{app}} = m_{\text{inst}} + \text{ZP}_{\text{inst}} \quad (3.8)$$

Hence, if  $\text{ZP}_{\text{inst}}$  is known, then  $m_{\text{inst}}$  can be converted to  $m_{\text{app}}$ . By the way  $\text{ZP}_{\text{inst}}$  is defined here,  $m_{\text{app}} = \text{ZP}_{\text{inst}}$  when  $m_{\text{inst}} = 0$ .

If we know the apparent and instrumental magnitudes of some stars in the image (i.e. we have obtained pairs of points  $(m_{\text{app}}, m_{\text{inst}})$ ), then  $m_{\text{app}}$  can be fitted as a function of  $m_{\text{inst}}$  using Equation (3.8), and hence  $\text{ZP}_{\text{inst}}$  can be found. Thus, in addition to performing Moffat PSF fitting on the object of interest, Moffat PSF fitting also needs to be performed on nearby reference stars present in the image (with known  $m_{\text{app}}$  values) in order to determine their  $m_{\text{inst}}$  values (to generate the  $(m_{\text{app}}, m_{\text{inst}})$  pairs of points). These selected reference stars may be different for different bands. For KSP-ZN7090, photometric calibration was done using 13  $B$  band, 10  $V$  band, and 9  $I$  band reference stars within  $10'$  of KSP-ZN7090. These reference stars were from the American Association of Variable Star Observers (AAVSO)

Photometric All-Sky Survey (APASS) catalog (Henden et al. 2016). The reference stars were selected so that they had apparent magnitudes between 15 and 16 mag, in order to avoid oversaturation issues. In addition, care was taken to make sure that selected reference stars did not have nearby sources, and that they were not binary stars or galaxies. Some of the APASS reference stars are shown in Figure 3.4. The AAVSO record numbers of the selected reference stars which were used for photometric calibration are shown in Table 3.2.

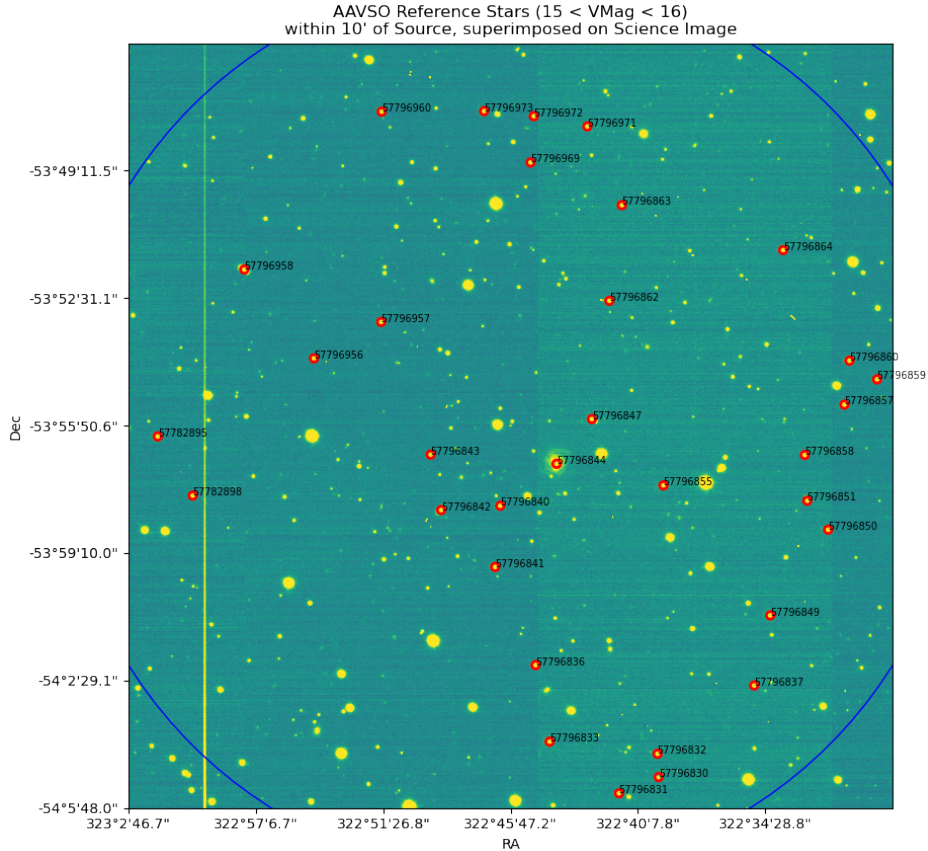


Figure 3.4: Some reference stars near KSP-ZN7090 with  $V$  band apparent magnitudes between 15 and 16 mag, circled in red. Not all of these stars were selected. For example, the object with AAVSO record number 57796844 near the centre of the image is a spiral galaxy.

Band	AAVSO Record Numbers of Selected APASS Reference Stars
$B$	57796833, 57796835, 57796841, 57796852, 57796839, 57796845, 57796861, 57796865, 57796973, 57796964, 57782897, 57782896, 57782891
$V$	57796833, 57796849, 57796841, 57796840, 57782898, 57796973, 57782781, 57782895, 57796957, 57796857
$I$	57782898, 57796840, 57796858, 57796969, 57796972, 57796957, 57796857, 57796922, 57782781

Table 3.2: AAVSO record numbers of selected APASS reference stars used for photometric calibration of KSP-ZN7090. These stars were within a  $10'$  radius of KSP-ZN7090 and had apparent magnitudes of 15 to 16 mag in their corresponding bands.

This process described for PSF fitting and photometric corrections was done for every subtracted image. Following this, an apparent magnitude value for KSP-ZN7090 was obtained for every image, and hence a rough light curve of KSP-ZN7090 was generated. This rough light curve needs further processing, and the steps will be discussed in the following sections.

### 3.4.5 Confirming the Position of KSP-ZN7090

While doing Moffat PSF fitting, notice that  $x_0$  and  $y_0$  in Equation (3.4) were free fit parameters. When a Moffat PSF is fitted to KSP-ZN7090, these two parameters  $x_0$  and  $y_0$  describe the position of KSP-ZN7090. Hence, PSF photometry not only enables us to find the instrumental fluxes and magnitudes of KSP-ZN7090, but also the position of KSP-ZN7090 in every image. A good way to confirm the position of KSP-ZN7090 is to look at histograms of the fitted right ascension (R.A.) and declination (decl.) values of KSP-ZN7090 in all the images. This is shown in Figure 3.5. The mode values of the R.A. and decl. were consistent with KSP-ZN7090's position mentioned in Section 3.2.2, which was (R.A., decl.) =  $(322^\circ 45' 45'' 72, -53^\circ 55' 49'' 91) = (21^h 31^m 3^s 05, -53^\circ 55' 49'' 91)$  (J2000). With this value confirmed, the PSF photometry process for KSP-ZN7090 was repeated but with  $x_0$  and  $y_0$  fixed to this coordinate value (with only  $A$ ,  $B$ ,  $\alpha_x$ ,  $\alpha_y$ , and  $\beta$  as free fit parameters for KSP-ZN7090's Moffat PSF), in order to get more reliable results for flux and magnitude.

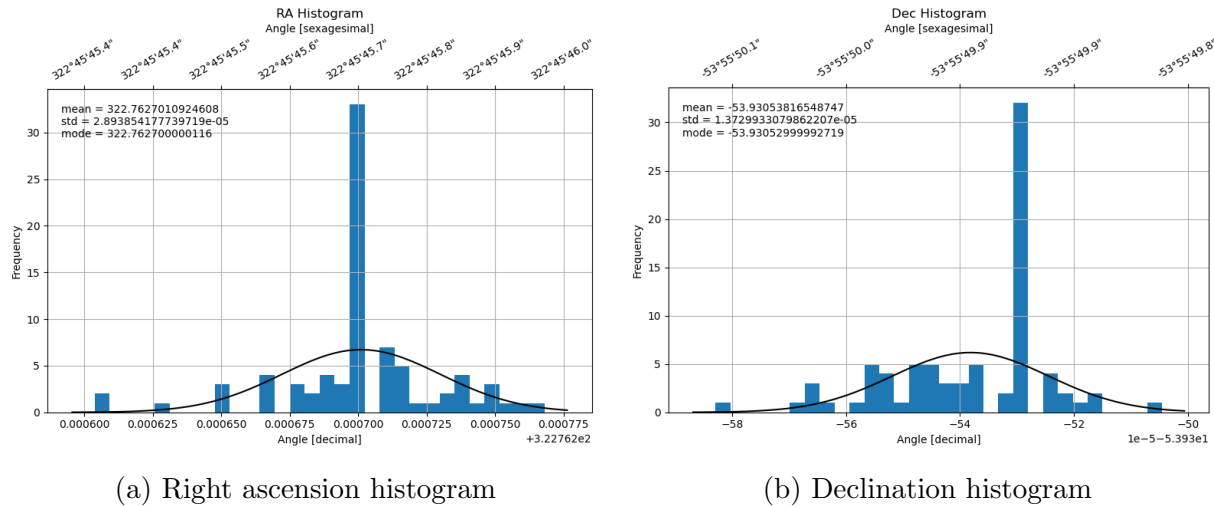


Figure 3.5: Histograms of right ascension and declination coordinates of KSP-ZN7090, from PSF fitting

### 3.5 Discarding Bad Quality Images

After a rough light curve was generated following the PSF photometry process in Section 3.4, every image was inspected. Bad quality images were discarded using qualitative and quantitative metrics. Bad image quality could be due to poor sky conditions, detector issues, or imaging artifacts. An example of a relatively good quality image of KSP-ZN7090 is shown in Figure 3.6. This image was viewed in DS9 ([Joye & Mandel 2003](#)), which was used as a tool to inspect every image.

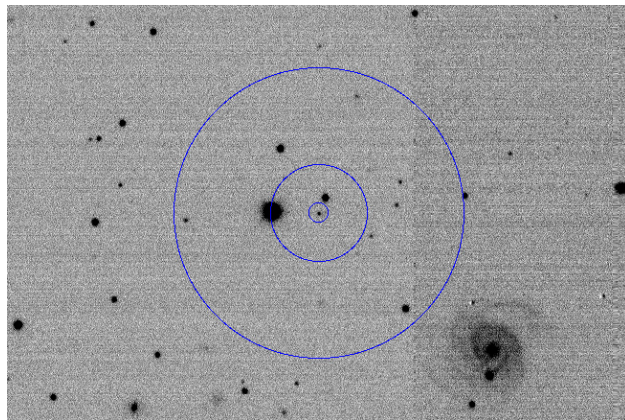
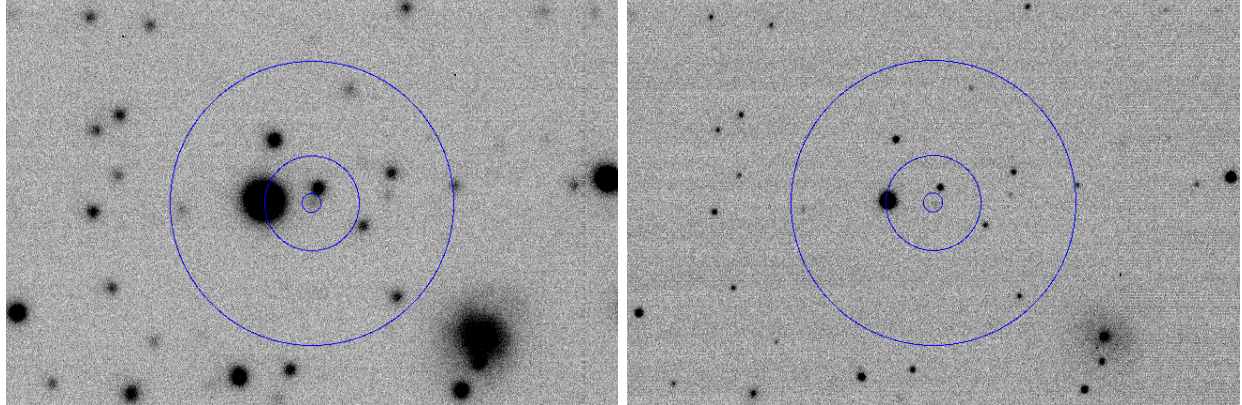


Figure 3.6: Example of a relatively good quality image of KSP-ZN7090, viewed in DS9 with an inverted colourmap. This image was taken in the  $B$  band, on 2020 October 14, 10:36 UTC at SSO. The three blue circles, which are all centred on KSP-ZN7090, have radii of 1', 20'', and 4''.

### 3.5.1 Bad Images due to Sky Conditions

Some images were poor in quality due to poor sky conditions, such as poor seeing or low limiting magnitudes. In order to determine which images had poor seeing, the average FWHM of the selected reference stars was determined (see Equation (3.7)) for each image. The average FWHM was then used as a metric for seeing, as in Section 3.3.2. If an image had an average FWHM greater than  $\sim 4$  pixels, then this image was considered to have poor seeing, and was discarded. An example is shown in Figure 3.7a, where the stars appear “fuzzy” and much more spread out in comparison to Figure 3.6.

In addition to seeing, the limiting magnitude of an image is also important. The limiting magnitude of an image for a certain SNR is the apparent magnitude of the faintest object which can be detected at that SNR. For analysis of KSP-ZN7090, a SNR of 3 will be used. Images with low limiting magnitude are not deep enough, and as a result, fainter objects in these images will not be visible. All images at least 10 days after the first detection with limiting magnitudes below an apparent magnitude of 20.5 mag were discarded. An example of one such image is shown in Figure 3.7b. In this image, the fainter objects and features are not visible, such as the arms of the spiral galaxy at the bottom right of the image.



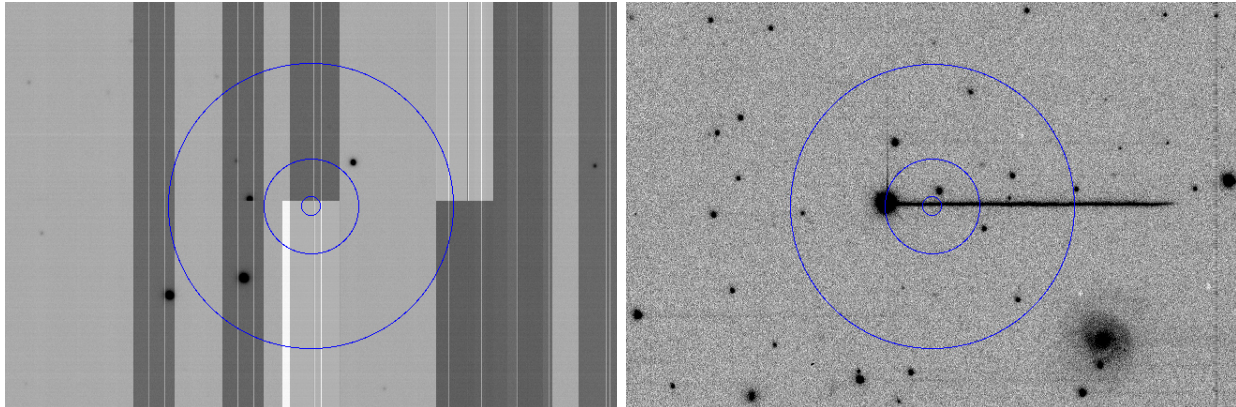
(a) Image with poor seeing (Average FWHM ( $\gtrsim 4$  pixels);  $I$  band image taken on 2020 November 5, 11:23 UTC at SSO) (b) Image with low limiting magnitude ( $\lesssim 20.5$ );  $I$  band image taken on 2020 November 3, 19:32 UTC at SAAO

Figure 3.7: Examples of bad images of KSP-ZN7090 due to poor sky conditions

### 3.5.2 Bad Images due to Detector Issues and Image Artifacts

Some images were poor in quality due to detector issues or image artifacts. For instance, some images had bad pixels and banding effects, which were caused by issues with the CCD detector. An example of this is shown in Figure 3.8a. Some images had image artifacts

such as streaks, an example of which is shown in Figure 3.8b. Some other images had random gradients across the entire image. All of these poor quality images were discarded accordingly.



(a) Image with bad pixels;  $B$  band image taken on 2020 July 31, 15:49 UTC at SSO  
(b) Image with streaks;  $I$  band image taken on 2020 August 1, 16:53 UTC at SSO

Figure 3.8: Examples of bad images of KSP-ZN7090 due to detector issues and image artifacts

## 3.6 Light Curve Binning and Image Stacking

After a rough light curve was constructed and the points corresponding to the bad images were removed, some points in the light curve were binned in order to reduce spread and to improve the quality of data. This was done using two methods: image stacking and rolling window binning.

### 3.6.1 Binning Data before the First Detection

As discussed in Section 3.2.2, KSP-ZN7090 was first detected in an image taken by KMTNet on 2020 October 12, and it was not detected in any single image prior to this date. However, this does not neglect the possibility that KSP-ZN7090 could be visible prior to this date but was just too faint to be observed in single images. It is possible that KSP-ZN7090 is visible in a stacked image made up of images taken before 2020 October 12, which is deeper and has a higher limiting magnitude value. In order to verify if 2020 October 12 is actually the first detection date, data up to 11 days before this supposed first detection date was binned, by stacking images.

Images starting from 2020 October 1 until the supposed first detection date were stacked, again using SWarp (Bertin et al. 2002). For each band on each day, a single stacked image

was created from observations on that day. For example, there were 4  $B$  band images taken on 2020 October 5, and these 4 images were stacked together in SWarp to create one single stacked image; this one single stacked image was then taken to be the  $B$  band observation on 2020 October 5. PSF photometry was then conducted on these stacked images, with the Moffat PSF coordinate fixed at KSP-ZN7090’s position (which was verified in Section 3.4.5). KSP-ZN7090’s apparent magnitude and uncertainty in each stacked image, as well as the limiting magnitude in each stacked image, were computed.

If, in any of these stacked images before the supposed first detection, KSP-ZN7090 had an apparent magnitude value which was less than the limiting magnitude, then this would mean a detection, and hence 2020 October 12 would not actually be the first detection date. However, in all of these stacked images, KSP-ZN7090 had an apparent magnitude which was greater than the limiting magnitude, which went as deep as  $\sim 22$  mag at times. In other words, all of the stacked images had non-detections of KSP-ZN7090. Hence, the 2020 October 12 date mentioned in Section 3.2.2 is indeed the date of the first detection.

While this process did not change any of the results, it helped to verify that the first detection date was indeed correct. In addition, the non-detection limiting magnitudes of the stacked images are a useful component of the light curve. They provide important information and could be used to constrain light curve models. For example, the  $B$  band stacked image for 2020 October 9 (which was a stack of the 3  $B$  band images taken on 2020 October 9) had a limiting magnitude of 22.222 mag. This means that KSP-ZN7090 was not detected up to a  $B$  band magnitude of 22.222 mag on 2020 October 9 (i.e. if KSP-ZN7090 was visible on 2020 October 9, its  $B$  band apparent magnitude must be less than 22.222 mag). Hence, these non-detection limiting magnitudes provide upper limit constraints on the brightness of KSP-ZN7090 before the first detection. Due to their importance, the non-detection limiting magnitudes of several stacked images prior to the first detection are commonly indicated on light curves, with an inverted triangle symbol. Moreover, further stacking of images before the first detection revealed that KSP-ZN7090 has a faint host galaxy, which will be discussed in Chapter 4.

### 3.6.2 Binning of Early Data

In addition to stacking images before the first detection, some images in the first 2 days immediately after the first detection were stacked, up until 2020 October 13. After this day, there was a  $\sim 2$  day gap in observations. While KMTNet provides near 24 hour continuous

coverage of the southern sky, it did not continuously observe the patch of sky containing KSP-ZN7090 only, as there are other observing projects. Specific observing times were allocated, and observations for KSP in the field of KSP-ZN7090 were conducted only at certain concentrated times of the day. For the early data, these concentrated times were  $\sim 2$  to 4 hours in duration, and images of KSP-ZN7090 were taken  $\sim 1$  hour apart in these times. For example, on 2020 October 13,  $B$  band images were taken at 11:27, 12:45, 19:48, 20:59, 21:58, and 22:58. There are two noticeable concentrated time intervals: 11:27 to 12:45, and 19:48 to 22:58. Hence, it is reasonable to stack images together in 4 hour windows, and this was done. Within each of the 4 hour windows, the apparent magnitudes of KSP-ZN7090 in the individual images were similar. Apparent magnitudes of images in different 4 hour windows were dissimilar. This stacking of images in 4 hour windows reduced spread in the early light curve, and allowed for early data with deeper limiting magnitudes. The first detection images were not stacked as they provide valuable data for the earliest part of the light curve.

### 3.6.3 Rolling Window Binning

One problem with the rough light curve was that the data was spread out, in particular for the observations after the peak. Lunar illumination may have contributed to the spread, especially for the later phases of the light curve where there was less data, as in Figure 3.9. It is likely that there were other effects which contributed to this spread in the data, such as variations in sky brightness.

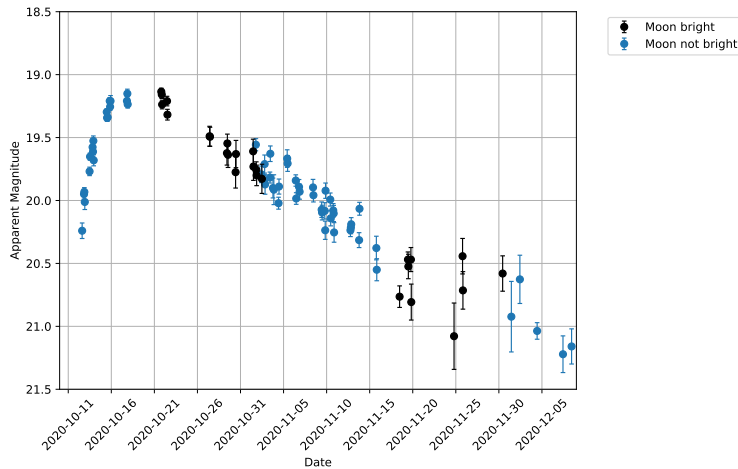


Figure 3.9: Effect of lunar illumination on the rough  $B$  band light curve. Points where the moon is considered “bright” (black points in the figure) are when the moon’s altitude was above  $15^\circ$ , or when the moon’s altitude is above  $0^\circ$  and its distance to KSP-ZN7090 was less than  $90^\circ$ .

In order to reduce spread in the light curve, data after 2020 October 21 (9 days after first detection) was binned with a 24 hour rolling window for each day, using inverse-variance weighting. Rather than weighting the magnitude values, the flux values are weighted. This is because magnitudes are just a logarithmic scale representation of fluxes, and so we should work with the original quantity of flux. Suppose that in a certain 24 hour window, there are  $N$  observations with apparent magnitudes of  $m_1 \pm \delta m_1, \dots, m_i \pm \delta m_i, \dots, m_N \pm \delta m_N$ . Each  $m_i \pm \delta m_i$  value was converted back to a flux value of  $F_i \pm \delta F_i$  using:

$$F_i = 10^{-m_i/2.5} \quad (3.9)$$

$$\delta F_i = \frac{(F_i \ln 10)(\delta m_i)}{2.5} \quad (3.10)$$

These are just rearranged versions of Equations (3.1) and (3.2). Then a weighted mean of the resulting flux values  $F_1 \pm \delta F_1, \dots, F_i \pm \delta F_i, \dots, F_N \pm \delta F_N$  was calculated. The variance was taken as the square of the flux uncertainty  $\delta F_i$ . The weighted mean flux  $F_{\text{avg}}$  and its associated uncertainty  $\delta F_{\text{avg}}$  is:

$$F_{\text{avg}} = \frac{\sum_{i=1}^N (F_i / [\delta F_i]^2)}{\sum_{i=1}^N (1 / [\delta F_i]^2)} \quad (3.11)$$

$$\delta F_{\text{avg}} = \sqrt{\frac{1}{\sum_{i=1}^N (1 / [\delta F_i]^2)}} \quad (3.12)$$

Finally, the weighted mean apparent magnitude  $m_{\text{avg}}$  and its associated uncertainty  $\delta m_{\text{avg}}$  can be obtained from  $F_{\text{avg}}$  and  $\delta F_{\text{avg}}$ :

$$m_{\text{avg}} = -2.5 \log_{10} F_{\text{avg}} \quad (3.13)$$

$$\delta m_{\text{avg}} = \frac{2.5(\delta F_{\text{avg}})}{F_{\text{avg}}(\ln 10)} \quad (3.14)$$

These two equations are analogous to Equations (3.1) and (3.2). This inverse-variance weighting was applied to every 24 hour window. Daily rolling window binning greatly helped to smooth out the light curve, as shown in Figure 3.10. The error bars of the binned points are also smaller, as expected from Equation (3.12).

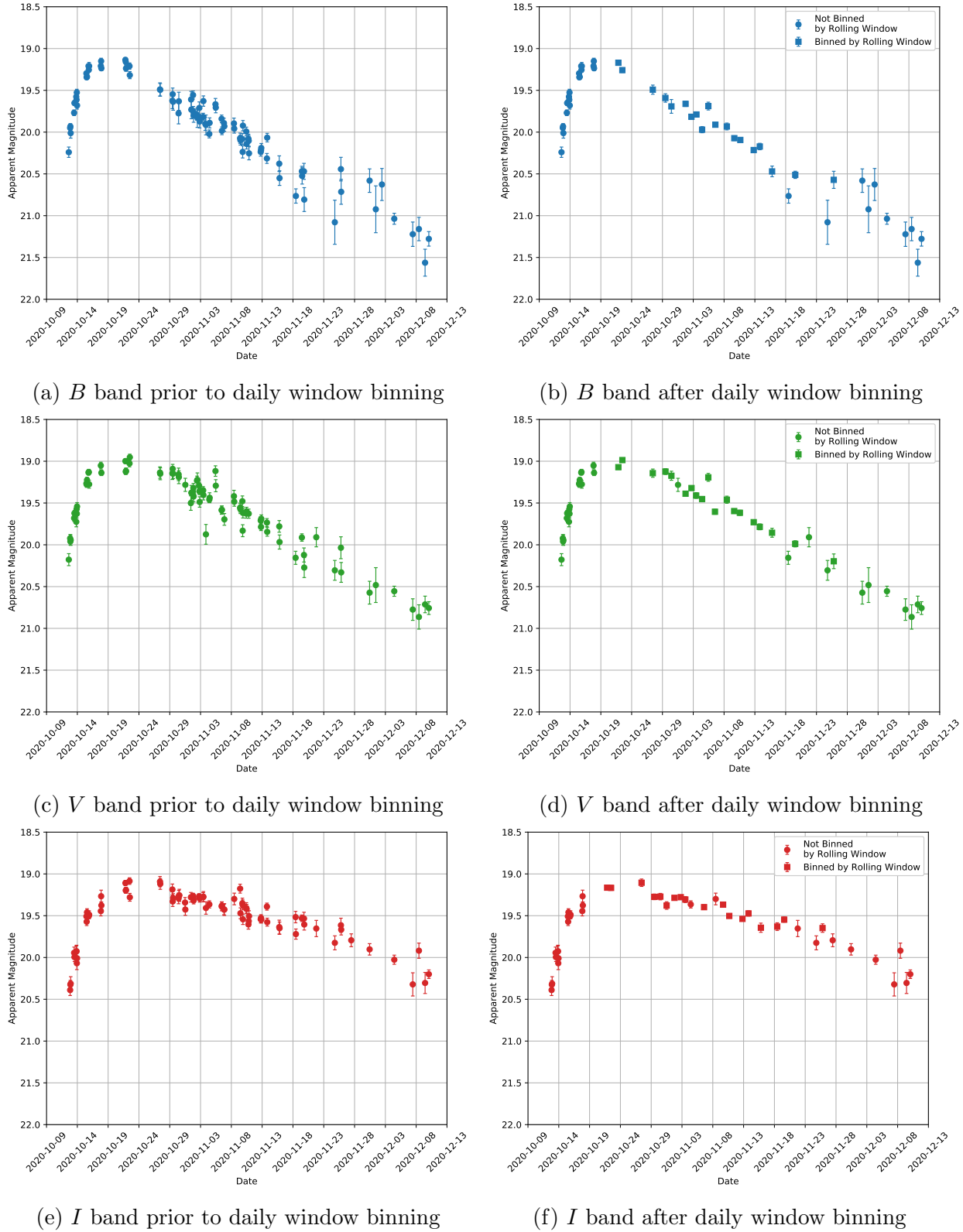


Figure 3.10: Comparison of light curves before and after daily window binning

### 3.6.4 Results from Binning and Stacking

The results from binning and stacking following the procedures in Sections 3.6.1, 3.6.2, and 3.6.3 are shown in Figure 3.11. The orange inverted triangle points correspond to the binned data before the first detection from Section 3.6.1. The square data points up until 2020 October 13 correspond to early data which were stacked, from Section 3.6.2. The square data points after 2020 October 21 correspond to data binned by a daily rolling window, from Section 3.6.3.

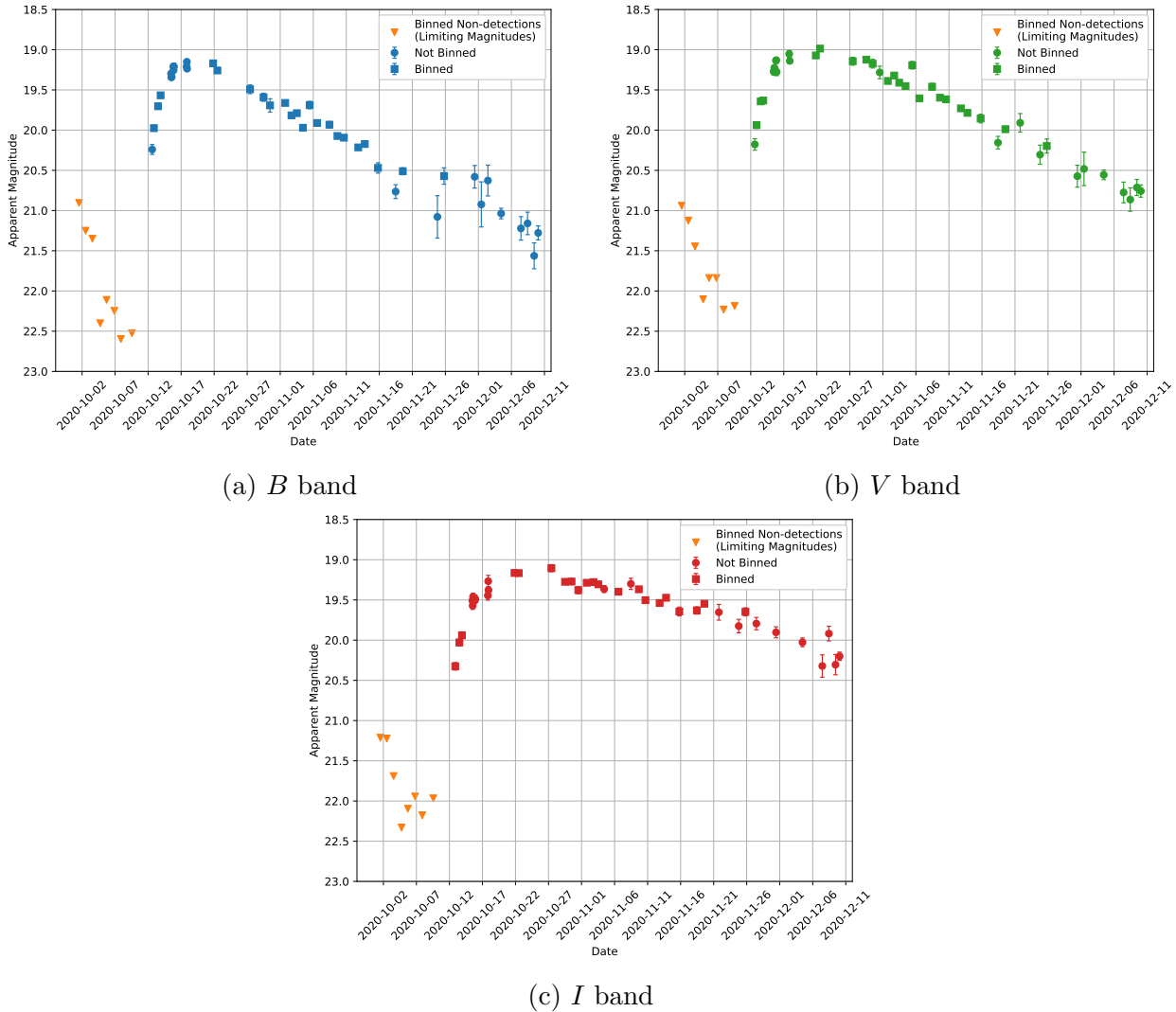


Figure 3.11: Binned light curves of KSP-ZN7090 following the procedures in Sections 3.6.1, 3.6.2, and 3.6.3

## 3.7 Colour Correction

### 3.7.1 Overview of Colour Corrections for KMTNet

Next, colour corrections were performed on the light curves in Section 3.6.4. KMTNet’s *BVI* filter system is non-standard, and differs from AAVSO’s *BVi* filter system. The KMTNet filters have a more “flat” transmission profile which is rectangular in shape. Hence, some of the computed magnitude values must be corrected. While KMTNet’s *V* band and AAVSO’s *V* band both correspond to the standard Johnson *V* band, and KMTNet’s *I* band and AAVSO’s *i* band both correspond to the Sloan *i* band (Moon et al. 2021). A simple linear correction could be made for the *V* and *I* bands, and the photometric calibration discussed in Section 3.4.4 is sufficient. However, KMTNet’s *B* band is different from the standard Johnson *B* band used by AAVSO, and a correction is required which depends on the apparent magnitude difference between the *B* and *V* bands. The *V* and *I* bands require no correction.

Let  $m_{B'}$  be the uncorrected KMTNet *B* band apparent magnitude, and let  $m_B$  be the corrected *B* band apparent magnitude which is consistent with the standard Johnson *B* band used by AAVSO. Let  $m_V$  be the *V* band apparent magnitude. In order to correct the KMTNet *B* band apparent magnitude  $m_{B'}$ , we define a term  $\Delta m_B \equiv m_B - m_{B'}$  which must be added to  $m_{B'}$  so that the corrected *B* band apparent magnitude is  $m_B = m_{B'} + \Delta m_B$ . Park et al. (2017) gives  $\Delta m_B$  as:

$$\Delta m_B = m_B - m_{B'} = c(m_B - m_V) + \text{offset} \quad (3.15)$$

where  $c$  and “offset” are some constants. Moving forward, let us label the uncorrected values with a prime symbol, and the corrected values without a prime symbol. Note that the *V* band apparent magnitude  $m_V$  was not labelled with a prime symbol, because corrections are not required for the *V* band, and hence this is already a “corrected” magnitude.

### 3.7.2 Finding the “offset” term

Now, let us find the value of “offset” in Equation (3.15). First, recall that the zero point magnitude  $ZP_{\text{inst}}$  for photometric calibration in Section 3.4.4 can be found by fitting pairs of points  $(m_{\text{app}}, m_{\text{inst}})$  of the reference stars to Equation (3.8), which was  $m_{\text{app}} = m_{\text{inst}} + ZP_{\text{inst}}$ . Hence, we can say that  $ZP_{\text{inst}} = \langle m_{\text{app}} - m_{\text{inst}} \rangle$ . That is,  $ZP_{\text{inst}}$  is the weighted average of  $m_{\text{app}} - m_{\text{inst}}$  for the reference stars, weighted based on the uncertainties. Therefore, for the

$B$  band, the zero point  $ZP_{B,\text{inst}}$  is:

$$ZP_{B,\text{inst}} = \langle m_{B,\text{ref}} - m_{B,\text{ref,inst}} \rangle \quad (3.16)$$

where  $m_{B,\text{ref,inst}}$  is the  $B$  band KMTNet instrumental magnitude of a  $B$  band reference star (i.e. a reference star from the first row of Table 3.2), and  $m_{B,\text{ref}}$  is its apparent magnitude, which was obtained from AAVSO APASS. Here, the weighted average is being taken over all  $B$  band reference stars. These  $m_{B,\text{ref}}$  values here are already corrected since they were from AAVSO, and hence there is no prime symbol here. Now suppose that we have the  $B$  band instrumental magnitude of any object, which we will call  $m_{B,\text{inst}}$ . Then, from Equation (3.8), this object's uncorrected  $B$  band apparent magnitude is:

$$m_{B'} = m_{B,\text{inst}} + ZP_{B,\text{inst}} = m_{B,\text{inst}} + \langle m_{B,\text{ref}} - m_{B,\text{ref,inst}} \rangle \quad (3.17)$$

where Equation (3.16) was substituted for  $ZP_{B,\text{inst}}$ . Equation (3.17) can then be substituted into Equation (3.15) to obtain:

$$m_B - (m_{B,\text{inst}} + \langle m_{B,\text{ref}} - m_{B,\text{ref,inst}} \rangle) = c(m_B - m_V) + \text{offset} \quad (3.18)$$

Now, note that Equation (3.18) holds true for any object with corrected  $B$  band apparent magnitude  $m_B$ , instrumental magnitude  $m_{B,\text{inst}}$ , and  $V$  band apparent magnitude  $m_V$ . Hence, let us use an object with a corrected  $B$  band apparent magnitude which is equal to the average  $B$  band apparent magnitude of the  $B$  band AAVSO reference stars; that is, let us use  $m_B = \langle m_{B,\text{ref}} \rangle$ . Then  $m_V$  is equal to the average  $V$  band apparent magnitude of the  $B$  band AAVSO reference stars (i.e.  $m_V = \langle m_{V,\text{ref}} \rangle$ ), and  $m_{B,\text{inst}}$  is equal to the average  $B$  band instrumental magnitude of the  $B$  band AAVSO reference stars (i.e.  $m_{B,\text{inst}} = \langle m_{B,\text{ref,inst}} \rangle$ ). Substituting these into Equation (3.18), we obtain:

$$\begin{aligned} m_B - (m_{B,\text{inst}} + \langle m_{B,\text{ref}} - m_{B,\text{ref,inst}} \rangle) &= c(m_B - m_V) + \text{offset} \\ \langle m_{B,\text{ref}} \rangle - (\langle m_{B,\text{ref,inst}} \rangle + \langle m_{B,\text{ref}} - m_{B,\text{ref,inst}} \rangle) &= c(\langle m_{B,\text{ref}} \rangle - \langle m_{V,\text{ref}} \rangle) + \text{offset} \\ \langle m_{B,\text{ref}} \rangle - (\langle m_{B,\text{ref,inst}} \rangle + \langle m_{B,\text{ref}} \rangle - \langle m_{B,\text{ref,inst}} \rangle) &= c\langle m_{B,\text{ref}} - m_{V,\text{ref}} \rangle + \text{offset} \\ 0 &= c\langle m_{B,\text{ref}} - m_{V,\text{ref}} \rangle + \text{offset} \\ \Rightarrow \text{offset} &= -c\langle m_{B,\text{ref}} - m_{V,\text{ref}} \rangle \end{aligned} \quad (3.19)$$

Hence, the “offset” term is equal to  $-c$  times the average  $B - V$  colour difference of the  $B$  band AAVSO reference stars. By calculating a weighted average of the  $B - V$  colour

difference of the  $B$  band AAVSO reference stars (the stars in the first row of Table 3.2),  $\langle m_{B,\text{ref}} - m_{V,\text{ref}} \rangle$  was found to be  $\langle m_{B,\text{ref}} - m_{V,\text{ref}} \rangle = 0.783 \pm 0.058$  mag.

### 3.7.3 Finding the $c$ term

The  $c$  term can be found by fitting magnitude values of reference stars to Equation (3.15). By doing this, Park et al. (2017) found that  $c \approx 0.27$ . Objects in the images containing KSP-ZN7090 also had this value. An example of this is shown in Figure 3.12, which is a plot of  $m_B - m_V$  versus  $m_B - m_{B,\text{inst}}$  for some reference stars within 15' of KSP-ZN7090, for a  $B$  band image taken on 2020 October 12 20:54. The resulting  $c$  value was 0.266, which is consistent with the value from Park et al. (2017).

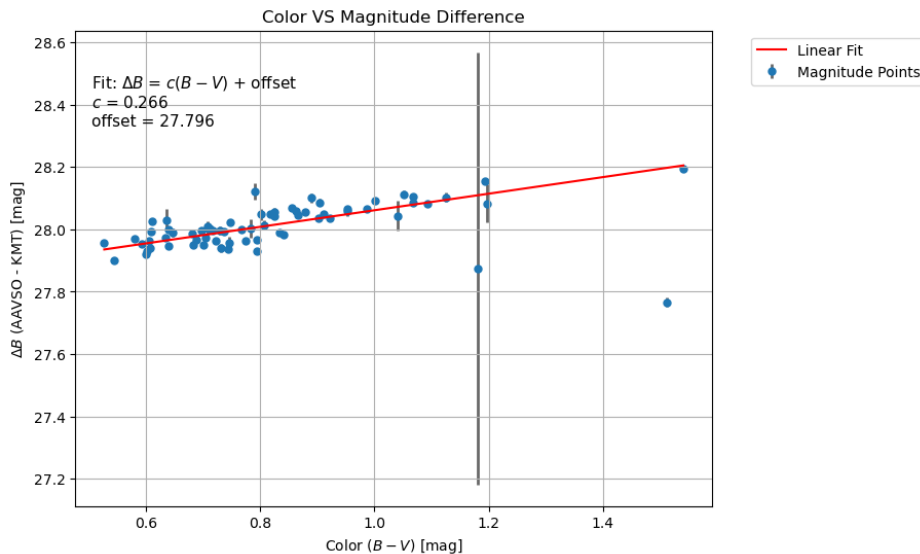


Figure 3.12: Plot of  $m_B - m_V$  (horizontal axis) versus  $m_B - m_{B,\text{inst}}$  (vertical axis) for a  $B$  band image taken on 2020 October 12 20:54. These points are for some reference stars within 15' of KSP-ZN7090. Note that the “offset” here is not the same as the “offset” term in Equation (3.15), because the vertical axis plots  $m_B - m_{B,\text{inst}}$  rather than  $m_B - m_{B'}$ . Nevertheless,  $c = 0.266$  is consistent with the  $c \approx 0.27$  value from Park et al. (2017).

### 3.7.4 Applying the Colour Correction

Finally, substituting Equation (3.19) into Equation (3.15) and rearranging, the corrected  $B$  band apparent magnitude value  $m_B$  can be obtained:

$$\begin{aligned}\Delta m_B &= m_B - m_{B'} = c(m_B - m_V) + \text{offset} \\ m_B - m_{B'} &= c(m_B - m_V) - c\langle m_{B,\text{ref}} - m_{V,\text{ref}} \rangle \\ m_B(1 - c) &= cm_V - c\langle m_{B,\text{ref}} - m_{V,\text{ref}} \rangle + m_{B'} \\ m_B &= \frac{cm_V - c\langle m_{B,\text{ref}} - m_{V,\text{ref}} \rangle + m_{B'}}{1 - c}\end{aligned}\quad (3.20)$$

where  $c = 0.27$  and  $\langle m_{B,\text{ref}} - m_{V,\text{ref}} \rangle = 0.783$  mag. Then the uncertainty in  $m_B$  is:

$$\begin{aligned}\delta m_B &= \sqrt{\left(\frac{\partial m_B}{\partial m_V}\right)^2 (\delta m_V)^2 + \left(\frac{\partial m_B}{\partial \langle m_{B,\text{ref}} - m_{V,\text{ref}} \rangle}\right)^2 (\delta \langle m_{B,\text{ref}} - m_{V,\text{ref}} \rangle)^2 + \left(\frac{\partial m_B}{\partial m_{B'}}\right)^2 (\delta m_{B'})^2} \\ &= \sqrt{\left(\frac{c}{1 - c}\right)^2 (\delta m_V)^2 + \left(\frac{c}{1 - c}\right)^2 (\delta \langle m_{B,\text{ref}} - m_{V,\text{ref}} \rangle)^2 + \left(\frac{1}{1 - c}\right)^2 (\delta m_{B'})^2} \\ &= \frac{1}{1 - c} \sqrt{(c\delta m_V)^2 + (c\delta \langle m_{B,\text{ref}} - m_{V,\text{ref}} \rangle)^2 + (\delta m_{B'})^2}\end{aligned}\quad (3.21)$$

where  $\delta \langle m_{B,\text{ref}} - m_{V,\text{ref}} \rangle = 0.058$  mag. The result of this colour correction on the  $B$  band light curve (from Figure 3.11a) is shown in Figure 3.13.

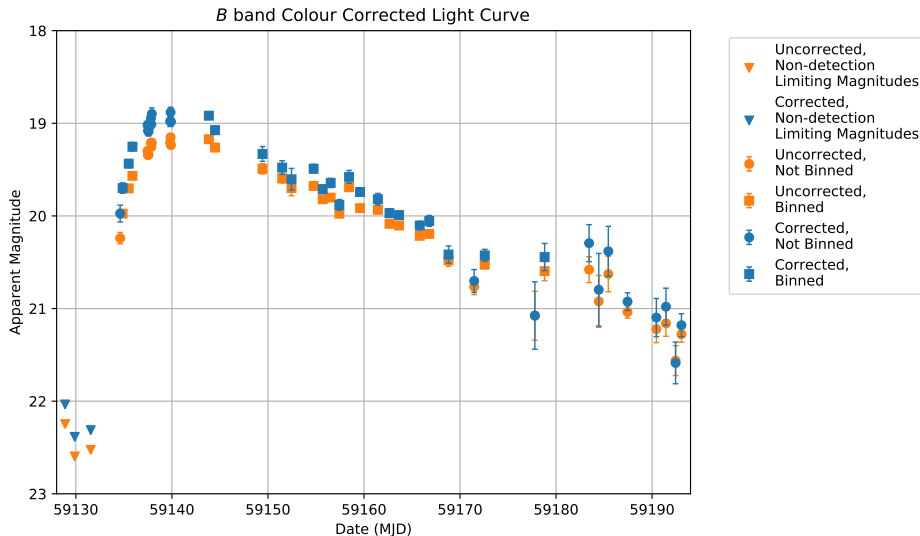


Figure 3.13: Colour correction applied to the  $B$  band light curve of KSP-ZN7090. The orange points are uncorrected, and the blue points are corrected according to Equations (3.20) and (3.21).

## 3.8 Interstellar Extinction Correction

### 3.8.1 About Interstellar Extinction

The final step for the light curve is to make a correction for interstellar extinction. When a certain object is being observed from Earth, interstellar material between the Earth and the object (e.g. dust) scatters and absorbs electromagnetic radiation coming from the object (Fitzpatrick 1999). This causes the object's measured apparent magnitude to be greater than what it actually is (i.e. the object appears dimmer). This scattering and absorption is called extinction. Interstellar extinction causes light from a source to appear redder, since shorter wavelengths are more strongly attenuated; this phenomenon is called reddening (Larson 2014).

Let us introduce some variables and terminology commonly used in the literature regarding interstellar extinction.  $A_x$  is called the extinction in band  $x$ , and has units of magnitudes.  $A_V$  is the total extinction in the  $V$  band and is sometimes just called the “absolute extinction” or “total extinction”.  $E(B - V) = A_B - A_V$  is called the reddening (Foley et al. 2014), and has units of magnitudes.  $R_V \equiv A_V/E(B - V)$ , which is dimensionless, has several names in the literature and is sometimes called the “reddening constant” (Schultz & Wiemer 1975), “interstellar reddening parameter” (Patriarchi et al. 2001), “ratio of the total-to-selective extinction” (Foley et al. 2014), or “extinction to reddening ratio” (Larson 2014). For the Milky Way,  $R_V \approx 3.1$  (Schultz & Wiemer 1975).

### 3.8.2 Correcting Interstellar Extinction

Now, let us determine the interstellar extinction  $A_x$  in band  $x$  for an object at coordinate (R.A., decl.). Firstly, the reddening  $E(B - V)$  corresponding to a particular (R.A., decl.) can be queried from a dust map such as in Schlegel et al. (1998), which is often called the “SFD dust map”. Let  $E(B - V)_{\text{SFD}}$  be the reddening from the SFD dust map. This can be obtained from the Caltech IPAC website<sup>1</sup>, or using the dustmaps Python package (Green 2018). The resulting reddening in the direction of KSP-ZN7090, at (R.A., decl.) = ( $21^{\text{h}}31^{\text{m}}3^{\text{s}}.05$ ,  $-53^{\circ}55'49''.91$ ) (J2000), is  $E(B - V)_{\text{SFD}} \simeq 0.02490$  mag.

There is an updated version of the SFD dust map model by Schlafly & Finkbeiner (2011) which is more accurate and is now more widely used. This is sometimes called the “S&F

---

<sup>1</sup>Caltech NASA/IPAC Galactic Dust Reddening and Extinction Tool: <https://irsa.ipac.caltech.edu/applications/DUST/>

dust map”. A correction could be made to the SFD model to obtain the updated reddening value  $E(B - V)_{\text{S&F}}$  corresponding to the S&F model:

$$E(B - V)_{\text{S&F}} = 0.86 \times E(B - V)_{\text{SFD}} \quad (3.22)$$

However, [Schlafly & Finkbeiner \(2011\)](#) provides a table to convert an  $E(B - V)_{\text{SFD}}$  value directly to an extinction value  $A_x$ , without first converting to  $E(B - V)_{\text{S&F}}$ . This is because the SFD model is still widely queried. Table 6 of [Schlafly & Finkbeiner \(2011\)](#) provides values of  $A_x/E(B - V)_{\text{SFD}}$  for a certain  $R_V$  and band  $x$ . Values from this table corresponding to the KMTNet filter system are shown in Table 3.3. Note that  $R_V = 3.1$  is being used, as for the Milky Way.

Band $x$	$A_x/E(B - V)_{\text{SFD}}$
CTIO $B$	3.641
CTIO $V$	2.682
SDSS $i$	1.698

Table 3.3: Values of  $A_x/E(B - V)_{\text{SFD}}$  from Table 6 of [Schlafly & Finkbeiner \(2011\)](#), with  $R_V = 3.1$

Using the values of  $A_x/E(B - V)_{\text{SFD}}$  in Table 3.3, the extinction  $A_x$  in band  $x$  for KSP-ZN7090 can be calculated by:

$$A_x = (A_x/E(B - V)_{\text{SFD}}) \times E(B - V)_{\text{SFD}} \quad (3.23)$$

where  $E(B - V)_{\text{SFD}} \simeq 0.02490$  mag in the direction of KSP-ZN7090. The resulting extinction values in the direction of KSP-ZN7090 are shown in Table 3.4.

Band $x$	Extinction $A_x$ [mag]
$B$	0.091
$V$	0.067
$I$	0.042

Table 3.4: Interstellar extinction in the direction of KSP-ZN7090, from the updated [Schlafly & Finkbeiner \(2011\)](#) dust map with  $R_V = 3.1$

After obtaining the  $A_x$  values, the effects of interstellar extinction can be corrected. Let  $m'_x$  be the apparent magnitude of KSP-ZN7090 in band  $x$ , uncorrected for extinction. Then

the actual apparent magnitude corrected for extinction is:

$$m_x = m'_x - A_x \quad (3.24)$$

Equation (3.24) was applied to all the data points in the light curves. The result is shown in Figure 3.14, which compares the *BVI* light curves of KSP-ZN7090 before and after this extinction correction procedure.

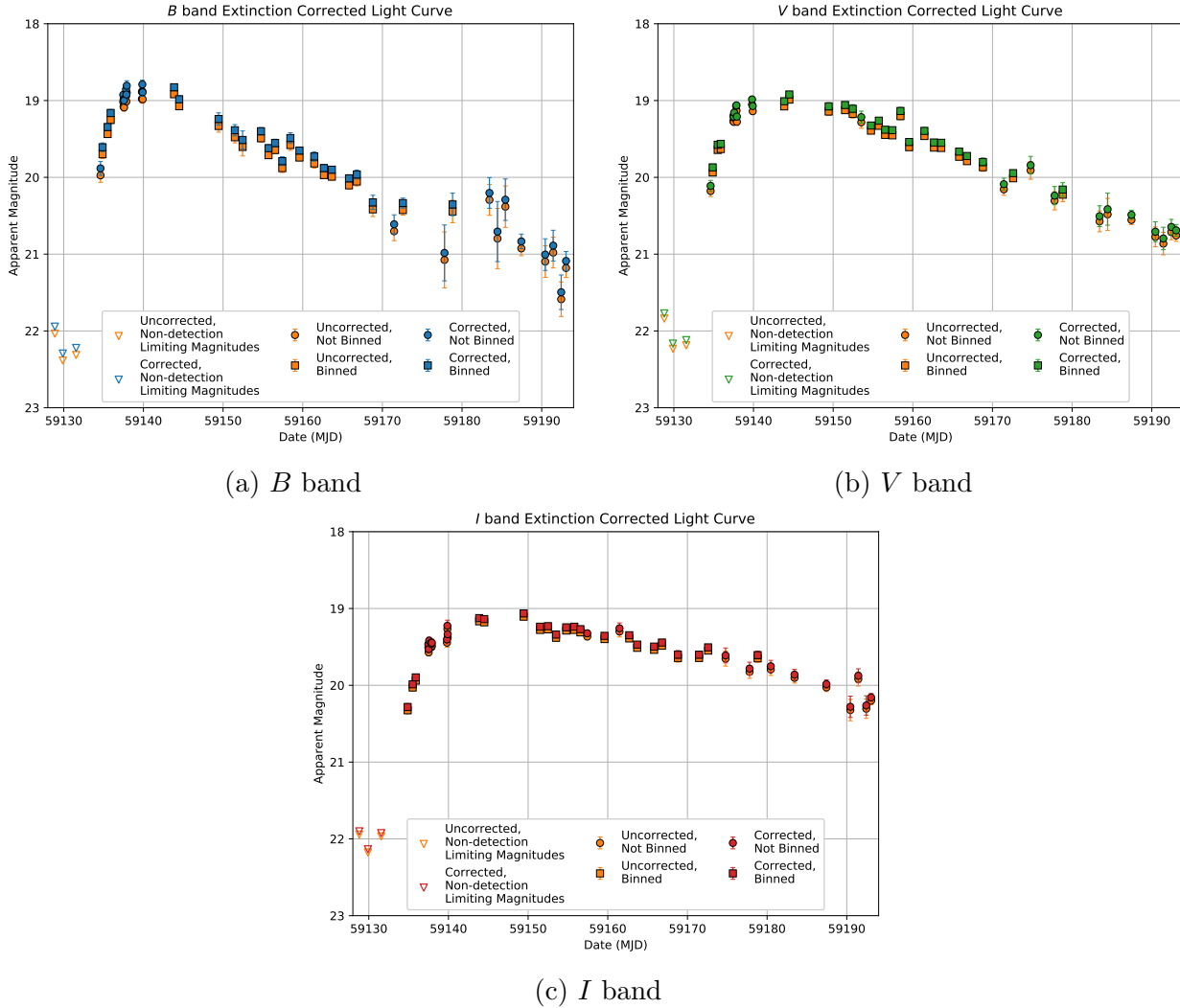


Figure 3.14: Extinction corrected light curves of KSP-ZN7090. The orange points are uncorrected, and the blue, green, and red points are extinction corrected for the *B*, *V*, and *I* bands respectively. Note that the orange points in the *B* band plot in Figure 3.14a were already colour corrected (i.e. these orange points are the blue points in Figure 3.13).

## 3.9 Key Results for Photometry and Light Curves

With the photometry process complete and the *BVI* light curves generated, let us present and summarize some of the key results. KSP-ZN7090 was first detected as a new point source in a *B* band image taken on 2020 October 12 at 14:44 UTC (MJD = 59134.61389) by KMTNet, shown in Figure 3.15b. This point source was located at (R.A., decl.) = ( $21^{\text{h}}31^{\text{m}}3\text{s}.05$ ,  $-53^{\circ}55'49''.91$ ) (J2000), and had a *B* band apparent magnitude of  $19.883 \pm 0.091$  mag. The source was subsequently detected in the *V* band 3 minutes later with an apparent magnitude of  $20.111 \pm 0.072$  mag. The first *I* band observation was several hours later on the same day at 20:00 UTC with an apparent magnitude of  $20.347 \pm 0.066$  mag. No data was available in the 3 days immediately before the first detection. The last image captured before the first detection was in the *I* band, on 2020 October 9 at 14:32 UTC, but the source was not detected at the  $3\sigma$  detection limit. The latest data points immediately before the first detection, on 2020 October 9, were all non-detections, with limiting magnitudes of  $\sim 22.404$ ,  $\sim 22.254$ , and  $\sim 22.009$  mag in the *B*, *V*, and *I* bands respectively. The *B* band last non-detection is shown in Figure 3.15a.

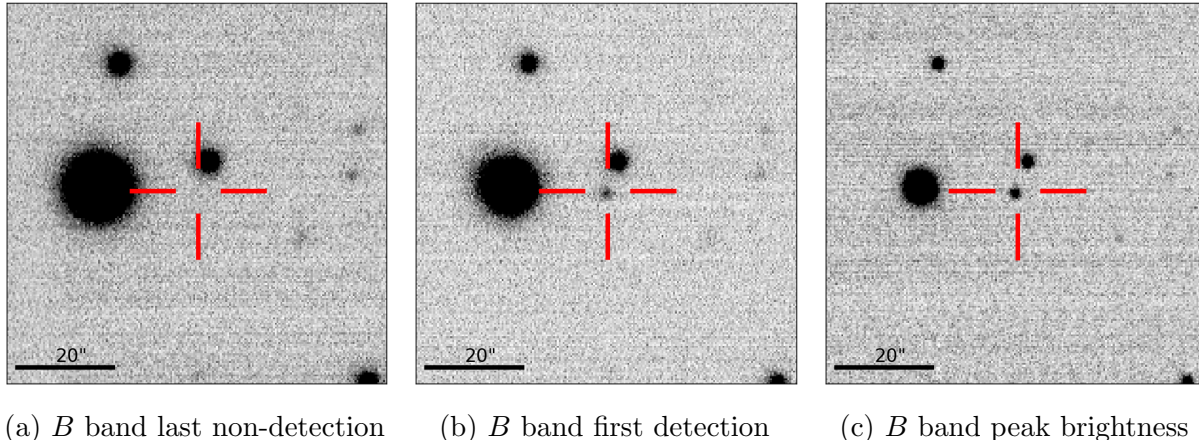


Figure 3.15: Important *B* band images of KSP-ZN7090 at key epochs

In addition, images were stacked up to 11 days before the first detection, reaching limiting magnitudes of  $\sim 22$  mag in the *BVI* bands, but no source was detected in these stacked images. This reinforces the first detection date as 2020 October 12. Further stacking of images before the first detection showed that KSP-ZN7090 has a faint host galaxy, which will be discussed in Chapter 4. The final *BVI* light curves of KSP-ZN7090 are shown in Figure 3.16.

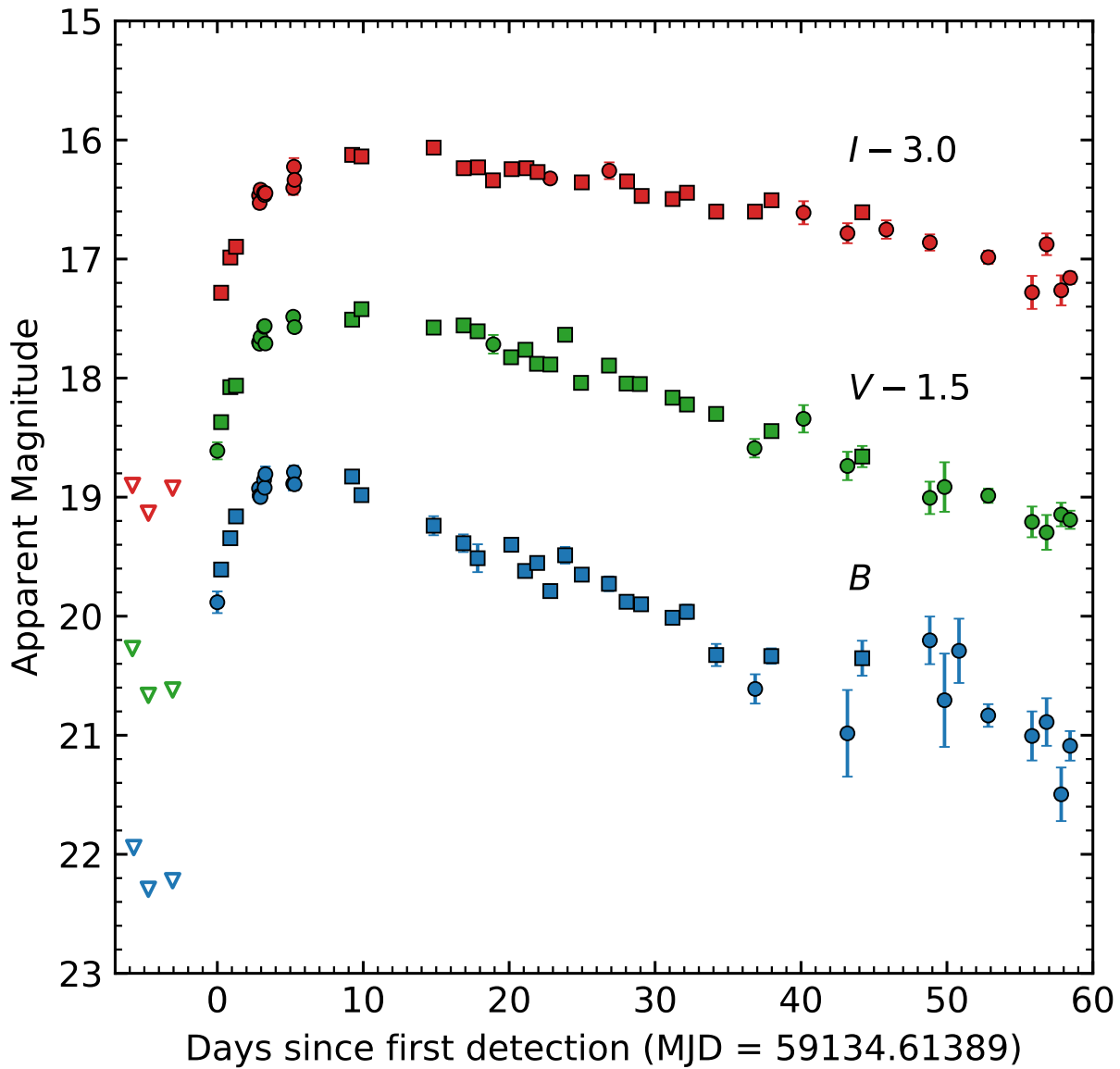


Figure 3.16: Colour and extinction corrected  $BVI$  light curves for KSP-ZN7090, vertically shifted for readability. The square points represent binned data, while the circular points represent data that was not binned. The inverted triangles are non-detection limiting magnitudes.

# Chapter 4

## Host Galaxy of KSP-ZN7090

### 4.1 Overview

In this chapter, KSP-ZN7090’s host galaxy will be analyzed. The host galaxy’s position and *BVI* apparent magnitudes will be determined. A complete analysis will be performed using a variety of different photometry methods. The final position of the host galaxy was determined to be (R.A., decl.) = ( $21^{\text{h}}31^{\text{m}}2\text{s}.86$ ,  $-53^{\circ}55'50\text{"}.75$ ) (J2000), shown in Figure 4.1b. The uncertainty of the R.A. and decl. coordinates were  $1.68''$  and  $1.00''$  respectively. For comparison, the position of KSP-ZN7090 is (R.A., decl.) = ( $21^{\text{h}}31^{\text{m}}3\text{s}.05$ ,  $-53^{\circ}55'49\text{"}.91$ ) (J2000). The positions of KSP-ZN7090 and its host galaxy differ by about  $2.95''$ . The final *B*, *V*, and *I* band apparent magnitudes of the host galaxy were measured to be  $22.165 \pm 0.276$ ,  $22.943 \pm 0.283$ , and  $21.773 \pm 0.112$  respectively. The *B* band magnitude was below the limiting magnitude of the stacked image used.

### 4.2 The Field around KSP-ZN7090 and its Host Galaxy

Figure 4.1 shows the field around KSP-ZN7090 and its host galaxy. This is an *I* band stacked image, made up of 31 *I* band images taken pre-burst. The position of KSP-ZN7090 is marked in red, and the final position of the host galaxy is marked in green. The galaxy appears as a black smudge slightly southwest of the SN. Note that the image has been heavily scaled to make the host galaxy more noticeable. In reality, the host galaxy has low SNR and is difficult to distinguish from the background, even for a stacked image like in Figure 4.1. Without stacking, the host galaxy is not discernible from the background.

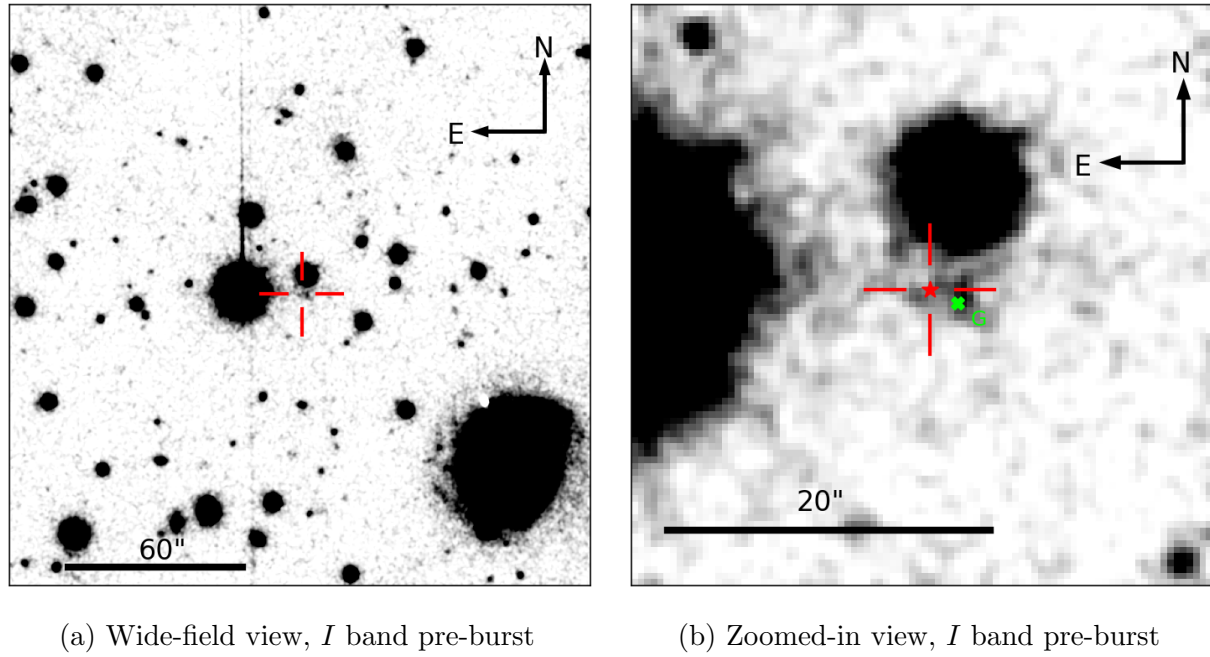
(a) Wide-field view,  $I$  band pre-burst(b) Zoomed-in view,  $I$  band pre-burst

Figure 4.1: The above figures show the field around KSP-ZN7090 and its host galaxy. These are stacked  $I$  band images taken pre-burst. Note that these images have been heavily scaled to make the host galaxy appear more noticeable. The location of KSP-ZN7090 is marked with a red star symbol and the red crosshairs. The final location of the host galaxy is marked with a green “X” and labelled “G”.

From Figure 4.1b, it is evident that the field is crowded due to a relatively bright foreground object north of the SN and host galaxy. This object has light which bleeds into the pixels belonging to the host galaxy, which is already faint. Thus, determining the position and magnitude of the host galaxy may be difficult, and will require photometry methods different from just simple aperture photometry or PSF photometry. Due to the crowded field, aperture photometry is not possible. Attempting to fit a Moffat PSF to the host galaxy alone is not a good idea, since there is light which spills over from the nearby bright object which will cause the fit will be skewed northwards.

In order to estimate the position of the host galaxy, stacked images like Figure 4.1 will be used. Two kinds of stacked images were created: pre-supernova (PRESN) images, which are stacked images consisting of all images up to  $\sim 2$  weeks before the SN first detection, and pre-burst (PREBT) images, which are stacked images consisting of all images up to  $\sim 1$  month before the SN first detection. The following sections will discuss about the different methods used to estimate the host galaxy position. The main goal is to get rid of the effects of the nearby bright object and the background, since the host galaxy is faint.

## 4.3 Fitting to Cropped Rectangular Region Only

### 4.3.1 Preliminary Fitting to Cropped Region

The first method which was attempted was to fit a Moffat function to a cropped rectangular region of an image, which contained as little of the nearby object as possible. Preliminary fits were performed in order to investigate the brightness of the host galaxy in relation to the nearby object and background. When this was done, the quality of these preliminary fits was very poor. The fitted Moffat function was unable to capture host galaxy well because of the background, which was comparable. This is shown in Figure 4.2, with the red rectangle being the cropped region. The fitted Moffat function in the bottom subfigure of Figure 4.2b is much brighter than the image (darker in the inverted image of Figure 4.2b). Hence the background is not represented well here.

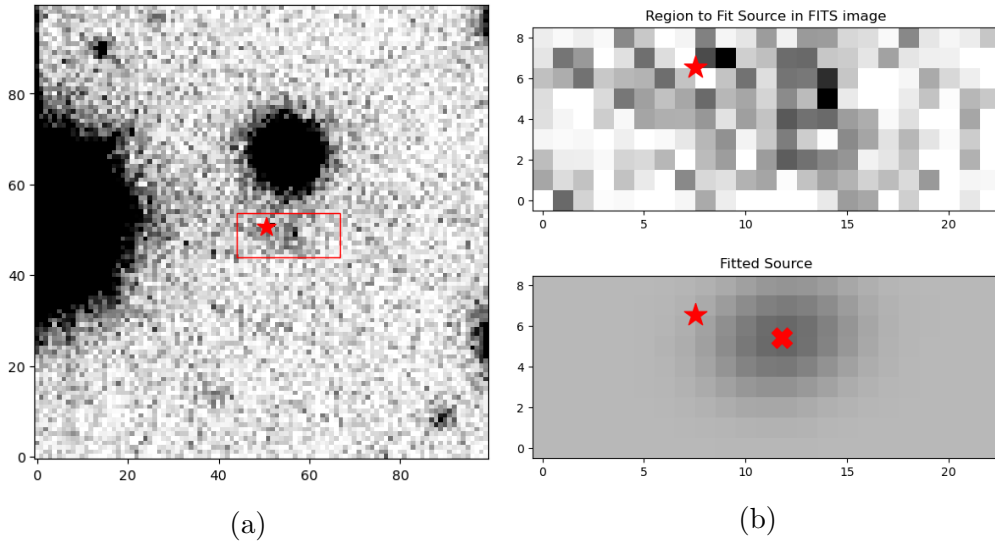


Figure 4.2: Preliminary fit to host galaxy with cropped rectangular region, for the  $I$  band PRESN image. The red star marker is the host galaxy and the “X” shows the position of the fitted host galaxy.

### 4.3.2 Background Circle Subtraction

In order to take into account the background, an alternate method was used, which was inspired from aperture photometry. Recall that in aperture photometry, an annulus is taken around the target object, and the pixel values inside this annulus are averaged in order to obtain an average background value. Taking an annulus here is not possible due to the nearby bright object. Instead, a circle was taken near the galaxy which is assumed to only contain background signal, and the pixel inside this circle were averaged in order to obtain

an average background value. This background value was then subtracted from the image, and a Moffat function was then fitted to the cropped rectangular region of the subtracted image. This is shown in Figure 4.3, with this background circle indicated by the green circle in Figure 4.3a. The resulting Moffat fit in Figure 4.3b was much better than that of Figure 4.2b, and represents the host galaxy and background relatively well.

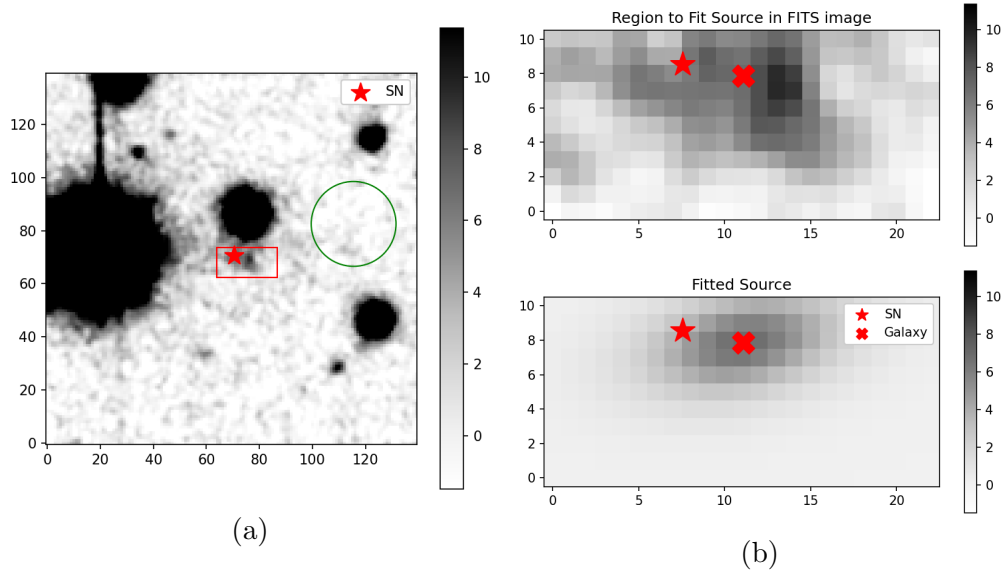


Figure 4.3: Fit to host galaxy with cropped rectangular region and a background circle subtracted, for the  $I$  band PRESN image. The red star marker is the host galaxy and the “X” shows the position of the fitted host galaxy. The background in the green circle was averaged and then subtracted from the image. A Moffat function was then fit to the subtracted image.

However, although this method performed better, there was a significant issue. If the green circle is modified slightly (e.g. translated or has a different radius value), then the fitted position of the host galaxy will be much different. Hence, this method is not reliable. The resulting host galaxy can be manipulated simply by changing the green circle for the background. This may be because the background enclosed by the green circle is not a good representation of the background nearer to the host galaxy. Furthermore, this method of simply selecting a cropped rectangle neglects the fact that light is being spilt over from the nearby bright object. It may be the case that the region around the host galaxy is dominated by light from the nearby object rather than the background, and hence subtracting the circle background would be useless. Thus, a different method is needed, which could account for both the background and the nearby bright object.

## 4.4 Fitting and Subtracting Out the Nearby Object with a Moffat Function

Let us assume here that this nearby object is a single star which can be modelled by a Moffat function. Since this nearby star dominates the region surrounding the host galaxy, a potential method to fit the host galaxy would be to first fit the nearby star, and then subtract it out. Then a fit on the host galaxy could be performed on a subtracted image ideally without the nearby star. This was attempted in Figure 4.4. Firstly, a rectangular region was selected which includes both the nearby star and the host galaxy, shown by the red box in Figure 4.4a. This rectangular region was then split into two subregions: one with only the nearby star (top region), and one with only the host galaxy (bottom region). A Moffat function was then fit to the top region to model the nearby star. After transforming between the coordinates of the two subregions, the fitted Moffat function for the nearby star was then subtracted from the bottom region. The subtracted image is the middle subfigure of Figure 4.4b. Finally, a Moffat function was fitted to the subtracted image, for the host galaxy. The result is shown in the rightmost subfigure of Figure 4.4b.

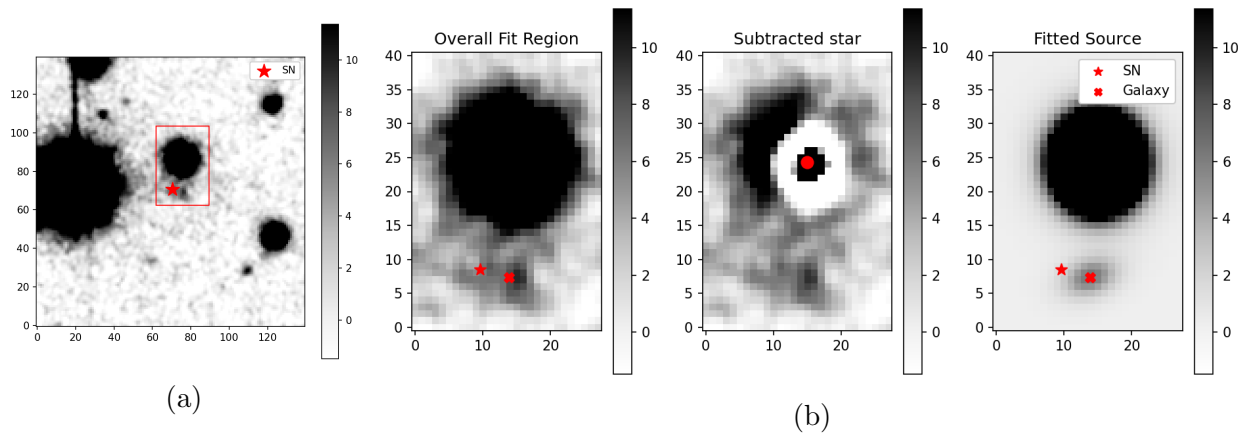


Figure 4.4: Fit to host galaxy with the nearby object (assumed to be a single star here modelled by a Moffat function) subtracted out, for the  $I$  band PRESN image

The rightmost subfigure of Figure 4.4b looks like a reasonable fit. However, upon closer inspection of the middle subfigure of Figure 4.4b, it appears that a Moffat function does not capture the nearby star well. The left portion of the star was left unsubtracted. Perhaps the host galaxy stretches behind the foreground nearby star. To account for this, another method should be used.

## 4.5 Fitting with a Combined PSF

Another method is to fit a combined PSF to a region containing both the host galaxy and the nearby object. Again, assuming that the nearby object is a single star, this nearby object can be modelled by a Moffat function. The host galaxy can be modelled by a Moffat or Gaussian function. Hence, a combined PSF, consisting of two Moffat functions summed together or a Moffat and a Gaussian function summed together, could be used.

### 4.5.1 Moffat and Moffat

The resulting fit for a combined function consisting of two Moffat functions is shown in Figure 4.5. While the fitted result in the bottom subfigure of Figure 4.5b appears to be good, this is actually not the case. The uncertainties in the fit parameters of the Moffat function ( $\beta$ ,  $\alpha_x$ , and  $\alpha_y$ ) for the host galaxy are  $\sim 1000\%$ . This indicates that a Moffat function may be a poor model for the host galaxy in this case.

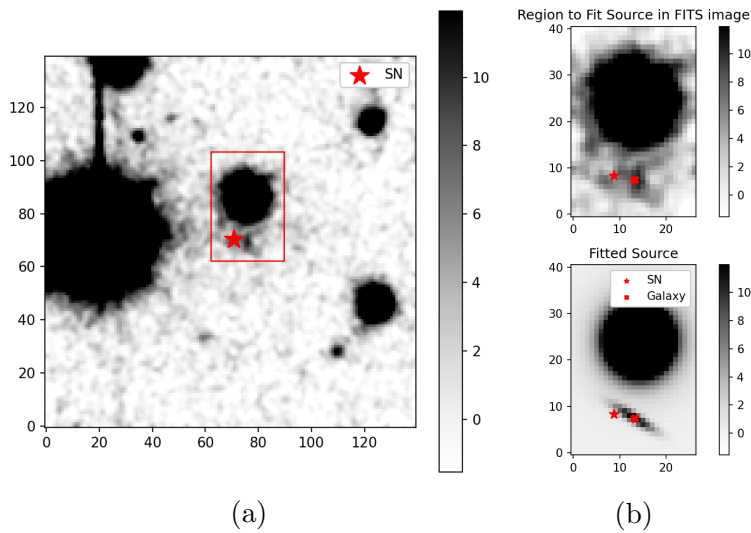


Figure 4.5: Fitting a combined function, consisting of two Moffat functions, to a region containing the host galaxy and nearby object (assumed to be a single star), for the  $I$  band PREBT image

### 4.5.2 Moffat and Gaussian

Perhaps a Gaussian model could be better for the host galaxy. Hence, a combined function consisting of a Moffat function (for the nearby star) and a Gaussian function (for the host galaxy) was fitted to a region containing both the host galaxy and the nearby object. This is shown in Figure 4.6. The fitted result in the bottom subfigure of Figure 4.6b appears

to be good. However, the calculated intensity of the host galaxy (by integrating the fitted Gaussian) has an uncertainty of  $\sim 35\%$ . The SNR is low. in addition, the fitted Moffat function for the nearby star is not centred on the nearby star. This, along with the poor subtraction in Figure 4.4b, suggests that a Moffat function is not a good representation of the nearby object. Hence, the nearby object might not be a single star.

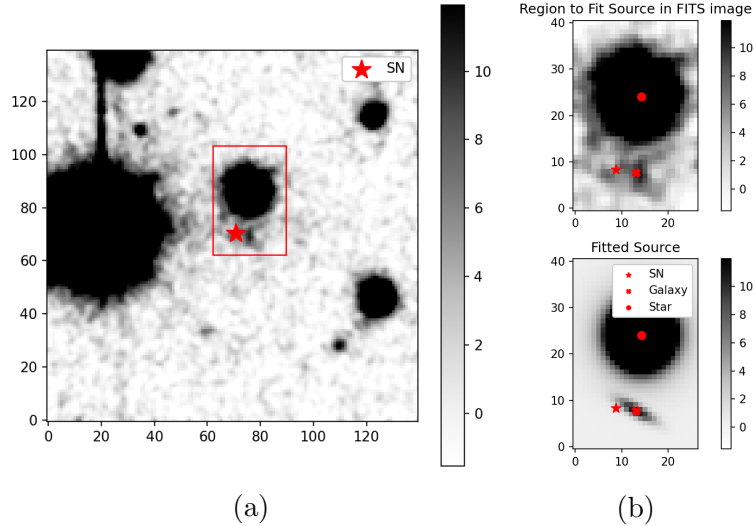


Figure 4.6: Fitting a combined function, consisting of a Moffat (for nearby object) and Gaussian (for host galaxy) function, to a region containing the host galaxy and nearby object (assumed to be a single star), for the  $I$  band PREBT image

## 4.6 Fitting with a Binary Star Model

The nearby object could be a binary star due to its slightly elongated shape, and because a single star model failed. Hence, a combined Gaussian model, consisting of two Gaussian functions, was fitted to a cropped region containing the nearby object only. This region is the green box in Figure 4.7. The fitted binary star was then subtracted from the image. The subtracted image is shown on the right subfigure of Figure 4.7. A smaller cropped region was then taken in the subtracted image, which contained the host galaxy only, shown in red in Figure 4.7. The centroid of this cropped region, calculated from a weighted mean, was then used for the position of the galaxy. The uncertainty value was from a weighted variance. Comparing the weighted variance with the average FWHM of the image (which is smaller), we can conclude that the host galaxy is an extended source.

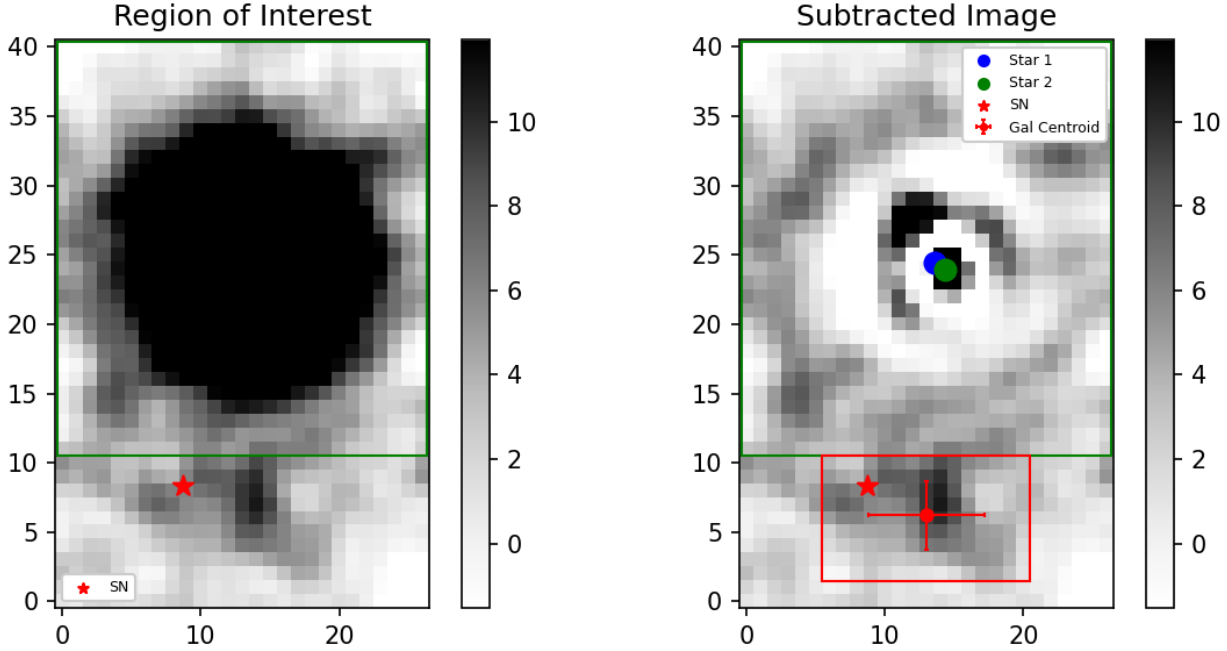


Figure 4.7: Fitting a binary star model to the nearby object, and then subtracting it from the image. This was for the  $I$  band PREBT image.

Suppose we have  $N$  values  $x_1, \dots, x_i, \dots, x_N$  with weights  $w_1, \dots, w_i, \dots, w_N$ . Then weighted mean  $x_{\text{avg}}$  and weighted variance  $\text{Var}(x_{\text{avg}})$  is given by Kirchner (2006) as:

$$x_{\text{avg}} = \frac{\sum_{i=1}^N w_i x_i}{\sum_{i=1}^N w_i} \quad (4.1)$$

$$\text{Var}(x_{\text{avg}}) = \frac{\sum_{i=1}^N w_i (x_i - x_{\text{avg}})^2}{\sum_{i=1}^N w_i} \times \frac{n_{\text{eff}}}{n_{\text{eff}} - 1} \quad (4.2)$$

where  $n_{\text{eff}}$  is the effective number of measurements, given as:

$$n_{\text{eff}} = \frac{\left(\sum_{i=1}^N w_i\right)^2}{\sum_{i=1}^N w_i^2} \quad (4.3)$$

These equations were used for the calculation of the centroid. The pixel values were used as the  $w_i$  values, and the pixel positions were used as the  $x_i$  values.

From the right subfigure of Figure 4.7, it is evident that a binary star model represents the nearby object better. The nearby object is subtracted out much better here. For completeness, a Gaussian and Moffat function were also fitted to the red region in Figure 4.7 for the host galaxy. However, the resulting fitted host galaxy position had much higher un-

certainty than the one obtained from the centroid method. Hence, the centroid method was used in the end. Moreover, notice that KSP-ZN7090 is at the nebulous edges of the galaxy, rather than at the centre bulge. This is consistent with what we should expect, because CCSNe should come from regions of a galaxy with vigorous star formation, not near the centre bulge of a galaxy.

## 4.7 Final Results

The process described in the previous section, with binary star fitting, was done for the PREBT images in the  $B$ ,  $V$ , and the  $I$  bands. Finally, aperture photometry was performed on subtracted image in order to estimate the host galaxy's apparent magnitude. The position of the host galaxy was selected to be that of from the centroid calculation for the  $I$  band PREBT image. This is because the  $I$  band PREBT image is relatively better in quality compared to those of other bands. The host galaxy's final position is (R.A., decl.) = ( $21^{\text{h}}31^{\text{m}}28.86$ ,  $-53^{\circ}55'50.75''$ ) (J2000), with an uncertainty of  $1.68''$  and  $1.00''$  in the R.A. and decl. respectively. The final corrected magnitudes (colour and extinction corrected) are shown in Table 4.1.

Band	Apparent Magnitude	Limiting Magnitude
$B$	$22.165 \pm 0.276$	21.846
$V$	$22.943 \pm 0.283$	22.771
$I$	$21.773 \pm 0.112$	22.569

Table 4.1: Estimated apparent magnitudes of KSP-ZN7090's host galaxy

# Chapter 5

## Preliminary Light Curve Analysis

### 5.1 Overview

In this chapter, some preliminary and exploratory analyses will be conducted on the *BVI* light curves of KSP-ZN7090. Fits will be made to KSP-ZN7090’s early light curve order to determine KSP-ZN7090’s temporal parameters. In Section 5.2, a polynomial fit will be performed to the entire light curve in order to estimate KSP-ZN7090’s peak epoch. This value will be then be used to normalize the light curves, and will help determine which part of the light curve is considered “early”. Then in Section 5.3, a power law model will be fitted to the early part of the normalized light curves, and KSP-ZN7090’s epoch of first light will be estimated from this. In Section 5.4, a type classification will be assigned to KSP-ZN7090 based on its *V* band light curve.

### 5.2 Peak Epoch

To estimate the peak epoch of KSP-ZN7090, a seventh degree polynomial was fitted to the light curves of each band after the first detection on 2020 October 12 at 14:44 UTC (MJD = 59134.61389). Polynomial fits have been used before in the literature to estimate the peak epoch of a SN, such as in [Shappee et al. \(2018\)](#). A seventh degree polynomial was used in this work because of its end behaviour, and because it was able to capture the light curves well. An investigation was also conducted with polynomials of other degrees (both greater than and less than 7), but a seventh degree yielded the best results. From this seventh degree polynomial fit, the peak in the *B*, *V*, and *I* bands is estimated to have occurred at  $5.610 \pm 0.187$ ,  $7.792 \pm 0.248$ , and  $10.956 \pm 0.347$  days respectively after the first

detection. The light curves used for this fitting were converted to flux units.

Monte Carlo simulations were used to fit the light curves, in which each data point was randomly shifted within its uncertainty range. To be precise, each data point was modelled as a Gaussian distribution centred about its flux value with standard deviation equal to its flux uncertainty. Each Monte Carlo trial consisted of randomly drawing a value from each Gaussian distribution, and then applying a polynomial fit to these drawn values using nonlinear least squares. The best fit parameters were the averaged fit parameters from all Monte Carlo trials. The peak value was found by analytically computing the roots of the derivative of the fitted polynomial, and then finding the global maximum within the fit region. This is shown in Figure 5.1.

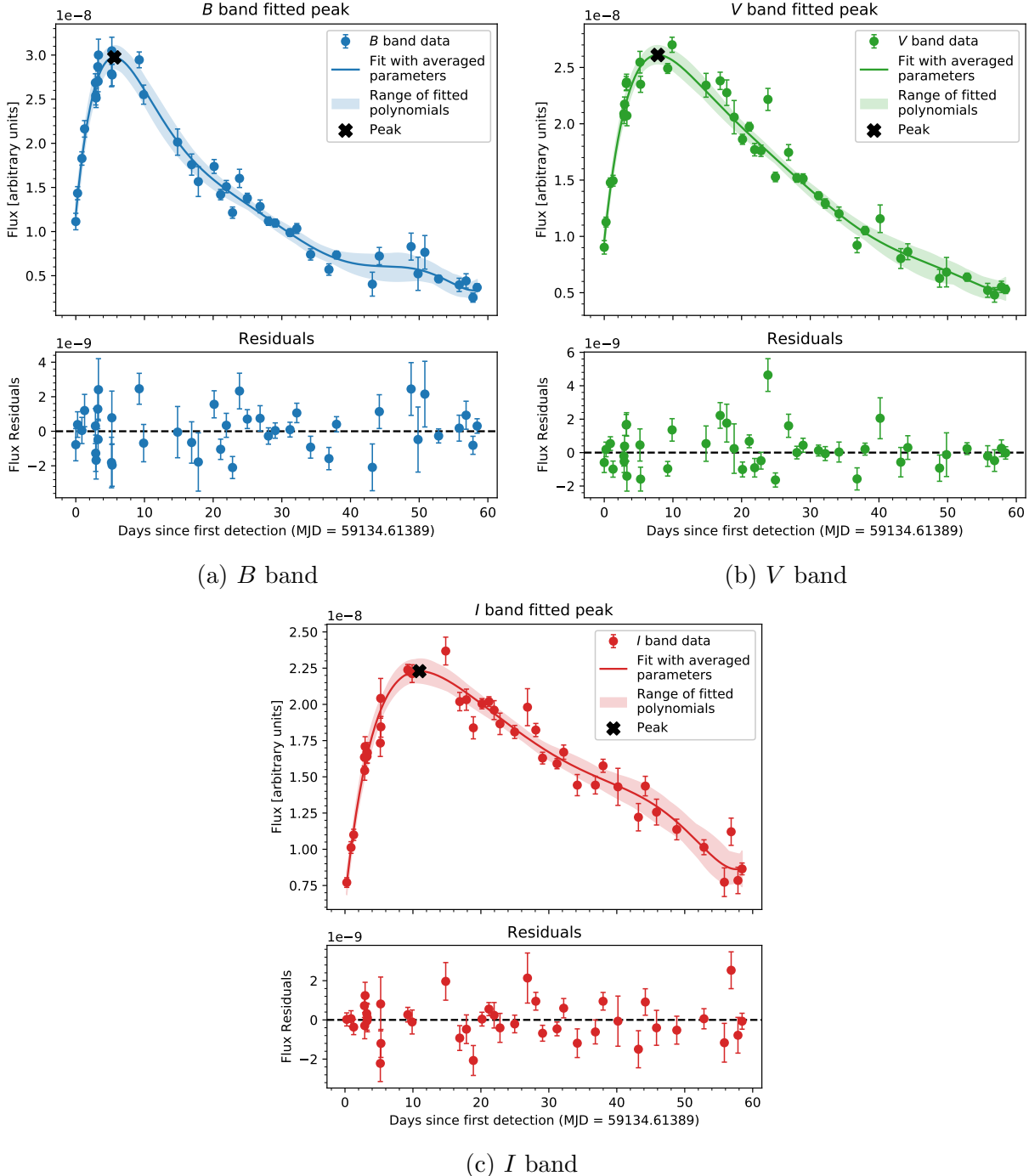


Figure 5.1: Fitted peaks of KSP-ZN7090's  $B$ ,  $V$ , and  $I$  band light curves. The shaded areas represent the range of the fitted polynomials from the Monte Carlo trials, and the fitted peak is marked with a black “X”. The reduced chi-squared ( $\chi^2/\text{dof}$ ) for the fits are 0.803, 1.242, and 0.861 for the  $B$ ,  $V$ , and  $I$  band respectively.

## 5.3 Early Power Law Fitting

### 5.3.1 Single Power Law and Epoch of First Light

In order to determine the epoch of first light, a single power law was fitted to the early light curve, given by Equation (5.1).  $f_\lambda(t)$  is the flux in the band  $\lambda$  at  $t$  days after the first detection,  $t_0$  is the epoch of first light, and  $n$  is the power index.

$$f_\lambda(t) = \begin{cases} 0 & \text{if } t < t_0 \\ C_\lambda(t - t_0)^n & \text{if } t \geq t_0 \end{cases} \quad (5.1)$$

Equation (5.1) was fit only to the early part of KSP-ZN7090's light curve, which was selected to be the first 2 days after the first detection. This roughly follows the method of [Gonzalez-Gaitan et al. \(2015\)](#), in which early data up to half of the maximum flux was used. However, in the case of KSP-ZN7090's light curve, fitting to only up to half of the maximum flux would not produce meaningful results, because there are only 2 data points each in the  $B$  and  $V$  bands that are less than half of the maximum flux. Hence, a fit was done to the first 2 days after the first detection.

Equation (5.1) was simultaneously fit to the flux-normalized light curves of all 3 bands, so that  $t_0$  and  $n$  were constrained to be the same for all 3 bands. The flux values were normalized against the peak flux at the peak epochs of each band, found in Section 5.2. The results are shown in Figure 5.2. The epoch of first light was  $t_0 = -0.191 \pm 0.126$  days, and the power index was  $n = 0.285 \pm 0.068$ . This  $t_0$  value suggests that KSP-ZN7090 was detected less than one day after its explosion, making it a young SN discovered in its infant phase. A double power law (Equation 2.4) was also attempted, but the results are nearly identical in this fit region (first 2 days after the first detection), in that the second power law plays no role.

The fitted value of the power law index can also inform us about the physical mechanisms contributing to the light curve's rise. [Gonzalez-Gaitan et al. \(2015\)](#) mentions that power law indices less than  $n = 1.5$  suggest that the light curve rise is powered by shock cooling emission, based on a discussion by [Piro & Nakar \(2013\)](#). They examined the rise times of 223 Type II SNe from SDSS and SNLS, finding that most of them followed  $n \lesssim 1.4$ , implying that most Type II SNe are powered by shock cooling emission. For KSP-ZN7090, we have  $n = 0.285 \pm 0.068 < 1.5$ , which suggests that the rise of KSP-ZN7090's light curve could perhaps be powered by shock cooling emission.

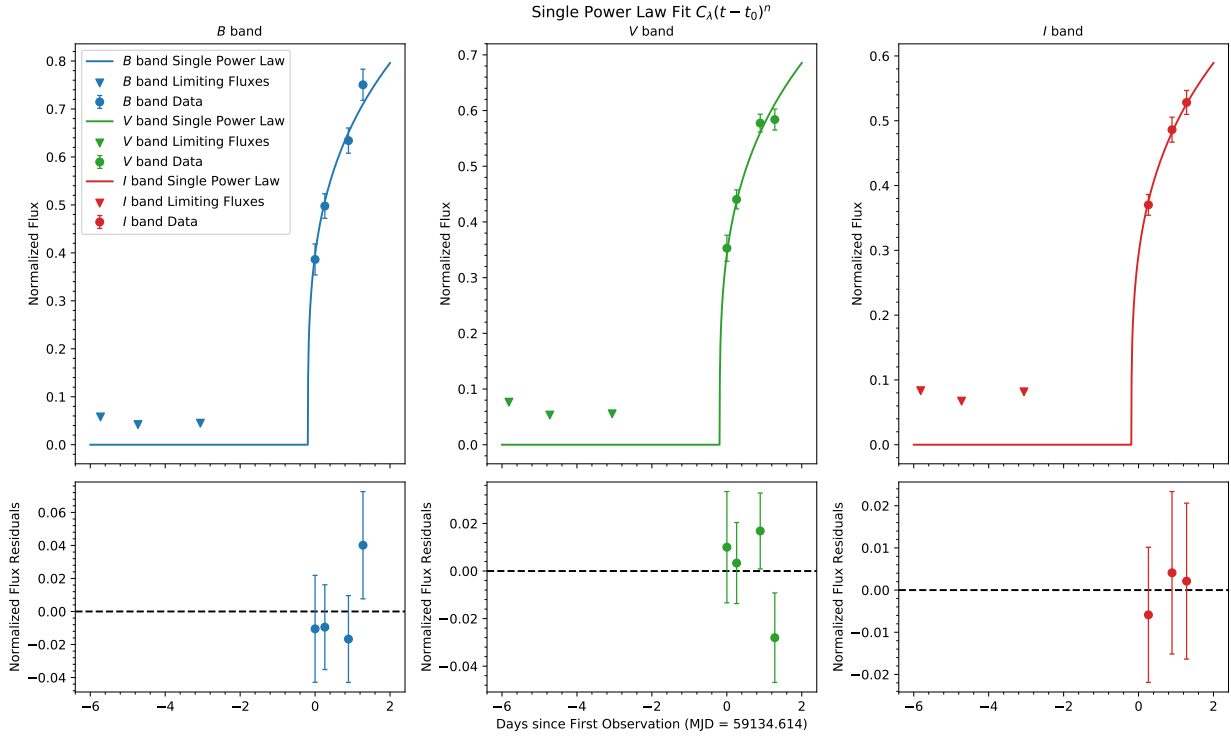


Figure 5.2: Single power law fits to KSP-ZN7090’s early light curve.  $\chi^2/\text{dof} = 0.986$ .

### 5.3.2 Rise Time

With the peak epoch and the epoch of first light, we can now compute a rough estimate of KSP-ZN7090’s rise times in each band. The rise time of a SN light curve is the time from the explosion epoch to peak epoch (Gonzalez-Gaitan et al. 2015). This is a good metric to compare with other SNe, and can potentially inform us about the physical mechanisms behind the SN’s rise. By subtracting  $t_0$  (which is negative) from the peak epochs in Section 5.2, we obtain rise times of  $5.801 \pm 0.225$ ,  $7.983 \pm 0.278$ , and  $11.147 \pm 0.369$  days for the  $B$ ,  $V$ , and  $I$  bands respectively. Comparisons of rise times of SNe powered by different mechanisms will be discussed in Sections 8.5 and 9.4.

## 5.4 KSP-ZN7090 Type Classification

Let us now assign a type classification for KSP-ZN7090. In order to confirm a SN’s type, its spectrum is required. Spectra have been obtained for KSP-ZN7090, but have not been extensively analyzed yet at the time of this work, since the focus of this thesis is light curve analysis. However, a rough inspection of KSP-ZN7090’s spectra revealed a H $\alpha$  absorption feature. A SN’s spectrum is used to distinguish it between the Type I class, which does

not have hydrogen lines, and the Type II class, which has hydrogen lines (Carroll & Ostlie 2017). Hence, KSP-ZN7090 can be classified as a Type II SN based on this rough inspection.

Now, let us determine the subclass of Type II SNe that KSP-ZN7090 belongs to. KSP-ZN7090 can be classified photometrically based on its light curve, following the definition in Faran et al. (2014) which was mentioned in Section 2.3.2. Faran et al. (2014) presents a definition which is used to distinguish between Type II-P and Type II-L SNe, which is used by many others in the literature. Their definition is that if a Type II SN has a  $V$  band light curve which declines by more than 0.5 mag from its peak brightness during the first 50 days after its explosion, then the SN can be photometrically classified as a Type II-L SN. Figure 5.3 shows the  $V$  band light curve of KSP-ZN7090. From polynomial fitting in Section 5.2, the peak  $V$  band magnitude was estimated to be  $18.958 \pm 0.011$  mag. At 50 days after first detection, we see that the  $V$  band light curve declines to around  $\sim 20.5$  mag. Hence, in the first 50 days after first detection, KSP-ZN7090's  $V$  band light curve declines by  $\sim 1.5$  mag from its peak value. Since the first detection is after the explosion epoch here, therefore KSP-ZN7090 satisfies the definition in Faran et al. (2014) for Type II-L SNe. Hence, we can classify KSP-ZN7090 as a Type II-L SN, photometrically based on its light curve.

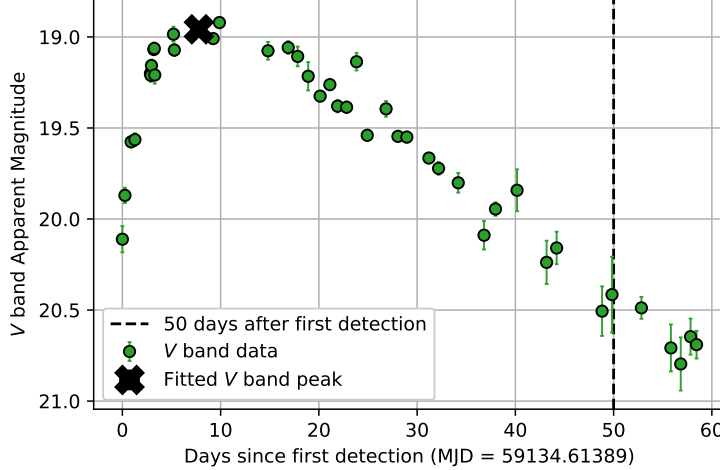


Figure 5.3:  $V$  band apparent magnitude light curve of KSP-ZN7090

# Part III

## Bolometric Light Curve

# Chapter 6

## Bolometric Light Curve from Blackbody Fitting

### 6.1 Overview

In this chapter, the method of blackbody fitting for constructing bolometric light curves will be discussed. The first few sections will go over the theory and how this method is done. In Section 6.6, this method will be verified with the Sun's parameters. In Section 6.8, this method will be applied to KSP-ZN7090. Key equations in this chapter are boxed.

### 6.2 Magnitude Definitions

#### 6.2.1 Magnitudes and Fluxes

Consider two stars with apparent magnitudes  $m_1$  and  $m_2$ , and fluxes  $F_1$  and  $F_2$  in a certain band. Flux, also known as irradiance, has SI units of  $\text{W/m}^2$  and is a measure of a star's brightness as viewed from Earth. As defined by Norman Pogson, a star which is 100 times brighter than another fainter star will have an apparent magnitude of 5 less than that of the fainter star (Pogson 1856). Hence:

$$\frac{F_2}{F_1} \equiv 100^{(m_1 - m_2)/5} \quad (6.1)$$

This implies:

$$m_1 - m_2 = -2.5 \log_{10} \left( \frac{F_1}{F_2} \right) \quad (6.2)$$

By convention, apparent magnitude values are defined based on some zero point magnitude value ZP. Suppose a certain star has flux  $F_x$  in band  $x$ . Then we say that the star's apparent magnitude  $m_x$  in band  $x$  is:

$$\begin{aligned} m_x &\equiv -2.5 \log_{10} (F_x) + \text{ZP}_x \\ &= -2.5 \log_{10} (F_x) - [-2.5 \log_{10} (F_{x,0})] \\ &= -2.5 \log_{10} \left( \frac{F_x}{F_{x,0}} \right) \end{aligned} \quad (6.3)$$

where  $\text{ZP}_x \equiv 2.5 \log_{10} (F_{x,0})$  is the zero point magnitude in band  $x$ .  $F_{x,0}$  is called the zero point flux in band  $x$ . By definition, a star with flux  $F_{x,0}$  in band  $x$  will have an apparent magnitude of 0 in band  $x$ . Different filter systems use different values of  $F_{x,0}$ .

### 6.2.2 Spectral Flux Density

In practice, filter systems do not provide a zero point flux value. Instead, they provide a zero point spectral flux density value, which is either given as per unit wavelength or per unit frequency. Spectral flux density per unit wavelength ( $f_\lambda$ ) has SI units of  $\text{W}/(\text{m}^2 \cdot \text{m})$ , while spectral flux density per unit frequency ( $f_\nu$ ) has SI units of  $\text{W}/(\text{m}^2 \cdot \text{Hz})$ . However,  $f_\nu$  is often reported in units of Janskys (Jy) rather than in SI units ( $1 \text{ Jy} = 10^{-26} \text{ W}/(\text{m}^2 \cdot \text{Hz})$ ).

We can relate  $f_\nu$  and  $f_\lambda$  using the relationship  $f_\lambda d\lambda = f_\nu d\nu$ :

$$\begin{aligned} f_\lambda d\lambda &= f_\nu d\nu \\ f_\lambda &= \left| \frac{d\nu}{d\lambda} \right| f_\nu \\ &= \left| \frac{d}{d\lambda} \left( \frac{c}{\lambda} \right) \right| f_\nu \\ &= \frac{c}{\lambda^2} f_\nu \end{aligned} \quad (6.4)$$

A zero point spectral flux density per unit frequency value  $f_{\nu,0}$  is usually provided by filter systems. We can rewrite Equation (6.3) and say that the monochromatic apparent magnitude of a star at frequency  $\nu$  is:

$$m_\nu = -2.5 \log_{10} \left( \frac{f_\nu}{f_{\nu,0}} \right) \quad (6.5)$$

Similarly, the monochromatic apparent magnitude of a star at wavelength  $\lambda$  is:

$$m_\lambda = -2.5 \log_{10} \left( \frac{f_\lambda}{f_{\lambda,0}} \right) \quad (6.6)$$

where  $f_{\lambda,0}$  is the zero point spectral flux density per unit wavelength for wavelength  $\lambda$ .

Values for  $f_{\nu,0}$  are shown in Table 6.1. Values for the Vega magnitude system, which use Johnson-Cousins filters, were obtained from Table A2 of [Bessell et al. \(1998\)](#). The effective wavelength values for the Johnson-Cousins filters (updated) were obtained from Table 1 of [Bessell \(2005\)](#).  $f_{\nu,0}$  values for the AB magnitude system, which use Sloan filters, were obtained from Table 2a of [Fukugita et al. \(1996\)](#). Note that the Sloan filters were designed so that  $f_{\nu,0} = 3631$  Jy in every band. Sometimes,  $f_{\lambda,0}$  values are also given, as in Table 6.2.

Magnitude & Filter System	Band $x$	Effective Wavelength $\lambda_{\text{eff},x}$ [ $\mu\text{m}$ ]	$f_{\nu_{\text{eff},x},0}$ [Jy]
Vega, Johnson- Cousins	$U$	0.3663	1790
	$B$	0.4361	4063
	$V$	0.5448	3636
	$R$	0.6407	3064
	$I$	0.7980	2416
AB, Sloan	$u$	0.3557	3631
	$g$	0.4825	3631
	$r$	0.6261	3631
	$i$	0.7672	3631
	$z$	0.9097	3631

Table 6.1: Zero point spectral flux densities for the Vega and AB magnitude systems, obtained from [Bessell et al. \(1998\)](#), [Bessell \(2005\)](#), and [Fukugita et al. \(1996\)](#).  $f_{\nu_{\text{eff},x},0}$  is the zero point spectral flux density per unit frequency for band  $x$ 's effective frequency  $\nu_{\text{eff},x} = c/\lambda_{\text{eff},x}$ .

Band $x$	$\lambda_{\text{eff},x}$ [ $\mu\text{m}$ ]	$f_{\lambda_{\text{eff},x},0}$ [ $\times 10^{-11} \cdot \text{erg} \cdot \text{cm}^{-2} \cdot \text{s}^{-1} \cdot \text{\AA}^{-1}$ ]
$U$	0.366	417.5
$B$	0.438	632
$V$	0.545	363.1
$R$	0.641	217.7
$I$	0.798	112.6

Table 6.2: Zero point spectral flux densities per unit wavelength for the Vega system, from [Bessell et al. \(1998\)](#)

### 6.3 Converting Magnitude to Spectral Flux Density

Let the apparent magnitude in a certain band  $x$  be  $m_x$ .  $m_x$  is equal to the monochromatic apparent magnitude at band  $x$ 's effective wavelength  $\lambda_{\text{eff},x}$ , which is  $m_{\lambda_{\text{eff},x}}$ . Hence, from

Equation (6.6), we can say that:

$$m_x = m_{\lambda_{\text{eff},x}} = -2.5 \log_{10} \left( \frac{f_{\lambda_{\text{eff},x}}}{f_{\lambda_{\text{eff},x},0}} \right)$$

Now, we are given  $m_x$ , and we have  $f_{\nu_{\text{eff},x},0}$  from Table 6.1. We want to find  $f_{\lambda_{\text{eff},x}}$ . Substituting Equation (6.4) into the above equation and rearranging, we can obtain  $f_{\lambda_{\text{eff},x}}$  in terms of  $m_x$ ,  $f_{\nu_{\text{eff},x},0}$ , and  $\lambda_{\text{eff},x}$ :

$$\begin{aligned} m_x &= -2.5 \log_{10} \left( \frac{f_{\lambda_{\text{eff},x}}}{f_{\lambda_{\text{eff},x},0}} \right) \\ m_x &= -2.5 \log_{10} \left( \frac{f_{\lambda_{\text{eff},x}}}{(c/\lambda_{\text{eff},x}^2) f_{\nu_{\text{eff},x},0}} \right) && \text{by Equation (6.4)} \\ 10^{-m_x/2.5} &= \frac{f_{\lambda_{\text{eff},x}}}{(c/\lambda_{\text{eff},x}^2) f_{\nu_{\text{eff},x},0}} \\ 10^{-m_x/2.5} (c/\lambda_{\text{eff},x}^2) f_{\nu_{\text{eff},x},0} &= f_{\lambda_{\text{eff},x}} \end{aligned}$$

$$f_{\lambda_{\text{eff},x}} = (c/\lambda_{\text{eff},x}^2) (f_{\nu_{\text{eff},x},0}) (10^{-m_x/2.5}) \quad (6.7)$$

For example, in order to find the spectral flux density per unit wavelength in the Johnson *B* band ( $f_{\lambda_{\text{eff},B}}$ ) given  $m_B$ , we can use Equation (6.7) with the values  $f_{\nu_{\text{eff},B},0} = 4063$  Jy and  $\lambda_{\text{eff},B} = 0.438$  μm, as from Table 6.1. If  $f_{\lambda_{\text{eff},x}}$  is already known, as in Table 6.2, then the following equation could be used instead:

$$f_{\lambda_{\text{eff},x}} = (f_{\lambda_{\text{eff},x},0}) (10^{-m_x/2.5}) \quad (6.8)$$

## 6.4 Blackbody

### 6.4.1 Planck's Function

Now, let us model our star as a blackbody. Planck's function represents blackbody spectra, and is given by Carroll & Ostlie (2017) as:

$$B_\lambda(T) = \frac{2hc^2/\lambda^5}{\exp [hc/(\lambda k_B T)] - 1} \quad (6.9)$$

where  $h$  is Planck's constant and  $k_B$  is Boltzmann's constant. Based on this definition,  $B_\lambda(T)$  is the spectral flux density per unit wavelength per steradian at temperature  $T$ .  $B_\lambda(T)$  has SI units of  $\text{W}/(\text{m}^2 \cdot \text{m} \cdot \text{sr}^{-1})$ . The wavelength corresponding to the peak of Equation (6.9)

can be found by Wien's Displacement Law:

$$\lambda_{\text{peak}} = \frac{b}{T} \quad (6.10)$$

where  $b = \lambda_{\text{peak}} T = 2.897771955 \times 10^{-3}$  m · K is a constant (Tiesinga et al. 2021).

### 6.4.2 Spectral Flux Density and Planck's Function

Assuming the star is a blackbody, let us find amount of energy radiating from the star per unit time per unit wavelength. Let us call this quantity the spectral power per unit wavelength, denoting it with the symbol  $p_\lambda$ . This has SI units of W/m. Let us assume the star is spherical in shape with radius  $R$ , and hence has a surface area of  $4\pi R^2$ . Assuming the star emits blackbody radiation isotropically, we can integrate  $B_\lambda(T)$  in spherical coordinates to obtain  $p_\lambda$ :

$$\begin{aligned} p_\lambda &= 4\pi R^2 \int_0^{2\pi} \int_0^{\pi/2} B_\lambda(T) \cos \theta \sin \theta d\theta d\phi \\ &= (4\pi R^2)(2\pi) \int_0^{\pi/2} B_\lambda(T) \cos \theta \sin \theta d\theta \\ &= (8\pi^2 R^2)(0.5)B_\lambda(T) \\ &= 4\pi^2 R^2 B_\lambda(T) \end{aligned} \quad (6.11)$$

Now, note that  $p_\lambda$  is analogous to luminosity as  $f_\lambda$  is analogous to flux. Hence, we can relate  $p_\lambda$  and  $f_\lambda$  by:

$$f_\lambda = \frac{p_\lambda}{4\pi r^2} \quad (6.12)$$

where  $r$  is the distance between Earth and the star. Combining Equations (6.11) and (6.12), we obtain the relationship between spectral flux density per unit wavelength  $f_\lambda$  and Planck's function  $B_\lambda(T)$ :

$$f_\lambda = \frac{\pi R^2}{r^2} B_\lambda(T) = \left( \frac{\pi R^2}{r^2} \right) \frac{2hc^2/\lambda^5}{\exp [hc/(\lambda k_B T)] - 1} \quad (6.13)$$

### 6.4.3 Blackbody Fit

Equation (6.13) gives the blackbody spectrum of the object. Knowledge of this will allow us to find the temperature  $T$  of the object, which can be used to find the bolometric flux of the object. In practice,  $R$  and  $r$  may be unknown. But if this is the case, we can still find  $T$  given the object's apparent magnitudes in at least two bands. Suppose we have apparent magnitudes of the object in band  $x$  and band  $y$ , called  $m_x$  and  $m_y$  respectively.

Using Equation (6.7) and Table 6.1, we can convert these apparent magnitude values to spectral flux densities per unit wavelength. We now have two data points,  $(\lambda_{\text{eff},x}, f_{\lambda_{\text{eff},x}})$  and  $(\lambda_{\text{eff},y}, f_{\lambda_{\text{eff},y}})$ , which could be used to fit this function:

$$f_\lambda = AB_\lambda(T) = \frac{2Ahc^2/\lambda^5}{\exp [hc/(\lambda k_B T)] - 1} \quad (6.14)$$

where  $A$  and  $T$  are fit parameters. Equation (6.14) is the same as Equation (6.13) except that we replace  $\pi R^2/r^2$  with a proportionality constant  $A$ .

## 6.5 Bolometric Flux and Bolometric Luminosity

Following the procedure in Section 6.4.3, we now have  $A$  and  $T$ . From this, we can find the bolometric flux  $F_{\text{bol}}$  of the object (SI units of  $\text{W}/\text{m}^2$ ), by integrating Equation (6.14) over all wavelengths. This is:

$$\begin{aligned} F_{\text{bol}} &= \int_0^\infty f_\lambda d\lambda \\ &= \int_0^\infty AB_\lambda(T) d\lambda \\ &= \int_0^\infty \frac{2Ahc^2/\lambda^5}{\exp [hc/(\lambda k_B T)] - 1} d\lambda \\ &= \frac{(2Ahc^2)\pi^4}{15(hc/(k_B T))^4} \end{aligned} \quad (6.15)$$

The last step was done using the following equation: <sup>1</sup>:

$$\int_0^\infty \frac{1/\xi^5}{\exp [\beta/\xi] - 1} d\xi = \frac{\pi^4}{15\beta^4} \quad (6.16)$$

where  $\beta = hc/(k_B T)$ . If we also have the distance  $r$  between the Earth and the object, we can find the object's bolometric luminosity  $L_{\text{bol}}$  (SI units of  $\text{W}$ ), which is:

$$L_{\text{bol}} = 4\pi r^2 F_{\text{bol}} = \frac{8Ahc^2\pi^5r^2}{15(hc/(k_B T))^4}$$

(6.17)

---

<sup>1</sup>See full derivation by Kevin Krisciunas: <http://people.tamu.edu/~kevinkrisciunas/planck.pdf>

## 6.6 Verifying this Method with the Sun's Parameters

Now, let us verify the above method with the Sun's apparent magnitude values in several bands, to see if we can obtain a reasonable bolometric flux and luminosity value for the Sun. We will use apparent magnitude values of the Sun in the bands of KMTNet, which are Johnson  $B$ , Johnson  $V$ , and Sloan  $i$ . The data is shown in Table 6.3, obtained from Table 3 of [Willmer \(2018\)](#).

Band	Apparent Magnitude
Johnson $B$	-26.13
Johnson $V$	-26.76
Sloan $i$	-27.05

Table 6.3: The Sun's apparent magnitudes, obtained from Table 3 of [Willmer \(2018\)](#)

The blackbody fit using Equation (6.14) is shown in Figure 6.1. The location of the peak, marked by an “X”, was found using Equation (6.10). Table 6.4 compares the fitted parameters to the actual values.

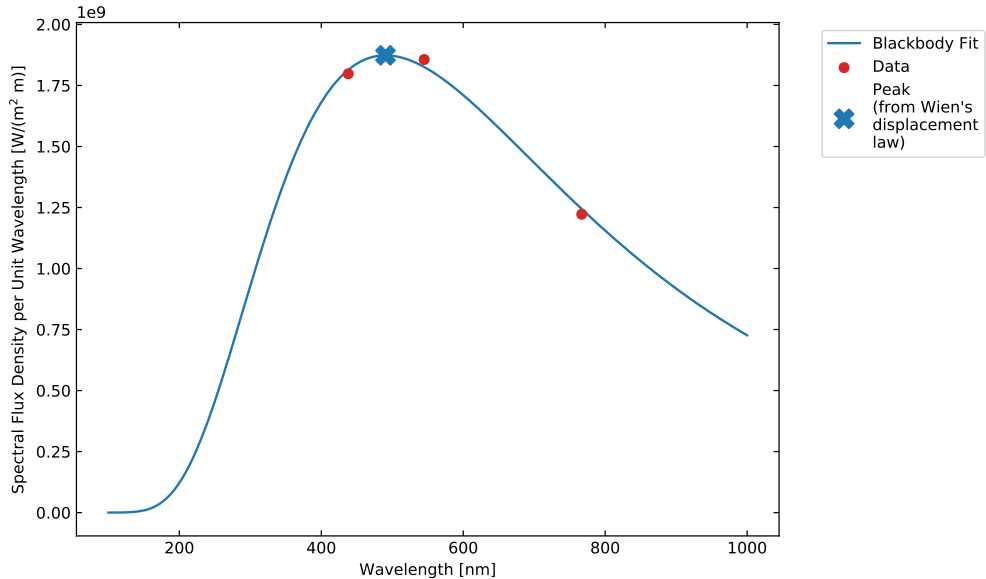


Figure 6.1: Fitted blackbody for the Sun using Equation (6.14)

The fitted value of  $T_{\text{fit}} = 5908$  K is close to the actual value of  $T_{\odot} = 5772$  K ([Prša et al. 2016](#)), within 2.4%. Likewise, the fitted value of  $A_{\text{fit}} = 6.353 \times 10^{-5}$  is close to the actual

Parameter	Fitted Value	Actual Value
$T$	5908 K	5772 K
$A$	$6.353 \times 10^{-5}$	$6.794 \times 10^{-5}$

Table 6.4: Fitted parameters of Equation (6.14) for the Sun

value within 6.5%, as:

$$A_{\text{fit}} = 6.353 \times 10^{-5} \approx 6.794 \times 10^{-5} = \frac{\pi R_{\odot}^2}{(1 \text{ AU})^2}$$

Finally, let us calculate the Sun's bolometric flux and bolometric luminosity from the fitted parameters. The results are shown in Table 6.5. The bolometric flux and luminosity are both close to the actual values within 2.7%. Interestingly, the calculated values are greater than the actual values, since  $T_{\text{fit}} > T_{\odot}$ . Nevertheless, this method gives consistent results when used on the Sun. Knowing this, we will try this method with KSP-ZN7090 next.

Variable	Calculated Value	Actual Value
Bolometric Flux $F_{\text{bol}}$	$1397.416 \text{ W/m}^2 = 1.027 F_{\odot}$	$F_{\odot} = 1361.166 \text{ W/m}^2$
Bolometric Luminosity $L_{\text{bol}}$	$3.930 \times 10^{26} \text{ W} = 1.027 L_{\odot}$	$L_{\odot} = 3.828 \times 10^{26} \text{ W}$

Table 6.5: Results of the Sun's bolometric flux and luminosity values from blackbody fitting

## 6.7 Luminosity Distance to KSP-ZN7090

Before proceeding with using this blackbody fitting method to find the bolometric light curve of KSP-ZN7090, we need the distance between Earth and KSP-ZN7090, which is the  $r$  parameter in Equation (6.17). This can obtained from the redshift  $z$  of KSP-ZN7090. Although the spectrum of KSP-ZN7090 has not been analyzed yet at the time of this work, a rough inspection of KSP-ZN7090's spectra gave a redshift estimate of  $z \sim 0.1$ . In a spectrum of KSP-ZN7090, a H $\alpha$  emission line from KSP-ZN7090's host galaxy was present at around  $\sim 7200 \text{ \AA}$ . The redshift can then be estimated as (Carroll & Ostlie 2017):

$$z = \frac{\lambda_{\text{obs}} - \lambda_{\text{rest}}}{\lambda_{\text{rest}}} \sim \frac{7200 - 6563}{6563} = 0.097 \sim 0.1 \quad (6.18)$$

where  $\lambda_{\text{rest}}$  is the rest wavelength of the H $\alpha$  line, which is  $6563 \text{ \AA}$  (Gutiérrez et al. 2017). This redshift value of 0.1 will be used for analysis in this work.

### 6.7.1 The Effect of Universal Expansion

When computing the distance to KSP-ZN7090 using the redshift  $z$ , the effect of universal expansion must be taken into account. We want to find a quantity called the luminosity distance  $D_L$  to KSP-ZN7090, given the redshift  $z$  of KSP-ZN7090. The parameter  $r$  in Equation (6.17) is  $D_L$ . The process of finding  $D_L$  will be discussed in this section. Due to universal expansion, an object currently at a proper distance  $D$  from the Earth is currently receding away from Earth at a velocity of:

$$v_{\text{rec}} = H_0 D \quad (6.19)$$

where  $H_0$  is Hubble's constant at the present time. Many different studies have measured different values of  $H_0$ , but we will use the value from [Riess et al. \(2016\)](#), which was measured using Type Ia SNe as standard candles.  $H_0 = 73.24 \pm 1.74 \text{ km s}^{-1} \text{ Mpc}^{-1}$  is the value given by [Riess et al. \(2016\)](#).  $H_0$  is the value of the Hubble parameter  $H(t)$  at the present time  $t_{\text{now}}$  (i.e.  $H_0 \equiv H(t_{\text{now}})$ ) after the beginning of the universe (we take time  $t = 0$  to be at the beginning of the universe).  $H(t)$  changes with time  $t$  and parameterizes universal expansion. Another way to parameterize universal expansion is with a dimensionless scale factor called  $R(t)$ , defined as:

$$\begin{aligned} H(t) &= \frac{1}{R(t)} \left( \frac{d}{dt} R(t) \right) = \frac{\dot{R}(t)}{R(t)} \\ R(t_{\text{now}}) &\equiv 1 \end{aligned} \quad (6.20)$$

Universal expansion is governed by the Friedmann equation, which is an ordinary differential equation for scale factor in time. This could be written as:

$$\left[ \frac{\dot{R}(t)}{R(t)} \right]^2 = [H(t)]^2 = H_0^2 \left( \frac{\Omega_{\text{rad},0}}{[R(t)]^4} + \frac{\Omega_{M,0}}{[R(t)]^3} + \frac{\Omega_{k,0}}{[R(t)]^2} + \Omega_{\Lambda,0} \right) \quad (6.21)$$

where  $\Omega_{\text{rad},0}$ ,  $\Omega_{M,0}$ ,  $\Omega_{k,0}$ , and  $\Omega_{\Lambda,0}$  are the current values of some cosmological density parameters.  $\Omega_{\text{rad},0}$  is the radiation density parameter,  $\Omega_{M,0}$  is the matter density parameter,  $\Omega_{k,0}$  is the curvature parameter, and  $\Omega_{\Lambda,0}$  is the vacuum density parameter. Different cosmological models and studies give different values for these parameters. For example, data from the Wilkinson Microwave Anisotropy Probe (WMAP) gave  $\Omega_{M,0} \approx 0.27$  and  $\Omega_{\Lambda,0} \approx 0.73$  ([Komatsu et al. 2009](#)).  $\Omega_{\text{rad},0}$  can have several parts, and more details can be found in [Komatsu et al. \(2009\)](#). Let us use the WMAP values in [Komatsu et al. \(2009\)](#), also assuming that the

universe is flat, having no curvature so that  $\Omega_{k,0} = 0$ .

Now, suppose that electromagnetic radiation was emitted from a certain object at a time  $t_e$  after the beginning of the universe. Suppose this object has a current observed redshift of  $z$  at the current time  $t_{\text{now}}$ . Then redshift and scale factor have the relationship (Copeland et al. 2006):

$$1 + z = \frac{R(t_{\text{now}})}{R(t_e)} = \frac{1}{R(t_e)} \quad (6.22)$$

Then taking  $t = t_e$ , we can substitute Equation (6.22) into the Equation (6.21) to obtain a version of the Friedmann equation written in terms of redshift rather than time:

$$[H(z)]^2 = H_0^2 (\Omega_{\text{rad},0}(1+z)^4 + \Omega_{M,0}(1+z)^3 + \Omega_{k,0}(1+z)^2 + \Omega_{\Lambda,0}) \quad (6.23)$$

### 6.7.2 Comoving Distance

Due to universal expansion, the distance between Earth and an object is changing over time. Hence, there are different ways to describe the distance between two points. In the literature, several distance measures have been defined. One of these measures is called the comoving distance  $D_c$ , which is a constant and unchanging measure quantifying the distance between Earth and this object. If two objects are moving solely due to universal expansion, then their comoving distance will be constant in time (Hogg 1999). The comoving distance is defined as:

$$D_c \equiv \frac{c}{R(t_{\text{now}})} \int_{t_e}^{t_{\text{now}}} \frac{1}{R(t)} dt \quad (6.24)$$

Following the procedure in Davis & Lineweaver (2004),  $D_c$  can be expressed in terms of redshift  $z$ , by making a change of variable from time to redshift using Equation (6.22). The result is:

$$\begin{aligned} D_c(z) &= \frac{c}{R(t_{\text{now}})} \int_0^z \frac{1}{H(\xi)} d\xi \\ &= c \int_0^z \frac{1}{H(\xi)} d\xi \\ &= c \int_0^z \frac{1}{H_0 \sqrt{(\Omega_{\text{rad},0}(1+\xi)^4 + \Omega_{M,0}(1+\xi)^3 + \Omega_{k,0}(1+\xi)^2 + \Omega_{\Lambda,0})}} d\xi \end{aligned} \quad (6.25)$$

where Equation (6.23) was substituted in the last step.

### 6.7.3 Luminosity Distance

Another distance measure is called the luminosity distance  $D_L$ , which is what we are trying to find for KSP-ZN7090. In Minkowski spacetime, if an object has an absolute bolometric luminosity of  $L_{\text{bol}}$  and a bolometric flux of  $F_{\text{bol}}$ , then the luminosity distance is defined as (Copeland et al. 2006; Hogg 1999):

$$D_L \equiv \sqrt{\frac{L_{\text{bol}}}{4\pi F_{\text{bol}}}} \quad (6.26)$$

This luminosity distance  $D_L$  is a quantity that satisfies the luminosity-flux relationship, while already accounting for universal expansion and the decrease in photon energy due to redshifted wavelengths. In terms of redshift  $z$ , the luminosity distance is (Copeland et al. 2006):

$$D_L(z) = R(t_{\text{now}})(1+z)D_c(z) = (1+z)D_c(z) \quad (6.27)$$

### 6.7.4 Results

Using the cosmological parameters in Komatsu et al. (2009), the value of the Hubble constant from Riess et al. (2016), and an assumed redshift of  $z = 0.1$  for KSP-ZN7090, the luminosity distance for KSP-ZN7090 was found to be  $D_L = 440.923 \text{ Mpc} = 1.36055 \times 10^{25} \text{ m}$ . This is the value which will be used for  $r$  in Equation (6.17). A plot of the corresponding  $D_c$  and  $D_L$  values for redshifts  $z \in [10^{-4}, 10^2]$  is shown in Figure 6.2.

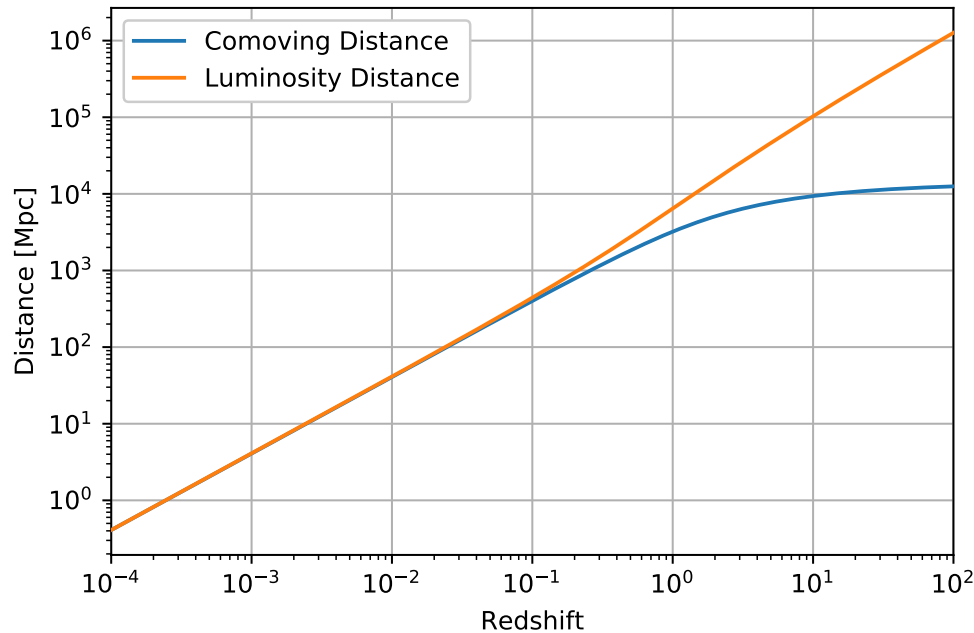


Figure 6.2: Comoving distance  $D_c$  and luminosity distance  $D_L$  evaluated using Equations (6.25) and (6.27) respectively. Parameters from Komatsu et al. (2009) and Riess et al. (2016) were used. The distances shown in this plot are in megaparsecs ( $1 \text{ Mpc} \approx 3.08568 \times 10^{22} \text{ m}$ ).

## 6.8 Blackbody Fitting for KSP-ZN7090

Equipped with the knowledge of  $r = D_L$  and the knowledge that the blackbody fitting method works for the Sun, let us now try this method for KSP-ZN7090. Let us work in wavelength coordinates, and use spectral flux density per unit wavelength values from Table 6.2 when possible, in order to avoid systematic errors in converting between  $f_{\nu,0}$  and  $f_{\lambda,0}$ . Note that the light curves need to be linearly interpolated so that the blackbody fitting is applied to data at the same epochs (see Section 7.2.3).

### 6.8.1 Fitting using Nonlinear Least Squares

First, let us use nonlinear least squares fitting to fit Equation (6.14) to each epoch. Blackbody fits for KSP-ZN7090 at two different epochs are shown in Figure 6.3 for example. These fits were done using nonlinear least squares fitting. A plot of the resulting fitted blackbody temperature and bolometric luminosity values as functions of time are shown in Figure 6.4.

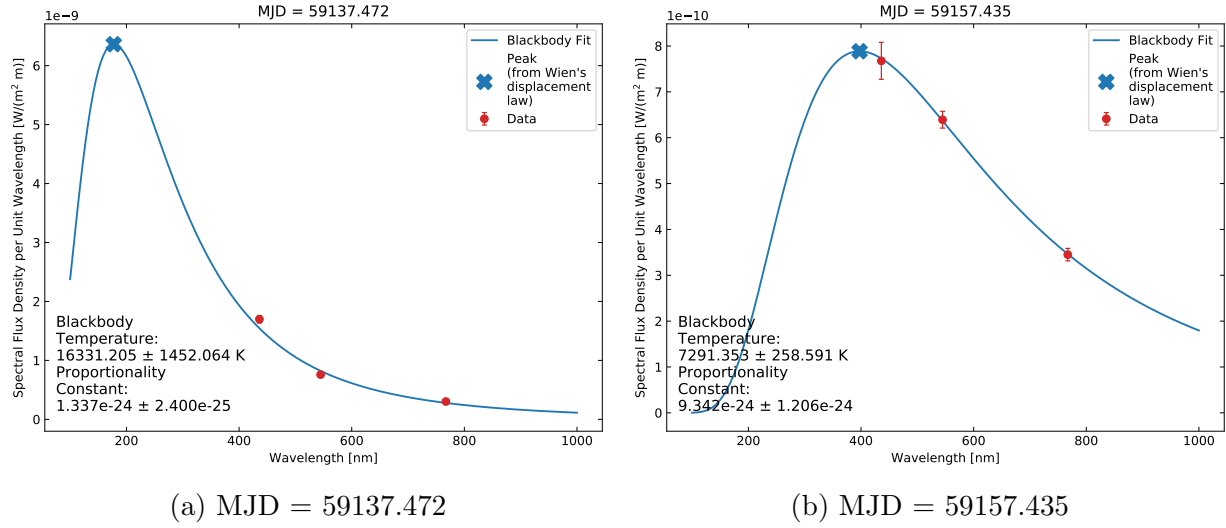


Figure 6.3: Blackbody fits to KSP-ZN7090 at two different epochs, using nonlinear least squares fitting

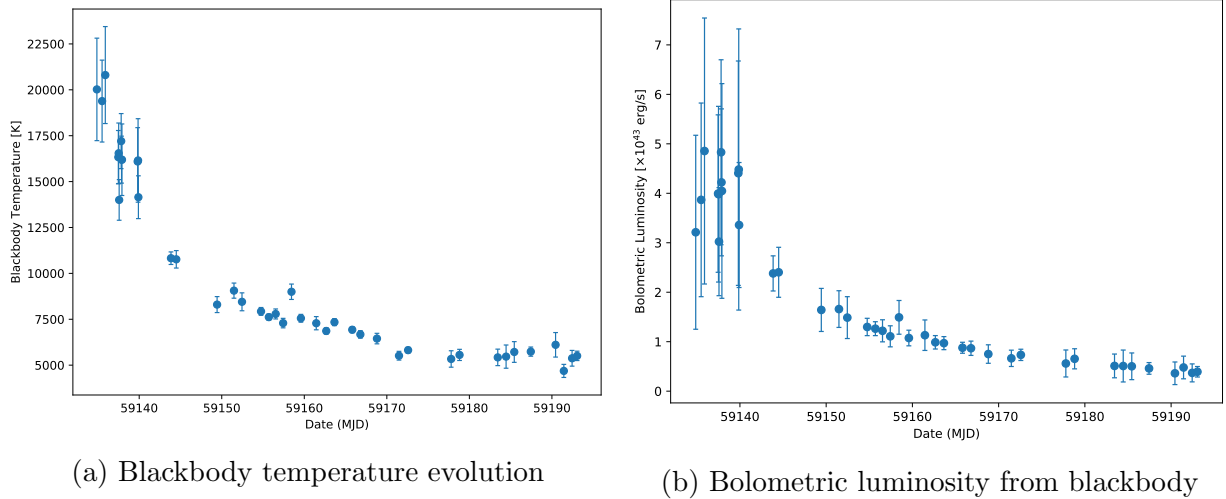


Figure 6.4: Blackbody temperature and bolometric luminosity of KSP-ZN7090, using non-linear least square fitting

In order to estimate the uncertainties in the fit parameters ( $T$  and  $A$ ), the Jacobian matrix  $J$  outputted by nonlinear least squares was used. Using the Gauss-Newton approximation (Triggs et al. 2000), the Hessian matrix  $H$  could be approximated as  $H = J^T J$ . The covariance matrix is  $H^{-1}$ , and then the diagonal entries of the covariance matrix are the uncertainty values. However, the uncertainty values computed from this method were very large or small for some reason (e.g. large  $A$  uncertainty and small  $T$  uncertainty). This resulted in large error bars as shown in Figure 6.4. It is possible that this method of

estimating uncertainties may not be too reliable in this application, and hence another method was attempted.

### 6.8.2 Fitting using Monte Carlo Simulations of Nonlinear Least Squares

In order to better estimate the uncertainties, the method of using Monte Carlo simulations was also attempted. Each data point was shifted randomly between its uncertainty range, and then a blackbody was fitted to the data. Each data point was modelled as a Gaussian distribution centred about its spectral flux density value with standard deviation equal to its spectral flux density uncertainty. Then each Monte Carlo trial consisted of randomly drawing a value from each Gaussian distribution, and then applying a blackbody fit to these drawn values using nonlinear least squares. 1000 Monte Carlo trials were done for each epoch. Blackbody fits for KSP-ZN7090 using this method at two different epochs (the same two epochs as in Figure 6.3) are shown in Figure 6.5. Notice how this method of using Monte Carlo simulations gives a range of fits. The uncertainties can then be taken as the variances of the fitted parameters from all the Monte Carlo trials.

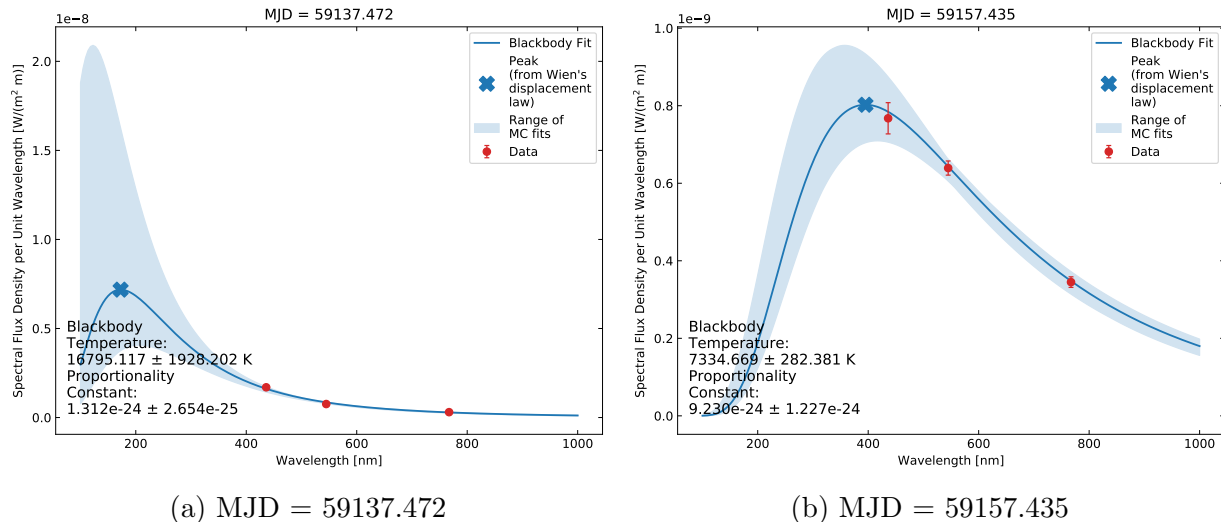


Figure 6.5: Blackbody fits to KSP-ZN7090 at two different epochs, using Monte Carlo simulations of nonlinear least squares fitting; compare this with Figure 6.3

A plot of the resulting fitted blackbody temperature and bolometric luminosity values as functions of time are shown in Figure 6.4. However, again the uncertainties were very large, mainly for the  $A$  parameter. This is reflected in the large uncertainties of the computed bolometric light curve in Figure 6.6b, especially for the early epochs.

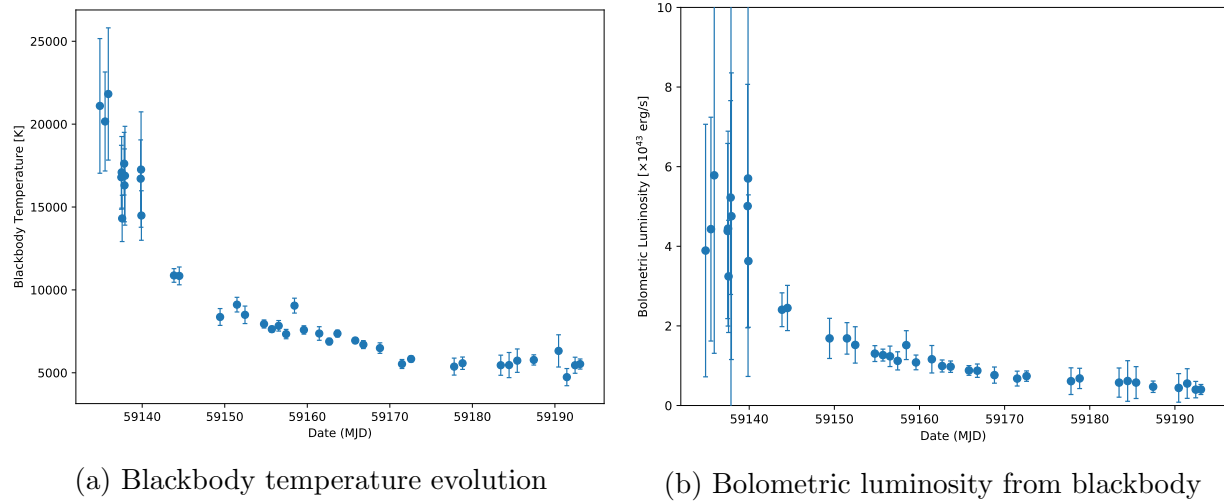


Figure 6.6: Blackbody temperature and bolometric luminosity of KSP-ZN7090, using Monte Carlo simulations of nonlinear least square fitting; compare this with Figure 6.4

### 6.8.3 Limitations of Blackbody Fitting Method for Finding Bolometric Light Curve

As seen from the figures in Section 6.8.2, the results from blackbody fitting still have issues. Upon closer inspection of the blackbody fits conducted using Monte Carlo simulations, a problem which was mentioned in Section 2.7.1 could be seen. Notice that in Figure 6.5a, the range of blackbody fits increases greatly in the UV regime. If the fitted blackbody is integrated over the UV regime, this integration is being performed over an extrapolated region, which may give unreliable results. Hence, there is high uncertainty associated with this integration, and the results would have high uncertainty.

The problem is that there are only 3 data points at each epoch, and so the blackbody function is not well constrained, and could produce bad fits at times. To be specific, often-times, the peak of the blackbody is not well constrained by the 3 data points, in that points are not on both sides of the peak. Hence, as seen in the Monte Carlo simulations, there are many blackbody functions with different peak values which can satisfy the 3 points, therefore resulting in a high uncertainty. This was particularly prevalent for the earlier epochs, which have higher uncertainties as seen in both Figures 6.6b and 6.4b. This is because at the early epochs, the SN is brighter and near its peak brightness. Hence, the expected blackbody spectrum is bluer, with a peak more leftwards to the UV regime. As a result, data points will not be able to be on both sides of the peak, and the peak will not be well constrained,

as shown in Figure 6.5a for example.

Usually, this blackbody method would be used for SN with observations in a larger number of bands, so that there could be more points for fitting. For example, [Tartaglia et al. \(2021\)](#) used this method with 11 bands for the Type II SN 2017ahn. For the case of KSP-ZN7090, with only 3 bands, the method of bolometric corrections may be more suitable for finding the bolometric light curve. This will be discussed in Chapter 7. Nevertheless, while the bolometric light curves in Figures 6.6b and 6.4b may not be usable due to the high uncertainties, they are still useful in providing a rough estimate of the bolometric luminosity. Most of the bolometric luminosity values in Figures 6.6b and 6.4b are on the order of  $10^{43}$  erg/s, which is reasonable for Type II SNe.

# Chapter 7

## Bolometric Light Curve from Bolometric Corrections

### 7.1 Overview

In this chapter, the method of bolometric corrections for constructing bolometric light curves will be discussed. Compared to the blackbody fitting method in Chapter 6, this method is more suitable if there is only data in a few bands, as discussed in Section 6.8.3 and as briefly touched upon in Section 2.7.

### 7.2 Method of Bolometric Corrections

#### 7.2.1 Equations

Given the apparent magnitude  $m_\xi$  of an object in band  $\xi$ , its bolometric apparent magnitude  $m_{\text{bol}}$  could be found by applying a bolometric correction  $\text{BC}_\xi$ . Let us call the band which we would like to apply the bolometric correction to, the target band  $\xi$ . The bolometric correction  $\text{BC}_\xi$  to target band  $\xi$  is defined as (Lyman et al. 2013):

$$\text{BC}_\xi \equiv m_{\text{bol}} - m_\xi \quad \Rightarrow \quad m_{\text{bol}} = m_\xi + \text{BC}_\xi \quad (7.1)$$

The bolometric correction to a particular target band  $\xi$  can be expressed as a polynomial function of colour difference between two bands  $x$  and  $y$ :

$$\text{BC}_\xi = \sum_{k=0}^n c_k (m_x - m_y)^k \quad (7.2)$$

Usually, the target band  $\xi$  is either  $x$  or  $y$ . The coefficients  $c_k$ ,  $k = 0, \dots, n$  are determined empirically by fitting light curve data from SNe. Different models in the literature give different coefficients  $c_k$ , and have different sets of coefficients for different phases of the light curves (e.g. see Martinez et al. (2021), Lyman et al. (2013), and Bersten & Hamuy (2009)). Sometimes, an uncertainty value  $\sigma$  is also provided for the  $BC_\xi$  fit, as in Martinez et al. (2021). Sometimes, an RMS error value is provided instead for the  $BC_\xi$  fit, as in Lyman et al. (2013).

### 7.2.2 Uncertainty Estimation

To estimate the uncertainty in  $m_{\text{bol}}$ , Monte Carlo simulations were used. There are three sources of uncertainty for  $m_{\text{bol}}$ , which are the uncertainty in  $m_x$ , the uncertainty in  $m_y$ , and  $\sigma$ . In order to estimate the uncertainties, the following process was done. Each data point in the light curve was modelled as a Gaussian distribution centred about its magnitude value, with standard deviation equal to its magnitude uncertainty. This was done for both the  $m_x$  and  $m_y$  data points. Then, each Monte Carlo trial consisted of randomly drawing a value from each Gaussian distribution, and then applying Equation (7.1), with Equation (7.2) directly substituted in place of  $BC_\xi$ . The resulting uncertainty was taken to be the spread in the  $m_{\text{bol}}$  values from the Monte Carlo simulations. This process was done in Sections 7.5.1 and 7.5.2, with 1 million Monte Carlo trials conducted each time.

In order to account for the effects of  $\sigma$ , another Gaussian distribution can be constructed, centred about 0 with standard deviation equal to  $\sigma$ . Then in each Monte Carlo trial, a value can be drawn from this Gaussian distribution and added to the result of Equation (7.1). Monte Carlo simulations including  $\sigma$  were attempted, but they will not be reported in this work because  $\sigma$  is often ignored in practice, since it is a systematic uncertainty which is not too significant.

### 7.2.3 Light Curve Interpolation

In order to apply this method, the  $m_x$  and  $m_y$  values must be at the same epochs. However, the KMTNet telescopes do not acquire images in multiple bands simultaneously, but rather takes images in one band at a time, and then changes filters. Oftentimes, a telescope acquires a  $B$  band image, then  $V$  band, and then  $I$  band, changing filters in between. There are also times when 3 sets of images are not acquired (e.g.  $B$  band and  $V$  band images are acquired, but an  $I$  band image is not acquired due to time constraints). Thus, the  $m_x$  and  $m_y$  values are at different epochs. In order to get these values to be at the same epoch,

the light curve was linearly interpolated so that the  $m_x$  and  $m_y$  values are at the same epochs.

For example, suppose we want to find the bolometric correction to target band  $\xi = V$ . In Martinez et al. (2021), coefficients  $c_k$  are provided for the condition  $x = B$ ,  $\xi = y = V$  in Equation (7.2). Since the bolometric correction is being added to the magnitude values of the target band  $\xi = y = V$  (see Equation (7.1)), the magnitude values for the non-target band  $x = B$  need to be interpolated. A linear interpolation of the  $B$  band light curve is shown in Figure 7.1. The black curve with “X” markers is the interpolated  $B$  band light curve. The “X” markers are at the same epochs as the  $V$  band data, and these values can be used with Equation (7.2)).

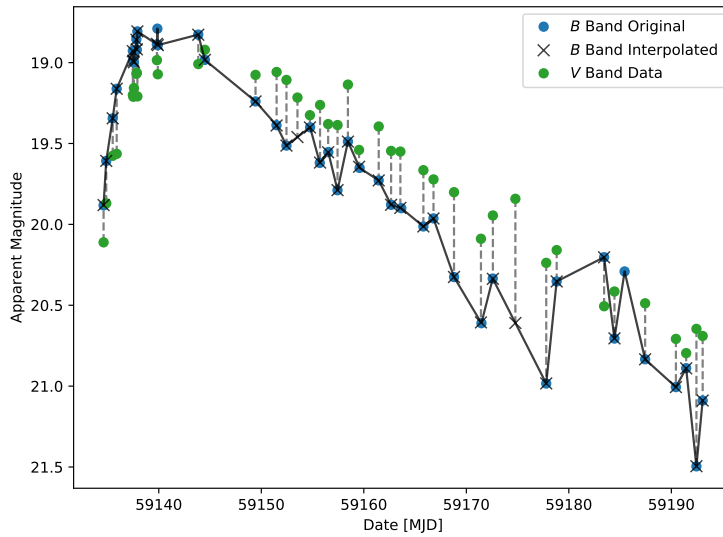


Figure 7.1: Linearly interpolated light curve for band  $x = B$ , interpolated from times of band  $\xi = y = V$

## 7.3 A More Complete Description of Light Curve Rise and Phases

### 7.3.1 Light Curve Sources

Before proceeding with applying bolometric corrections using the method in Section 7.2, we need to first identify the different light curve phases in the light curve of KSP-ZN7090. That is, we need to know which parts of KSP-ZN7090’s light curve correspond to the light curve phases discussed in Section 2.3.1. As mentioned in Sections 2.7.2 and 7.2, different light curve phases, which correspond to different sources powering the light curve, require different

bolometric correction coefficients  $c_k$ . Recall that [Lyman et al. \(2013\)](#) splits up the bolometric corrections into 2 phases: the cooling phase and radiatively-/recombination-powered phase, while [Martinez et al. \(2021\)](#) splits up the bolometric corrections into 3 phases: the cooling phase, recombination phase, and tail (nebular) phase (which are the same 3 phases discussed in Section 2.3.1).

While a description of the different light curve phases was given in Section 2.3.1, that description was simplified and corresponded to Type II SNe with a rise dominated by shock cooling emission. However, there are other possibilities, and a more complete description will be given here. A SN’s light curve rise is mainly caused by two sources ([Piro & Nakar 2013](#)): (1) shock cooling emission and (2) radioactive decay of  $^{56}\text{Ni}$ . The different combinations of these two sources will lead to 3 scenarios for the rise of a SN’s light curve, which will be discussed in Section 7.3.2. A brief description of shock cooling emission and radioactive decay is presented below.

### 7.3.1.1 Shock Cooling Emission

As the shock (see Section 2.2.1) is moving outwards, it deposits energy into the SN’s envelope and material. This material is called “shock-heated”. Then as this heated material expands and cools, photons are diffused out of this heated material, causing a sharp rise in the SN’s light curve ([Piro et al. 2021](#)).

### 7.3.1.2 Radioactive Decay of $^{56}\text{Ni}$

As the shock is moving outwards, its interaction with surrounding material produces radioactive isotopes. The radioactive decay of these isotopes releases energy which is deposited into the SN remnant, and then radiated away ([Carroll & Ostlie 2017](#)). While several different isotopes are produced,  $^{56}\text{Ni}$  is the most abundant product ([Truran et al. 2012](#)). A more detailed discussion can be found in [Piro & Nakar \(2013\)](#).

## 7.3.2 Three Scenarios for Light Curve Rise

### 7.3.2.1 Light Curve Rise Dominated by Shock Cooling Emission

If shock cooling emission starts at around time as radioactive decay, then the rise of the light curve could be dominated by cooling of the shocked material, and this would continue beyond the peak of the light curve. Once the shocked material has been cooled to some extent, then the light curve will either be sustained by hydrogen recombination for Type

II-P SNe (hydrogen recombination reduces opacity of material and allows photons to escape; see Section 2.3.1.2), or energy released by radioactive decay for Type II-L SNe. This is what is seen in Figure 8 of Martinez et al. (2021) for Type II-P SNe. In this case, bolometric corrections for the cooling phase should be used up until the plateau phase (for Type II-P SNe) or nebular phase (for Type II-L SNe). This scenario corresponds to the description presented in Section 2.3.1.

### 7.3.2.2 Light Curve Rise Powered by Radioactive Decay Only

In this scenario, the light curve's rise is powered only by radioactive decay, and contributions from shock cooling emission are not as significant. The light curve rises slower compared to one which has the scenario in Section 7.3.2.1. In this case, bolometric corrections for the radiatively-/recombination-powered phase in Lyman et al. (2013) should be used. This scenario is more common for Type I SNe.

### 7.3.2.3 Double Peaked Light Curve from both Shock Cooling Emission and Radioactive Decay

It is possible that shock cooling emission starts earlier than radioactive decay, and so the light curve could be double peaked in this case. The first peak would be powered by shock cooling emission and the second peak by radioactive decay. If the first peak is too early to observe, and only the second peak is seen, then bolometric corrections for the cooling phase should not be used at all, since the first detection was roughly after the cooling phase. If both peaks are visible, then bolometric corrections for the cooling phase should be used for the first peak, and bolometric corrections for the radiatively-/recombination-powered phase in the second peak. An example of a SN with a double peaked light curve belonging to this scenario is the Type IIb SN 2016gkg (Arcavi et al. 2017; Tartaglia et al. 2017).

## 7.4 Phases in the Light Curve of KSP-ZN7090

### 7.4.1 Models to Identify Light Curve Phases

Now, let us identify which phases are in the light curve of KSP-ZN7090. From Figure 3.16, we see that KSP-ZN7090's light curve is not double peaked, and so the scenario in Section 7.3.2.3 is not applicable. KSP-ZN7090 has the scenario in either Section 7.3.2.2 or Section 7.3.2.1. Given KSP-ZN7090's fast rise as seen in Section 5.3, it is reasonable to infer here that KSP-ZN7090's rise is powered by shock cooling emission (the scenario in Section 7.3.2.1). Going along with this scenario, KSP-ZN7090 will enter the nebular phase after the

cooling phase, since KSP-ZN7090 is not a Type II-P SNe. The question is whether or not KSP-ZN7090 has entered nebular phase in its light curve.

In Martinez et al. (2021), identifying the different light curve phases was done using the method in Anderson et al. (2014). In this method, a model was fitted to the post-peak  $V$  band light curves of Type II-P SNe in order to identify 3 sections of constant slope in the light curves. These 3 sections correspond to the cooling phase, plateau phase, and nebular phase (Martinez et al. 2021). It is sufficient to fit the  $V$  band light curve only, because the  $V$  band light curve is a “very close proxy” for the bolometric light curve (Bersten & Hamuy 2009). This model to fit the  $V$  band light curve is basically a piecewise function of 3 straight lines (each line represents one of the light curve phases) but with some modifications. The first and second straight lines, which represent the cooling phase and plateau phase, are a simple piecewise function. The transition between the second and third straight lines, which represent the plateau phase and the nebular phase, is represented by another model developed by Olivares E. et al. (2010) for the bolometric light curves of Type II-P SNe during the plateau phase and nebular phase. The model of Olivares E. et al. (2010) consists of the sum of 3 different functions, which are: a Fermi-Dirac function (for the transition), a straight line (for the nebular phase), and a Gaussian function (for the plateau phase).

In the case of KSP-ZN7090, there is no plateau, and so the transition model described by Olivares E. et al. (2010) is not applicable. Adopting a similar model as in Anderson et al. (2014), it seems reasonable to fit a piecewise linear function with 2 sections of constant slope, in order to identify the cooling phase and nebular phase in KSP-ZN7090’s post-peak light curve. The first section would represent the cooling phase and the second section would represent the nebular phase. The results of this fitting to KSP-ZN7090’s post-peak  $V$  band light curve, using Monte Carlo simulations, are shown in Figure 7.2. The light curve decline rates for the fitted piecewise linear function are reported in Table 7.1, where a comparison is also made with values in the literature.

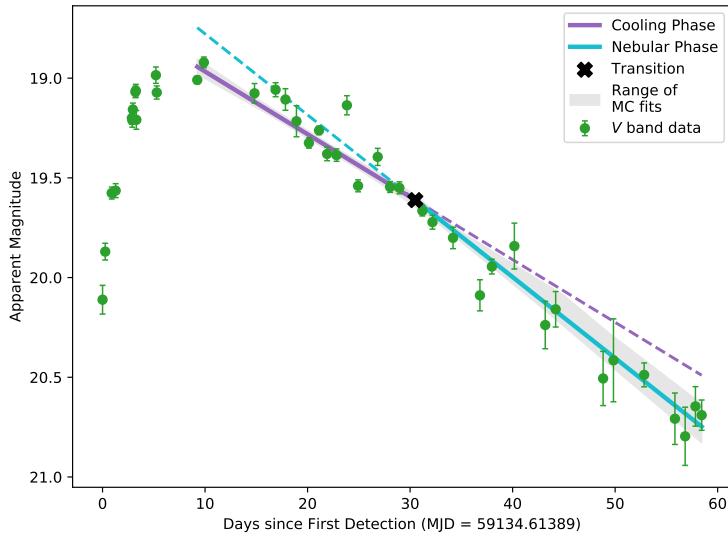


Figure 7.2: Piecewise linear function with 2 sections of constant slope, fitted to the  $V$  band light curve of KSP-ZN7090. Comparing with the values in Table 7.1, we can conclude that this fit does not make sense and that the nebular phase is not present in this light curve.

Phase	Light curve decline rate [mag per 100 days]		
	KSP-ZN7090 $V$ band piecewise linear fit	Martinez et al. (2021) Bolometric	Anderson et al. (2014) $V$ band
Cooling	3.144	4.59 (MAD = 2.84)	2.65 ( $\sigma = 1.50$ )
Nebular	4.066	1.38 (MAD = 0.62)	1.47 ( $\sigma = 0.82$ )

Table 7.1: Comparison of light curve decline rates for the cooling phase and nebular phase, for a piecewise linear model fitted to KSP-ZN7090 (in Figure 7.2), and values from Martinez et al. (2021) and Anderson et al. (2014). Martinez et al. (2021) reports the median decline rate for the bolometric light curves of 74 Type II SNe, and Anderson et al. (2014) reports the mean decline rate for the  $V$  band light curves of 115 Type II SNe. These values are presented in this table. MAD is median absolute deviation and  $\sigma$  is standard deviation.

### 7.4.2 Results

By comparing the line curve decline rates in the piecewise linear fit to the decline rates in Table 7.1, we see that the nebular phase part of the fit is inconsistent with the decline rates in the literature. The turquoise line in Figure 7.2 is too steep, even steeper than the purple line representing the cooling phase, and this should not happen. Hence the turquoise line does not represent the nebular phase. By looking at Figure 7.2, we can conclude that the nebular phase is not present in the light curves of KSP-ZN7090 yet. Indeed, nebular phase for Type II SNe usually starts later, hundreds of days after the explosion (Dessart & Hillier

2020). Here, the light curve only goes up to  $\sim 60$  days, and so nebular phase has not started yet. Unfortunately, a consequence of this is that most of the light curve models mentioned in Section 2.8 (used to estimate KSP-ZN7090’s physical parameters from its bolometric light curve) cannot be used yet, since they require the nebular phase of the light curve. Once KSP-ZN7090’s bolometric light curve is constructed (in the next sections), other light curve models, more applicable to the earlier parts of SN light curves, would need to be used instead to find KSP-ZN7090’s physical parameters. These will be discussed later in Chapters 8 and 9.

In addition, the fitted piecewise linear function has two lines which are very similar in slope, suggesting that the light curve only contains only one phase. We have ruled out the plateau phase from Martinez et al. (2021) since KSP-ZN7090 is not a Type II-P SN, and also the nebular phase of Martinez et al. (2021). Thus, the phase present in the light curve is either a cooling phase (from Martinez et al. (2021) or Lyman et al. (2013)) or a radiatively-/recombination-powered phase (from Lyman et al. (2013)). In the former case, this corresponds to the scenario in Section 7.3.2.1 with a shock cooling emission powered peak. In the latter case, this corresponds to the scenario in Section 7.3.2.2 with a radioactive decay powered peak. Bolometric corrections will be applied assuming these phases in the next section.

## 7.5 Applying the Bolometric Corrections

This section presents the results of applying bolometric corrections using the method in Section 7.2, with the coefficients in Martinez et al. (2021) and Lyman et al. (2013). In addition to the bolometric light curve, intermediary figures (showing  $BC_\xi$  versus  $m_x - m_y$ ,  $BC_\xi$  versus  $t$ , and  $m_x - m_y$  versus  $t$ ) are also shown. Note that both Martinez et al. (2021) and Lyman et al. (2013) provide colour ranges for their bolometric correction, which are the ranges of colours they used to derive their coefficients. This is shown by the grey shaded regions in the figures. Colour values outside of the ranges will have bolometric corrections which are extrapolated from the models.

### 7.5.1 Martinez et al. (2021) Method

This section presents the results of applying bolometric corrections using the coefficients in Martinez et al. (2021). As discussed in Section 7.4.2, only the cooling phase of Martinez et al. (2021) may be applicable to KSP-ZN7090. Coefficients from Table 4 of Martinez et al.

(2021) are used. Here, we have  $\xi = y = V$  and  $x = B$ , following the convention in Section 7.2.1. The results are shown in Figure 7.3.

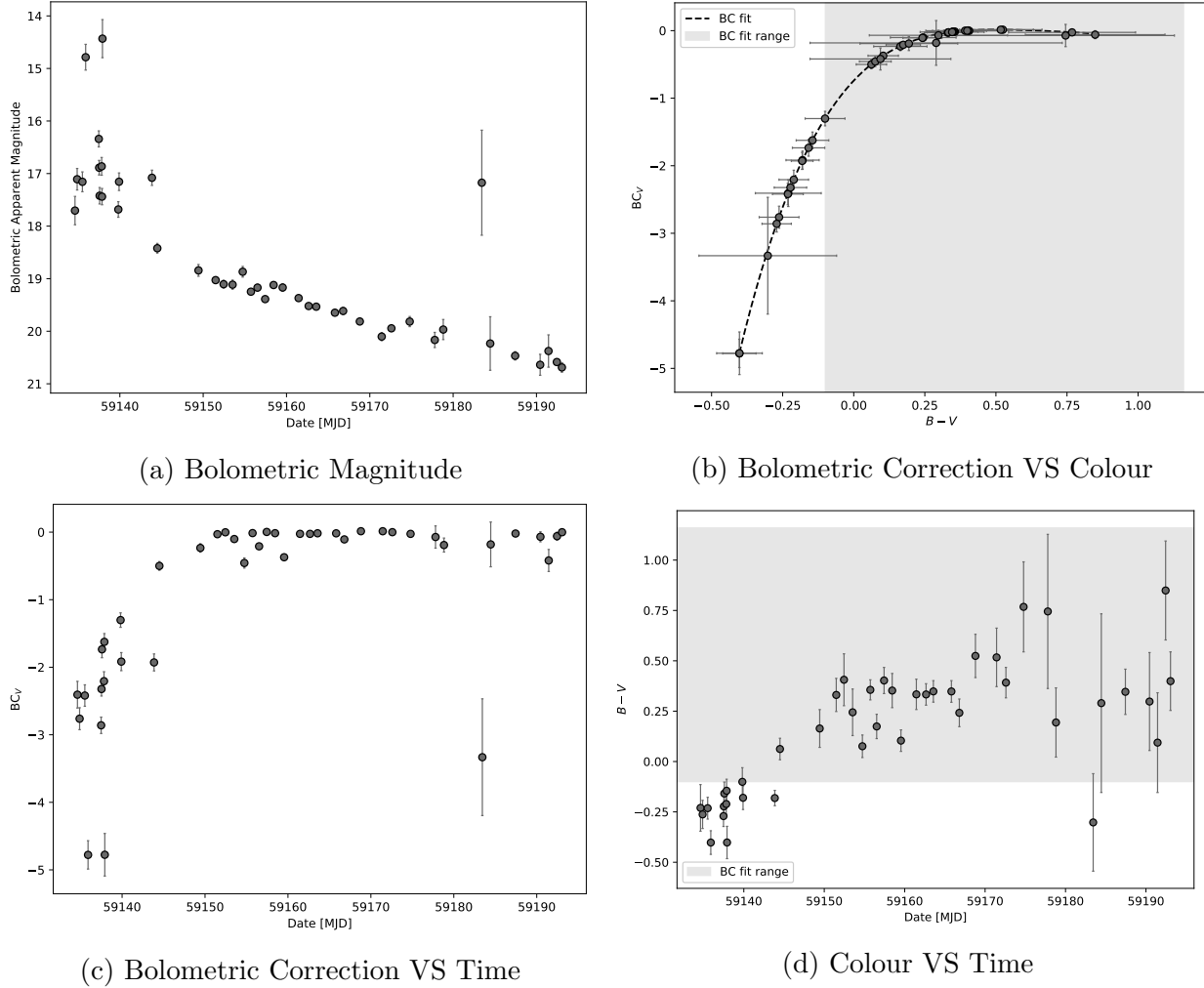


Figure 7.3: Bolometric corrections using the cooling phase in Martinez et al. (2021);  $\xi = y = V$ ,  $x = B$

### 7.5.2 Lyman et al. (2013) Method

This section presents the results of applying bolometric corrections using the coefficients in Lyman et al. (2013). As discussed in Section 7.4.2, both the cooling phase and radiatively-/recombination-powered phase of Lyman et al. (2013) may be applicable to KSP-ZN7090. Coefficients for the radiatively-/recombination-powered phase and cooling phase are found in Tables 3 and 4 respectively of Lyman et al. (2013). While Martinez et al. (2021) only allows one option for  $\xi$ ,  $x$ , and  $y$  among the Johnson filters, Lyman et al. (2013) gives more

options. In the figures below,  $\xi = x = B$  with  $y = V$  and  $y = I$  are shown. For conciseness, intermediary figures are only shown for  $y = V$ .

### 7.5.2.1 Lyman et al. (2013) Cooling Phase, $\xi = x = B$ , $y = V$

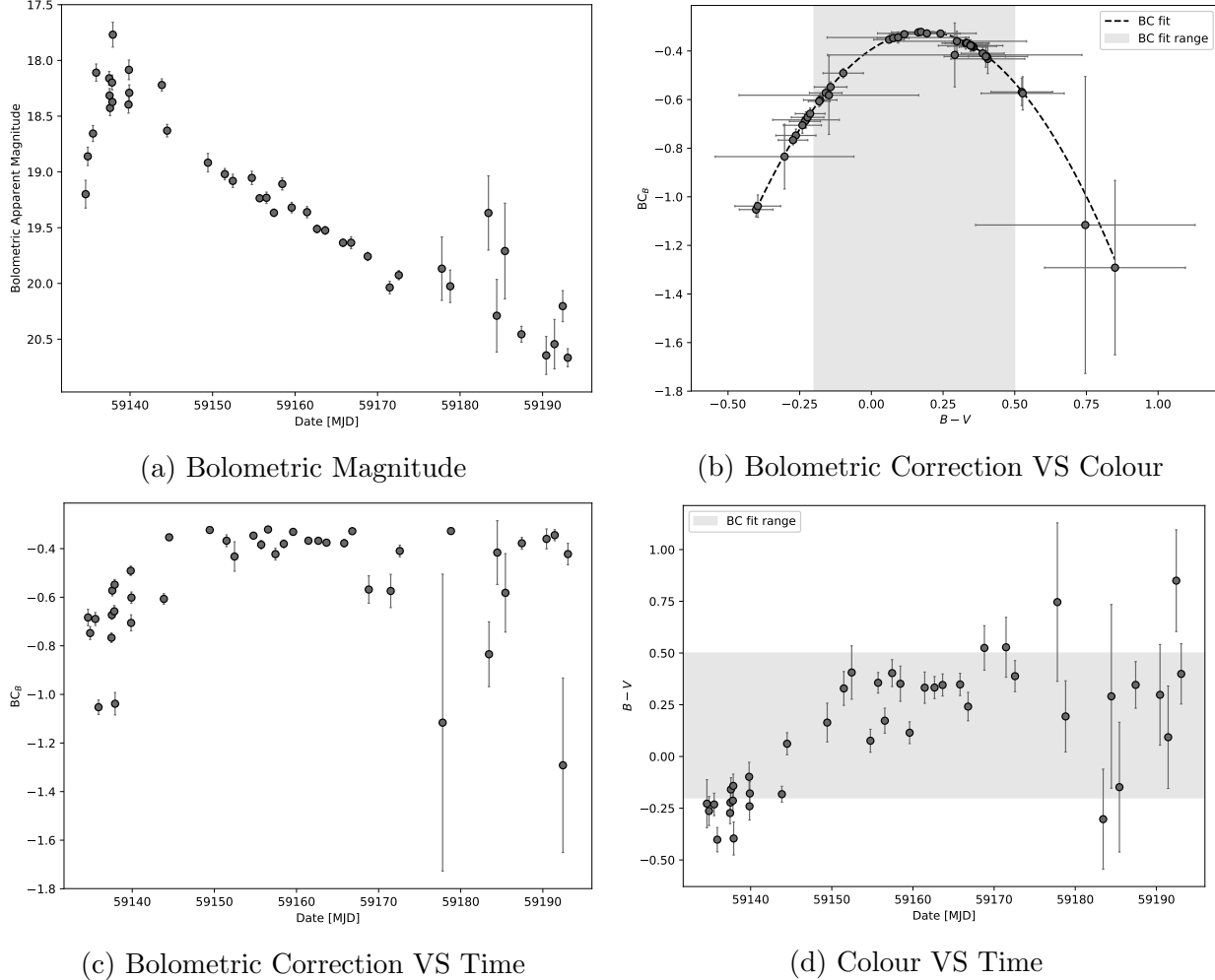


Figure 7.4: Bolometric corrections using the cooling phase in Lyman et al. (2013);  $\xi = x = B$ ,  $y = V$

### 7.5.2.2 Lyman et al. (2013) Radiatively-/Recombination-Powered Phase, $\xi = x = B, y = V$

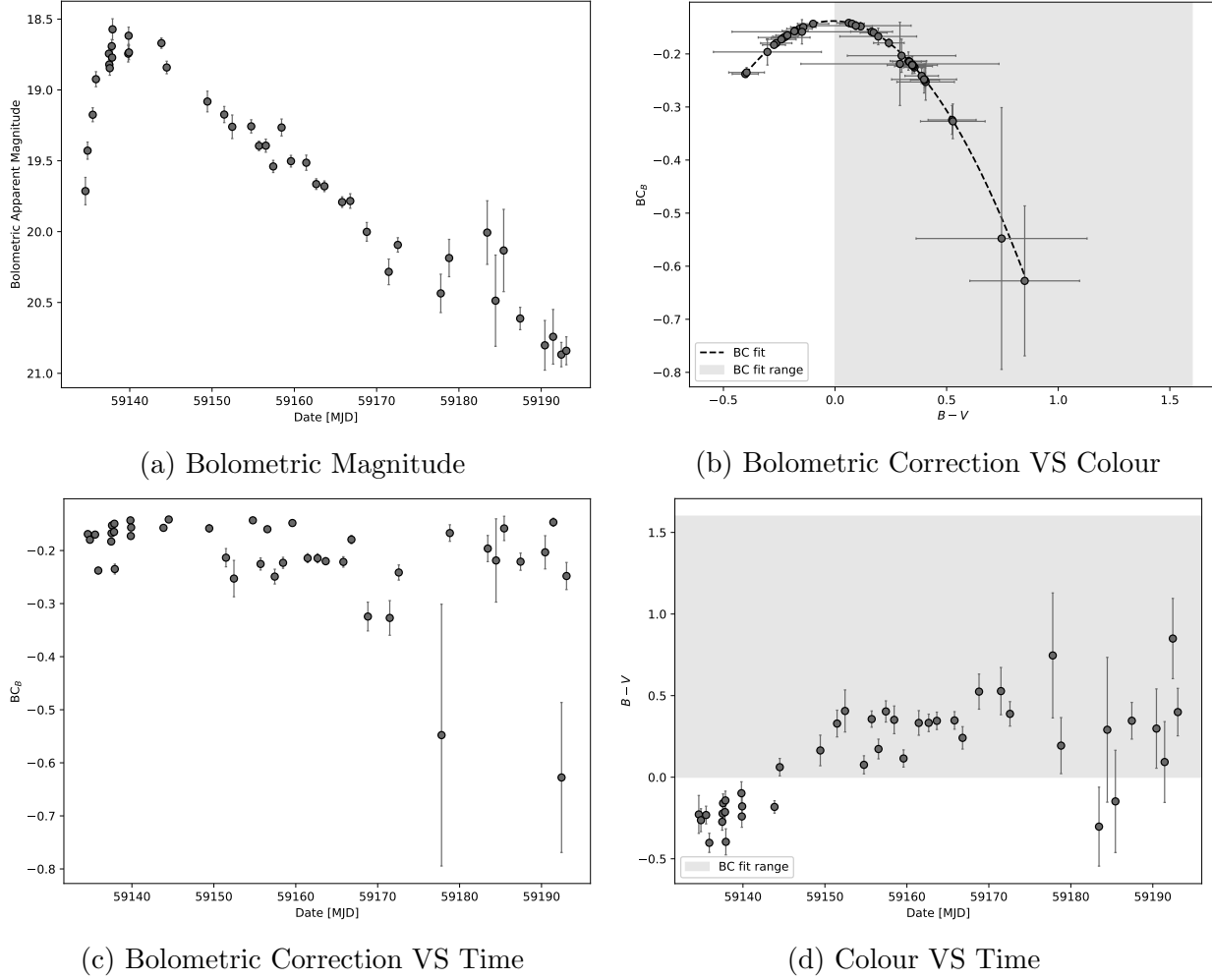


Figure 7.5: Bolometric corrections using the radiatively-/recombination-powered phase in Lyman et al. (2013);  $\xi = x = B, y = V$

### 7.5.2.3 All Results of Lyman et al. (2013) Bolometric Correction

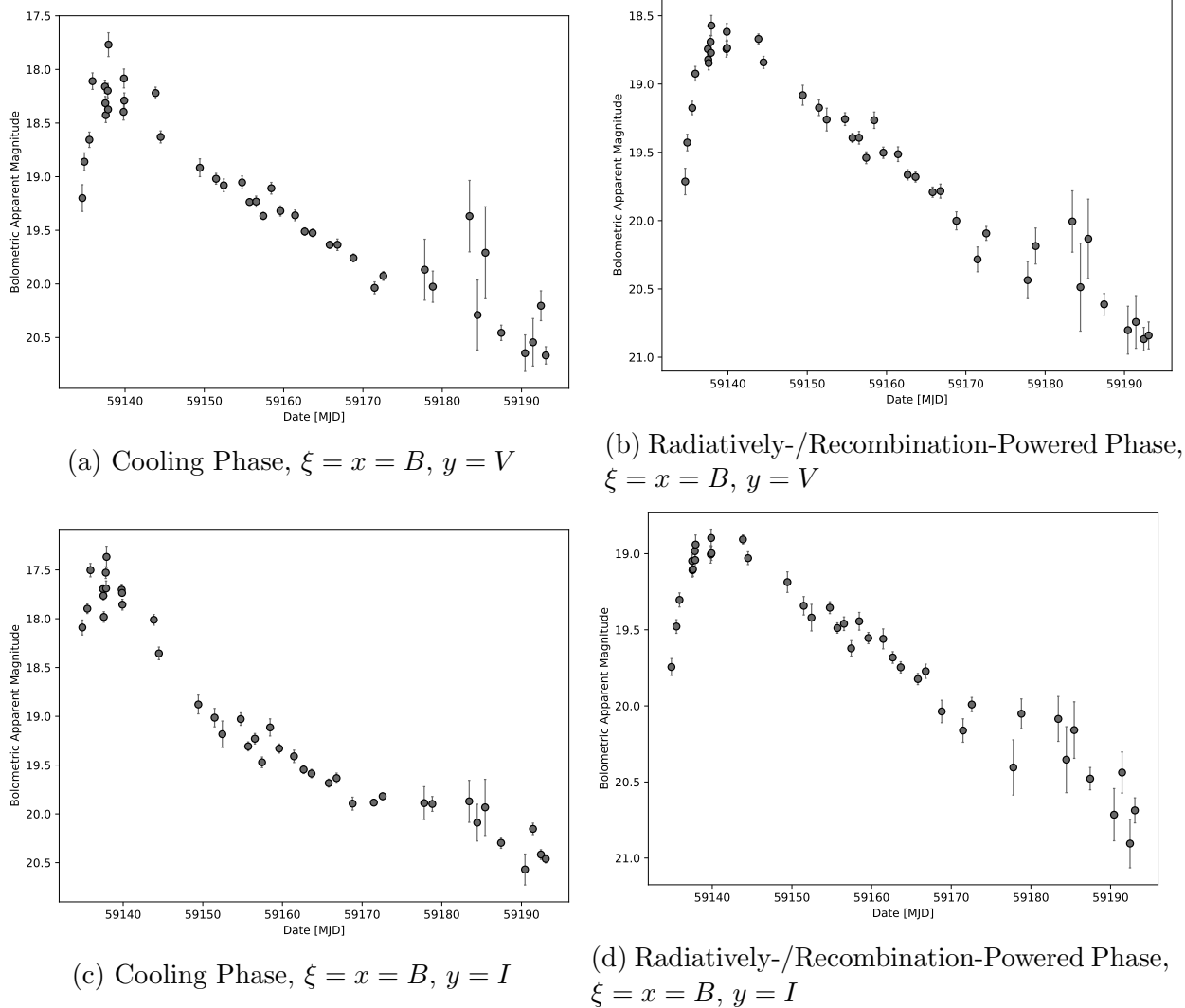


Figure 7.6: Comparison of results using bolometric coefficient coefficients in [Lyman et al. \(2013\)](#)

### 7.5.3 Comparison and Selection of Results

As seen in the figures above, there are differences between using the method in [Martinez et al. \(2021\)](#) and the method in [Lyman et al. \(2013\)](#). Let us compare and select here which ones to use for the actual bolometric light curve of KSP-ZN7090. For the [Martinez et al. \(2021\)](#) bolometric correction in Figure 7.3, we see a bolometric light curve which is not representative of a typical Type II SN bolometric light curve. The early data points are too bright, and this is due to the colour range and shape of the bolometric correction polynomial. We see that all colour values ( $m_B - m_V \lesssim 0.1$ ) are extrapolated in the polynomial in

Figure 7.3b. The polynomial in Figure 7.3b changes very dramatically outside of the colour range, dropping to a value of  $BC_V \sim -5$  for the smallest  $m_B - m_V$  value, and this is not reasonable. This results in values of bolometric correction with a larger absolute value and larger uncertainties. This extrapolation is questionable, and the resulting bolometric light curve is inconsistent with Type II SNe.

In contrast, the polynomial from the cooling phase of Lyman et al. (2013) in Figure 7.4b changes less dramatically outside the colour range compared to Figure 7.3b. The resulting bolometric light curve is more representative of Type II SNe. One of the reasons why the Martinez et al. (2021) bolometric correction polynomial is more dramatic is because Martinez et al. (2021) had colour corrections oriented more for Type II-P SNe. Recall that they had a set of bolometric correction coefficients for a plateau phase. Martinez et al. (2021) may be more suitable for Type II-P SNe, which may not have the range of colour difference values as in KSP-ZN7090, which is a Type II-L SNe. Hence, if we were to assume that the rise of KSP-ZN7090's light curve is powered by shock cooling emission, it is more reasonable to use the cooling phase coefficients in Lyman et al. (2013) rather than in Martinez et al. (2021).

In the bolometric corrections using the method of Lyman et al. (2013), there are several options for  $y$ . Looking at Figure 7.6, the results appear mostly comparable. However,  $y = V$  will be used instead of  $y = I$ , in order to have the earliest data, which is the most valuable. Recall from Section 3.9 that the first data points of KSP-ZN7090 was in the  $B$  and  $V$  bands, and that the first  $I$  band data point occurred several hours later. Hence the results with  $y = V$ , in Figures 7.6a and 7.6b, will be used.

The question now is whether or not we should use the cooling phase in Lyman et al. (2013) or the radiatively-/recombination-powered phase in Lyman et al. (2013). Again, this would depend on whether or not KSP-ZN7090's rise is powered by shock cooling emission or radioactive decay respectively. This will be investigated in Chapters 8 and 9. Finally, one thing to point out here is that the bolometric light curves in Figures 7.6a and 7.6b look much more reasonable than the light curve in Figure 6.6 from blackbody fitting. This method of bolometric corrections works much better for observations in a limited number of bands, as is the case for KSP-ZN7090.

## 7.6 Bolometric Apparent Magnitude to Bolometric Absolute Magnitude and Bolometric Luminosity

The final step is to convert the light curves in the previous section from bolometric apparent magnitude to bolometric absolute magnitude. Then a light curve of bolometric luminosity can be obtained, which is what will be used to fit light curve models to in Chapters 8 and 9.

### 7.6.1 Bolometric Apparent Magnitude to Bolometric Absolute Magnitude

The absolute magnitude  $M$  of an object is its apparent magnitude if the object was to be located at a distance of 10 pc [Carroll & Ostlie \(2017\)](#). To convert from apparent magnitude  $m$  to absolute magnitude  $M$ , we can use the equation:

$$M = m - 5 \log_{10} \left( \frac{D_L}{10 \text{ pc}} \right) \quad (7.3)$$

where  $D_L$  is the luminosity distance of the object, which for KSP-ZN7090 was found in Section 6.7 assuming a redshift of  $z = 0.1$ . This equation can be derived from the definitions in Section 6.2 and the relationship between flux, luminosity, and distance. The uncertainty in the absolute magnitude is the same as the uncertainty in the apparent magnitude. The light curve from Figure 7.6b, in bolometric absolute magnitudes, is shown in Figure 7.7.

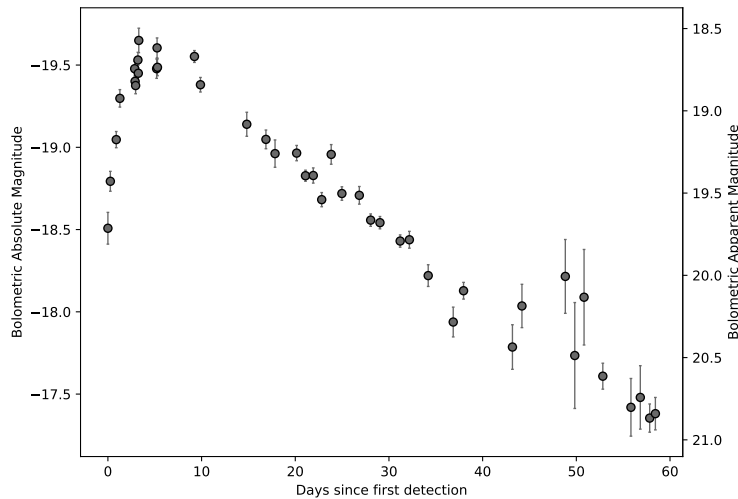


Figure 7.7: Light curve with bolometric absolute magnitudes, based on Figure 7.6b

## 7.6.2 Bolometric Absolute Magnitude to Bolometric Luminosity

The bolometric absolute magnitude  $M_{\text{bol}}$  and bolometric luminosity  $L_{\text{bol}}$  have the relationship:

$$M_{\text{bol}} = -2.5 \log_{10} \left( \frac{L_{\text{bol}}}{L_0} \right) \quad (7.4)$$

where  $L_0 = 3.0128 \times 10^{28}$  W, according to the IAU 2015 Resolution B2 (Mamajek et al. 2015). Rearranging this, we obtain:

$$L_{\text{bol}} = (10^{-M_{\text{bol}}/2.5})(L_0) \quad (7.5)$$

The uncertainty in  $L_{\text{bol}}$  is:

$$\begin{aligned} \delta L_{\text{bol}} &= \sqrt{\left( \frac{\partial L_{\text{bol}}}{\partial M_{\text{bol}}} \right)^2 (\delta M_{\text{bol}})^2} \\ &= \left( -\frac{\ln 10}{2.5} \right) (10^{-M_{\text{bol}}/2.5})(L_0)(\delta M_{\text{bol}}) \\ &= \left( -\frac{\ln 10}{2.5} \right) (L_{\text{bol}})(\delta M_{\text{bol}}) \end{aligned} \quad (7.6)$$

where  $\delta M_{\text{bol}}$  is the uncertainty in  $M_{\text{bol}}$ , which is the same as the uncertainty in  $m_{\text{bol}}$ . The light curve from Figure 7.6b, in bolometric luminosity values, is shown in Figure 7.8. We can now proceed with fitting models to the bolometric light curve.

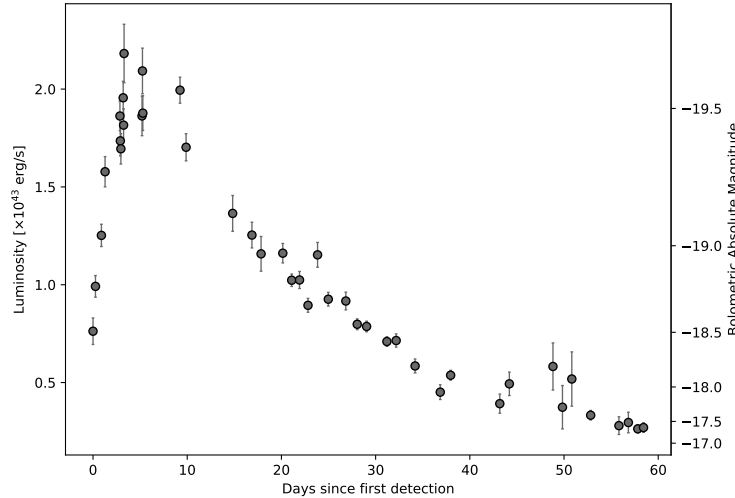


Figure 7.8: Light curve with bolometric luminosity, based on Figure 7.6b

# Part IV

## Light Curve Modelling

# Chapter 8

## Radioactive Decay Powered Rise

### 8.1 Overview

This chapter will investigate the possibility of KSP-ZN7090 having a light curve rise powered by the radioactive decay of Nickel-56, which corresponds to the scenario in Section 7.3.2.2. An analytic model from Valenti et al. (2007) for radioactive decay powered SN light curve rise will be used. The bolometric light curve in Figure 7.8, with bolometric corrections from the radiatively-/recombination-powered phase of Lyman et al. (2013), will be fitted.

### 8.2 Valenti et al. (2007) Model

Appendix A of Valenti et al. (2007) presents a model used to fit the light curves of SNe with rise powered by radioactive decay. This model was used by the authors for the Type Ic SN 2003jd, and was modified from an analytic model from Arnett (1982), originally for Type Ia SNe. This model does not have a hydrogen recombination phase, and hence may be applicable to KSP-ZN7090. The model, which is for the first 30 days after the explosion (in what is called the photospheric phase), gives an analytic expression for the bolometric luminosity  $L(t)$  as a function of time  $t$  (in seconds) after the explosion:

$$L(t) = M_{\text{Ni}} \exp \left( \left[ -\frac{t}{\tau_m} \right]^2 \right) \times \left[ (\epsilon_{\text{Ni}} - \epsilon_{\text{Co}}) \int_0^{t/\tau_m} A(\xi) d\xi + \epsilon_{\text{Co}} \int_0^{t/\tau_m} B(\xi) d\xi \right] \quad (8.1)$$

where:

$$A(\xi) \equiv 2\xi \exp(-2\xi y + \xi^2) \quad (8.2)$$

$$B(\xi) \equiv 2\xi \exp(-2\xi y + 2\xi s + \xi^2) \quad (8.3)$$

$$y \equiv \frac{\tau_m}{2\tau_{\text{Ni}}} \quad (8.4)$$

$$s \equiv \frac{\tau_m(\tau_{\text{Co}} - \tau_{\text{Ni}})}{2\tau_{\text{Co}}\tau_{\text{Ni}}} \quad (8.5)$$

$\epsilon_{\text{Ni}}$  and  $\epsilon_{\text{Co}}$  are the energies produced in 1 s by 1 g of  $^{56}\text{Ni}$  and  $^{56}\text{Co}$  respectively. They have values of  $\epsilon_{\text{Ni}} = 3.90 \times 10^{10} \text{ erg} \cdot \text{s}^{-1} \cdot \text{g}^{-1}$  and  $\epsilon_{\text{Co}} = 6.78 \times 10^9 \text{ erg} \cdot \text{s}^{-1} \cdot \text{g}^{-1}$ .  $\tau_{\text{Ni}}$  and  $\tau_{\text{Co}}$  are the decay times of  $^{56}\text{Ni}$  and  $^{56}\text{Co}$  respectively, which are their half-life values divided by  $\ln 2$ . They have values of  $\tau_{\text{Ni}} = 6.1 / \ln 2 = 8.8 \text{ d} = 760358 \text{ s}$ , and  $\tau_{\text{Co}} = 77.27 / \ln 2 = 111.477 \text{ d} = 9631617 \text{ s}$ .  $M_{\text{Ni}}$  is the Nickel-56 mass.  $\tau_m$  is some timescale of the light curve, which is given by:

$$\tau_m = \left( \frac{\kappa_{\text{opt}}}{\beta c} \right)^{1/2} \left( \frac{10M_{\text{ej}}^3}{3E_{\text{k}}} \right)^{1/4} \quad (8.6)$$

where  $M_{\text{ej}}$  is the ejecta mass,  $E_{\text{k}}$  is the ejecta kinetic energy,  $\beta \approx 13.8$  is a constant, and  $\kappa_{\text{opt}}$  is the optical opacity, which is assumed to be constant in this model.  $\tau_m$  is also called the effective diffusion time and describes the width of the bolometric light curve (Cano 2013). The relationship between  $M_{\text{ej}}$  and  $E_{\text{k}}$  is given by Toy et al. (2016):

$$E_{\text{k}} = \frac{3}{10} M_{\text{ej}} v_{\text{ph}}^2 \quad (8.7)$$

where  $v_{\text{ph}}$  is the photospheric velocity. Note that both Arnett (1982) and Valenti et al. (2007) have incorrect versions of this equation, and Toy et al. (2016) gives the correct version.

### 8.2.2 Method to Fit the Model

In this model, the parameters which we want to find are the physical parameters:  $M_{\text{Ni}}$ ,  $M_{\text{ej}}$ , and  $E_{\text{k}}$ . There is degeneracy between  $M_{\text{ej}}$  and  $E_{\text{k}}$ , which is broken by Equation (8.7), provided that we know what  $v_{\text{ph}}$  is. Hence, in this model, there are two fit parameters:  $M_{\text{Ni}}$  and  $\tau_m$ . After fitting the model and obtaining the fitted values of  $M_{\text{Ni}}$  and  $\tau_m$ ,  $M_{\text{ej}}$  and  $E_{\text{k}}$  can be found from  $\tau_m$  and  $v_{\text{ph}}$ .

Suppose that we know the photospheric velocity  $v_{\text{ph}}$ , and that we have fitted the model to the light curve, finding  $M_{\text{Ni}}$  and  $\tau_m$ , and their associated uncertainties  $\delta M_{\text{Ni}}$  and  $\delta \tau_m$ .

Then rearranging Equation (8.6) and substituting in Equation (8.7), we can find  $M_{\text{ej}}$ :

$$M_{\text{ej}} = \tau_m^2 \left( \frac{3\beta c}{10\kappa_{\text{opt}}} v_{\text{ph}} \right) \quad (8.8)$$

Then the uncertainty in  $M_{\text{ej}}$  is:

$$\delta M_{\text{ej}} = \sqrt{\left( \frac{\partial M_{\text{ej}}}{\partial \tau_m} \right)^2 (\delta \tau_m)^2} = 2 \left( \frac{M_{\text{ej}}}{\tau_m} \right) (\delta \tau_m) \quad (8.9)$$

With  $M_{\text{ej}}$  and  $v_{\text{ph}}$ ,  $E_{\text{k}}$  can be found with Equation (8.7). The uncertainty in  $E_{\text{k}}$  is:

$$\delta E_{\text{k}} = \sqrt{\left( \frac{\partial E_{\text{k}}}{\partial \tau_m} \right)^2 (\delta \tau_m)^2} = 2 \left( \frac{E_{\text{k}}}{\tau_m} \right) (\delta \tau_m) \quad (8.10)$$

## 8.3 Fitting the Valenti et al. (2007) to KSP-ZN7090's Bolometric Light Curve

Now, let us fit this model to the bolometric light curve of KSP-ZN7090 in Figure 7.8. Firstly, some assumptions need to be made. The photospheric velocity  $v_{\text{ph}}$  is obtained through analysis of KSP-ZN7090's spectrum in the early phases, by measuring the shifts of certain emission lines. However, since KSP-ZN7090's spectra have not been analyzed yet at the time of this work, let us assume a value of  $v_{\text{ph}} \sim 10000$  km/s. This  $v_{\text{ph}}$  value is around the same order of magnitude of typical Type II SN photospheric velocity, but a bit on the higher end. For example, see the Type II-L SN 2013ej in Bose et al. (2015b), and also the Type II SN 2016gsd which had estimated velocities as high as 20000 km/s (Reynolds et al. 2020). In addition, let us assume Thompson scattering in the envelope with hydrogen mass fraction  $X = 0.7$ , so that the opacity is  $\kappa_{\text{opt}} = 0.2(1 + X) = 0.34$  cm<sup>2</sup>/g.

### 8.3.1 Fitting with Fixed Explosion Time

Firstly, a fit was done with a fixed explosion time, assuming that the explosion happened at  $|t_0| = 0.191$  days before first detection, which was the value obtained in Section 5.3 by power law fitting. The result is shown in Figure 8.1, for the first 10 days after first detection. As we can see, the fit is poor in quality and fails to capture the light curve rise. This is because the  $\tau_m$  parameter, which helps to determine when the peak of the light curve will occur and how wide the bolometric light curve is, is forced to a very small value due to the fast rise of KSP-ZN7090's light curve. The convexity of the earliest part of the model cannot

replicate KSP-ZN7090's rising light curve. This suggests that either the  $t_0$  value found in Section 5.3 is not entirely correct or that KSP-ZN7090's early light curve does not follow the mechanisms proposed in the Valenti et al. (2007) model. Here, let us assume the former, and add the explosion time as a fit parameter.

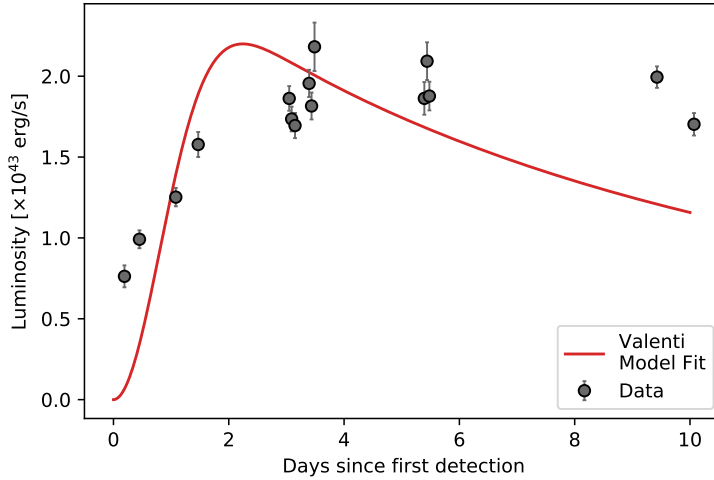


Figure 8.1: Fit of Valenti et al. (2007) model, with explosion time fixed at 0.191 days before first detection (see Section 5.3), to the first 10 days after first detection of KSP-ZN7090's bolometric light curve (Figure 7.8). The resulting fitted parameters are  $M_{\text{Ni}} = (0.350 \pm 0.031)M_{\odot}$  and  $\tau_m = 1.206 \pm 0.214$  days.  $\chi^2/\text{dof} = 39.361$ .

### 8.3.2 Fitting with Explosion Time as Another Fit Parameter

Figure 8.2 shows the result of fitting the Valenti et al. (2007) model, with the explosion time as a fit parameter, to the first 4 days after first detection. The model here captures the light curve rise better. However, the fitted explosion time value is  $t_{\text{exp}} = 2.049 \pm 0.521$  days before the first detection, which is significantly earlier than the  $t_0$  value from Section 5.3.

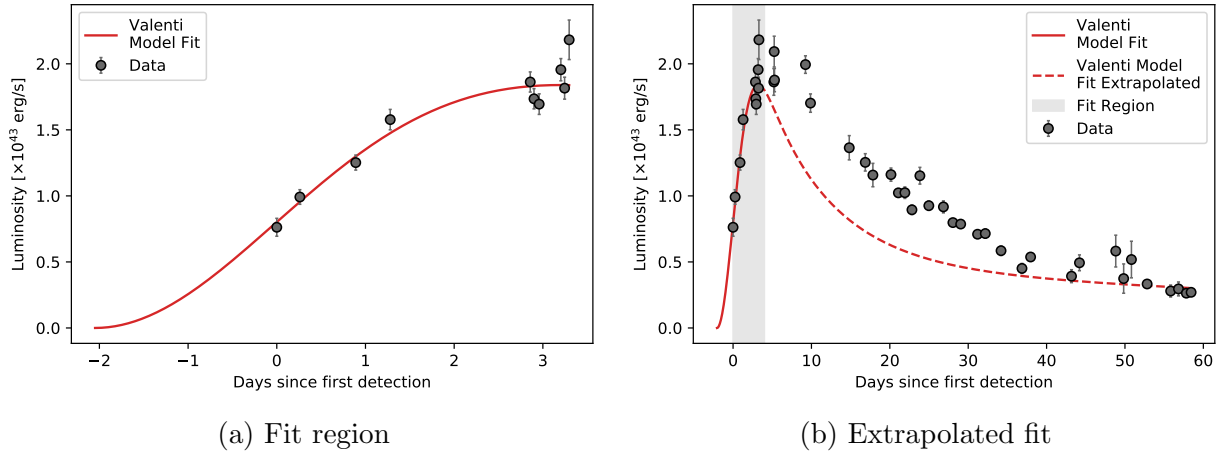


Figure 8.2: Fit of [Valenti et al. \(2007\)](#) model, with explosion time as a fit parameter, to the first 4 days after first detection.  $\chi^2/\text{dof} = 1.721$ .

Variable	Result
Nickel-56 mass $M_{\text{Ni}}$ [ $\times M_{\odot}$ ]	$0.382 \pm 0.041$
Light curve timescale $\tau_m$ [days]	$3.368 \pm 0.854$
Explosion time $t_{\text{exp}}$ [days before first detection]	$2.049 \pm 0.521$
Ejecta mass $M_{\text{ej}}$ [ $\times M_{\odot}$ ]	$0.016 \pm 0.008$
Ejecta kinetic energy $E_k$ [ $\times 10^{51}$ erg]	$0.009 \pm 0.005$

Table 8.1: Results of fitting the [Valenti et al. \(2007\)](#) model to the bolometric light curve of KSP-ZN7090, in the first 4 days after first detection. The first 3 rows are the fitted parameters, and the results in the last 2 rows are calculated from the results in the first 2 rows. See Figure 8.2 for the fit.

Fits were also conducted for longer intervals, for the first 6, 10, and 25 days after first detection. These fits are shown in Figure 8.3. These results will be discussed in Section 8.4.

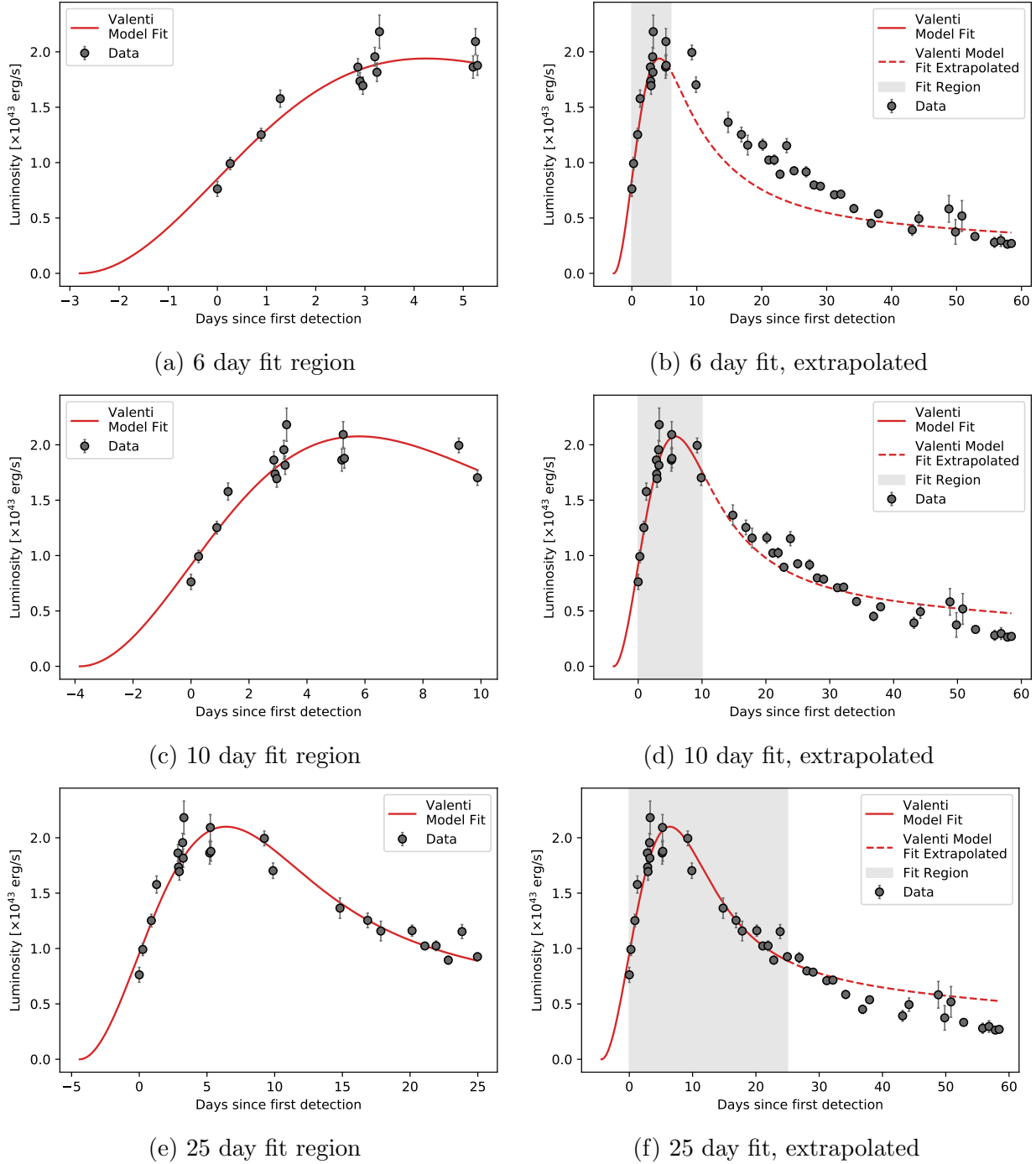


Figure 8.3: Fits of Valenti et al. (2007) model, with explosion time as a fit parameter, for the first 6, 10, and 25 days after first detection. The  $\chi^2/\text{dof}$  values for the fits are 1.772, 2.772, and 2.957 respectively.

## 8.4 Discussion on the Results from the Valenti et al. (2007) Model Fits

### 8.4.1 Model Validity and Fit Region

In the fits in Section 8.3.2, we can see that the light curve is modelled relatively well in comparison to the fit in Section 8.3.1 where the explosion time was fixed. However, in Figures 8.2 and 8.3, we see that when the model is extrapolated beyond the fit region, the light curve is represented poorly. This is because the Valenti et al. (2007) model presented here only applies for what is called the photospheric phase of the light curve. During this phase, a photon diffusion approximation is assumed (Cano 2013). The ejecta is assumed to be optically thick. But after the peak, this is not the case. As the ejecta expands, soon there is no more photosphere, and the ejecta is no longer thick (Valenti et al. 2007), causing the approximation to fail. The fitted post-peak light curves using the Valenti et al. (2007) model would deviate from the actual light curve, for example as seen in Figure 5 of Lyman et al. (2016). In other words, the model fails post-peak.

Indeed, we see that as the size of the fit region is increased, the  $\chi^2/\text{dof}$  for the fit gets larger, as seen in Figure 8.3. The Valenti et al. (2007) does not work well post-peak. Hence, let us only use the results of in Figure 8.2, fit to the first 4 days after first detection. The fit region here, of up to 4 days after the first detection, is before the peak epochs found in Section 5.2 for all of the  $B$ ,  $V$ , and  $I$  bands.

### 8.4.2 Comparing the Results to Other Type II-L SNe

Let us compare the physical parameters obtained from fitting the Valenti et al. (2007) model (to the first 4 days after the first detection) with the physical parameters of other Type II-L SNe. The results are presented in Table 8.2. We can see that the values from the Valenti et al. (2007) model fit are inconsistent with other Type II-L SNe. The fitted Nickel-56 mass is too large by an order of magnitude, and the ejecta mass and ejecta energy are too small. In particular, the fitted Nickel-56 mass being much larger suggests that there is extra energy which is contributing to the light curve's rise, which is not being accounted for in this model. This energy is likely due to shock cooling emission.

Supernova	Type	$M_{\text{Ni}} [\times M_{\odot}]$	$M_{\text{ej}} [\times M_{\odot}]$	$E_k [\times 10^{51} \text{ erg}]$
KSP-ZN7090 <a href="#">Valenti et al. (2007)</a> fit	II-L	$0.382 \pm 0.041$	$0.016 \pm 0.008$	$0.009 \pm 0.005$
SN 2013ej ( <a href="#">Bose et al. 2015b</a> )	II-L	$0.020 \pm 0.002$	12	$2.3^{\dagger}$
SN 2013hj ( <a href="#">Bose et al. 2015a</a> )	II-L	$0.08 \pm 0.01$	9.6	$2^{\dagger}$
SN 2014G ( <a href="#">Terreran et al. 2016</a> )	II-L	$0.059 \pm 0.003$	4.8	2.0
SN 2017ahn ( <a href="#">Tartaglia et al. 2021</a> )	II	$0.041 \pm 0.006$	12.52	1.35

Table 8.2: Comparison between some physical parameters of Type II-L SNe and the fitted physical parameters from the [Valenti et al. \(2007\)](#) model (first row). The values with a dagger ( $\dagger$ ) are total energy values (kinetic + thermal), rather than just kinetic energy.

At this point, we can conclude that the [Valenti et al. \(2007\)](#) model is incompatible with KSP-ZN7090. However, this does not rule out entirely that the rise of KSP-ZN7090's light curve is being powered primarily by radioactive decay. This is because the [Valenti et al. \(2007\)](#) model has a lot of assumptions. For example, this model assumes a centrally concentrated nickel distribution and a small initial (progenitor) radius, which is not always true ([Lyman et al. 2016](#)). In order to extend the conclusion to say that KSP-ZN7090's light curve rise is likely not being powered primarily by radioactive decay, we can compare the rise times of KSP-ZN7090 with those of SNe with rise powered by radioactive decay. This will be done in the next section.

## 8.5 Rise Time Comparison of SNe with Radioactive Decay Powered Rise

Let us now compare the rise times of SNe with a radioactive decay powered rise with the rise times of KSP-ZN7090 found in Chapter 5. Recall that the rise time of a SN light curve is the time from the explosion epoch to peak epoch ([Gonzalez-Gaitan et al. 2015](#)). First, let us consider Type Ia SNe. The majority of Type Ia SN early optical light curves are powered by the radioactive decay of Nickel-56 ([Firth et al. 2014](#)). [Firth et al. \(2014\)](#) found the rise times of 18 Type Ia SNe, giving a mean rise time of  $18.98 \pm 0.54$  days, with results ranging from 15.98 days to 24.7 days.

[Lyman et al. \(2016\)](#) investigated the rise times of 38 stripped envelope CCSNe by fitting their light curves to the [Valenti et al. \(2007\)](#) model. These SNe encompassed a variety of types, and had rises which were powered by radioactive decay of Nickel-56. They found average rise times of 17.6, 16.7, 16.8, and 13 days for Type IIb, Ib, Ic, and broad-lined Ic

SNe respectively.

Now, recall from Section 5.3.2 that the rise times for KSP-ZN7090’s *BVI* light curves were about  $5.801 \pm 0.225$ ,  $7.983 \pm 0.278$ , and  $11.147 \pm 0.369$  days for the *B*, *V*, and *I* bands respectively. From Firth et al. (2014) and Lyman et al. (2016), we can see that the rise times for SNe with light curve rise powered primarily by radioactive decay are in the range of  $\sim$ 15 to 20 days. This is inconsistent with the rise times of KSP-ZN7090. All of the discussion in this chapter suggests that the rise of KSP-ZN7090’s light curve is likely not powered primarily by radioactive decay. It is likely that KSP-ZN7090’s rise is powered by shock cooling emission, and this will be discussed in the next chapter.

# Chapter 9

## Shock Cooling Emission Powered Rise

### 9.1 Overview

This chapter will investigate the possibility of KSP-ZN7090 having a light curve rise powered by shock cooling emission, which corresponds to the scenario in Section 7.3.2.1. An analytic model from Sapir & Waxman (2017) will be used to fit the light curve of KSP-ZN7090.

### 9.2 Sapir & Waxman (2017) Model

#### 9.2.1 Bolometric Luminosity

Sapir & Waxman (2017) provides an analytic model to fit the light curves of SNe with rise powered by shock cooling emission. This model is based on the popular Rabinak & Waxman (2011) model, and adds a suppression factor so that the analytic description is still valid at later times in the light curve. Here, let us consider the version of the model for SNe with efficiently convective envelopes, which are typical for red supergiant (RSG) progenitors, with a polytropic index of  $n = 3/2$ . We will make some assumptions to fit the model with KSP-ZN7090's light curve. The bolometric luminosity  $L_{\text{RW}}(t)$  of the SN (with RSG progenitor) is given by Rabinak & Waxman (2011) (in Sapir & Waxman (2017)) as:

$$L_{\text{RW}}(t) = 2.0 \times 10^{42} \left( \frac{(v_{s*,8.5}) t^2}{f_\rho \kappa_{0.34} M_{\text{ej}} / M_\odot} \right)^{-\epsilon_2} \frac{(v_{s*,8.5})^2 R_{13}}{\kappa_{0.34}} \quad (9.1)$$

$L_{\text{RW}}(t)$  here is in units of erg/s, and  $t$  is the time in days after the explosion.  $M_{\text{ej}}$  is the ejecta mass,  $R_{13}$  is the radius of the progenitor in units of  $10^{13}$  cm ( $R_* = 10^{13} R_{13}$  cm),  $\kappa_{0.34}$  is the opacity in units of  $0.34 \text{ cm}^2/\text{g}$  ( $\kappa = 0.34 \kappa_{0.34} \text{ cm}^2/\text{g}$ ), and  $\epsilon_2 = 0.086$ .  $v_{s*,8.5}$  is a scaled

version of a velocity quantity called  $v_{s*}$ , which is related to the velocity of the shock. The scaling is  $v_{s*} = (10^{8.5})(v_{s*,8.5})$  cm/s. Matzner & McKee (1999) gives an approximation for  $v_{s*}$  as:

$$v_{s*} \approx \frac{1.05}{f_\rho^\beta} \sqrt{\frac{E_{\text{ej}}}{M_{\text{ej}}}} \quad (9.2)$$

where  $E_{\text{ej}}$  is the ejecta energy and  $\beta = 0.191$  for a polytropic index of  $n = 3/2$ .  $f_\rho$  is a quantity that depends on some properties of the progenitor, and is given by Rabinak & Waxman (2011) as:

$$f_\rho = \left( \frac{3}{4\pi} \right) \left( \frac{\rho_1}{\rho_*} \right) \quad (9.3)$$

where  $\rho_1/\rho_*$  is a parameter that describes the the density structure of the progenitor star's outermost regions (Calzavara & Matzner 2004).  $f_\rho$  is dependent on several physical parameters, but Rabinak & Waxman (2011) indicated that the results of their model are not very sensitive to  $f_\rho$ . Hence, let us assume a fixed value for  $f_\rho$ . Calzavara & Matzner (2004) gives a nominal value of  $\rho_1/\rho_* = 0.5$  for RSGs, and so let us assume  $f_\rho = 3/(4\pi) \times 0.5 = 3/(8\pi)$ .

Sapir & Waxman (2017) updates the Rabinak & Waxman (2011) model by adding a suppression factor for the bolometric luminosity, so that the bolometric luminosity is:

$$L(t) = L_{\text{RW}}(t) \times A \exp \left[ - \left( \frac{at}{t_{\text{tr}}} \right)^\alpha \right] \quad (9.4)$$

where  $A = 0.94$ ,  $a = 0.8$ , and  $\alpha = 1.67$  for a polytropic index of  $n = 3/2$ . Here,  $L_{\text{RW}}(t)$  is Equation (9.1).  $t_{\text{tr}}$  is some timescale describing when the envelope becomes transparent, and is given (in units of days) by:

$$t_{\text{tr}} = 19.5 \left( \frac{\kappa_{0.34} M_{\text{env}} / M_\odot}{v_{s*,8.5}} \right)^{1/2} \quad (9.5)$$

where  $M_{\text{env}}$  is the mass of the envelope. This is defined as  $M_{\text{env}} \equiv M - M_c$ , where  $M_c$  is the core mass. Let us assume that the core mass is the Chandrasekhar mass, which is around  $\sim 1.4M_\odot$  (Mazzali et al. 2007).

## 9.2.2 Temperature and Blackbody

In order to use the model, we also need the photospheric temperature of the SN, which (in units of eV) is given by Rabinak & Waxman (2011) (in Sapir & Waxman (2017)) as:

$$T_{\text{ph,RW}}(t) = 1.61 \left( \frac{(v_{s*,8.5})^2 t^2}{f_\rho \kappa_{0.34} M_{\text{ej}} / M_\odot} \right)^{\epsilon_1} \left( \frac{R_{13}}{\kappa_{0.34}} \right)^{1/4} t^{-1/2} \quad (9.6)$$

where  $\epsilon_1 = 0.027$  for a polytropic index of  $n = 3/2$ . Here,  $t$  is also in units of days.

Now, notice from Equations (9.1) and (9.4) that the bolometric luminosity  $L(t)$  is a strictly decreasing function. The photospheric temperature  $T_{\text{ph,RW}}(t)$  in Equation (9.6) is also a strictly decreasing function. Intuitively, this makes sense for shock cooling emission; since the heated material is cooling, the bolometric luminosity and temperature would always strictly decrease. However, we saw in the *BVI* light curves of KSP-ZN7090 that this was not the case. The luminosity rises in the early part of the light curve before decreasing. One may ask whether or not there is a contradiction here.

As a matter of fact, there is no contradiction here. The key is the assumed spectral energy distribution (SED) of the SN. We need to consider individual bands. If we assume a blackbody spectrum for the SN, then the luminosity in a single band is equal to the bolometric luminosity times the blackbody integrated between the bandpass of that band (note that the limits of integration are fixed). But since the photospheric temperature of the SN changes with time, the blackbody will shift right with time (the peak will be at longer wavelengths). The result of this is that the light curve of a single band rises and then falls. This is the light curve shape which is given by Equation (9.7) below. The spectral luminosity per unit wavelength (CGS units of erg/s/cm) is (Sapir & Waxman 2017):

$$L_\lambda(t) = L(t) \times \frac{k_B T_{\text{col}}(t)}{hc} \times g_{\text{BB}}(hc/(\lambda k_B T_{\text{col}}(t))) \quad (9.7)$$

where  $T_{\text{col}}(t)$  is called the colour temperature and describes the temperature of the plasma. For a polytropic index of  $n = 3/2$ , we can approximate  $T_{\text{col}}(t)$  as  $T_{\text{col}}(t) = 1.1 \times T_{\text{ph,RW}}(t)$  (Sapir & Waxman 2017). In Equation (9.7), the temperature values are in units of K.  $g_{\text{BB}}(x)$  is the normalized Planck function, given by:

$$g_{\text{BB}}(x) = \frac{15x^5}{\pi^4(\exp(x) - 1)} \quad (9.8)$$

Instead of integrating the bandpass, we could just use the effective wavelength of the band from Section 6.2.2, taking  $\lambda = \lambda_{\text{eff},x}$  in Equation (9.7) for band  $x$ . So suppose we want to get a model for the  $B$  band luminosity of KSP-ZN7090. Then this would equal to  $L_{\lambda_{\text{eff},B}}(t) \times \lambda_{\text{eff},B}$ , which is in the standard units of luminosity (CGS units of erg/s).

Now, one may also ask why the bolometric light curves obtained in Chapter 7 (assuming a cooling phase) are not strictly decreasing, since they are bolometric after all. The reason is that a different SED is being assumed during bolometric corrections. Each model for bolometric corrections corresponds to different SEDs for the SNe. In the Sapir & Waxman (2017) and Rabinak & Waxman (2011) models, a blackbody SED is assumed. These models are just theoretical, and in real life we would not see this for the bolometric light curves of SNe.

### 9.2.3 Method to Fit the Model to KSP-ZN7090's Light Curve

Usually, the Sapir & Waxman (2017) and Rabinak & Waxman (2011) models are used to find the SN progenitor's radius  $R_*$  once the other physical parameters such as ejecta mass  $M_{\text{ej}}$  and ejecta energy  $E_{\text{ej}}$  have been estimated from nebular phase fitting.  $M_{\text{ej}}$  and  $E_{\text{ej}}$  would have been obtained from models such as those in Section 2.8. However, since the light curves of KSP-ZN7090 at the time of this work do not contain the nebular phase yet (as discussed in Section 7.4.2), let us make some assumptions. As in Chapter 8, let us assume a photospheric velocity of  $v_{\text{ph}} = 10000$  km/s. Then rearranging Equation (8.7), we can obtain:

$$\sqrt{\frac{E_{\text{ej}}}{M_{\text{ej}}}} = v_{\text{ph}} \sqrt{\frac{3}{10}} \quad (9.9)$$

We can then substitute Equation (9.9) into Equation (9.2), and therefore have  $v_{s*,8.5}$  in Equation (9.1) as a constant. Then the only fit parameters in Equation (9.1) would be  $M_{\text{ej}}$  and  $R_{13}$ . The Sapir & Waxman (2017) model will be fitted to the light curve of KSP-ZN7090 with these assumptions.

## 9.3 Fitting the Sapir & Waxman (2017) Model to KSP-ZN7090's Light Curve

Now, let us attempt to fit the Sapir & Waxman (2017) model to KSP-ZN7090's  $B$  band light curve. The effective wavelength value which will be used for the  $B$  band is 436.1 nm,

from Table 6.1. Let us do a fit to only the first 10 days after the first detection, so that a similar comparison could be made to the Valenti et al. (2007) model results from Chapter 8.

### 9.3.1 Fitting with Fixed Explosion Time

#### 9.3.1.1 Results of Fit

Firstly, similar to Section 8.3.1, a fit was done with a fixed explosion time, assuming that the explosion happened at  $|t_0| = 0.191$  days before first detection. Recall that this value was from Section 5.3 by power law fitting. Upper limits of  $M_{\text{ej}} = 900M_\odot$  (note that this is unphysical) and  $R_* = 1500R_\odot$  were imposed in the fit. The result of fitting the first 10 days after first detection is shown in Figure 9.1. As we can see, this fit is poor in quality ( $\chi^2/\text{dof} = 20.054$ ) and fails to capture the light curve rise. The resulting fitted parameters are  $M_{\text{ej}} = (900 \pm 1345)M_\odot$  (at the limit of the upper bound value imposed in the fit) and  $R_* = (313.240 \pm 80.069)R_\odot$ . Using Equation (9.9), this results in an ejecta energy of  $E_{\text{ej}} \sim 537 \times 10^{51}$  erg. Clearly, these values are unphysical for Type II SNe. The ejecta mass and ejecta energy are both too large, and the uncertainties are huge. However, in contrast to the Valenti et al. (2007) model fit in Section 8.3.1, we can see that the concavity of the earliest part of the light curve in the Sapir & Waxman (2017) model fit is consistent with the light curve of KSP-ZN7090, which is a good sign. This could suggest that the mechanisms behind the Sapir & Waxman (2017) model are applicable to KSP-ZN7090, and that the  $t_0$  value found in Section 5.3 is not entirely correct.

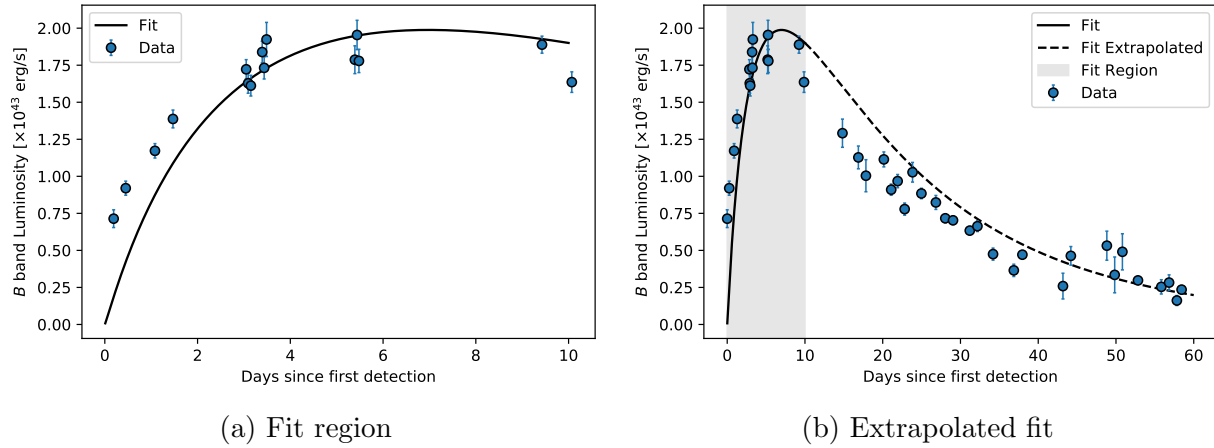


Figure 9.1: Fit of Sapir & Waxman (2017) model, with explosion time fixed at 0.191 days before first detection (see Section 5.3), to the first 10 days after first detection of KSP-ZN7090's  $B$  band light curve.  $\chi^2/\text{dof} = 20.054$ .

### 9.3.1.2 Contour Plots and Discussion

Figure 9.2 shows a contour plot of the reduced chi-squared ( $\chi^2/\text{dof}$ ) values for fits to the first 10 days after first detection of KSP-ZN7090's  $B$  band light curve, with the explosion time fixed at 0.191 days before first detection. The fitted value of ejecta mass is at the imposed upper limit of  $900M_\odot$  in the fit (which is not even physical). The contour plot in Figure 9.2a suggests that the optimal set of parameters in this case is even larger than this ejecta mass value, within the  $\chi^2/\text{dof} = 30$  contour. Looking at a region of the contour plot which would have more physical values (Figure 9.2b), we can see that values of  $\chi^2/\text{dof}$  as small as the minimum value of 20.054 (from Figure 9.1) are not obtained in this region. The smallest  $\chi^2/\text{dof}$  values are around 40. The minimum  $\chi^2/\text{dof}$  indeed occurs in a region with unphysical values.

Hence, we can conclude that the fit done here, fixing the explosion time at 0.191 days before first detection, does not produce physical results. It is possible that this is because the  $t_0$  value is not entirely correct. Recall that in Section 5.3, due to limited data, data above half the maximum flux was also used for the single power law fit, contrary to the method in Gonzalez-Gaitan et al. (2015). Hence, let us try adding the explosion time as a fit parameter.

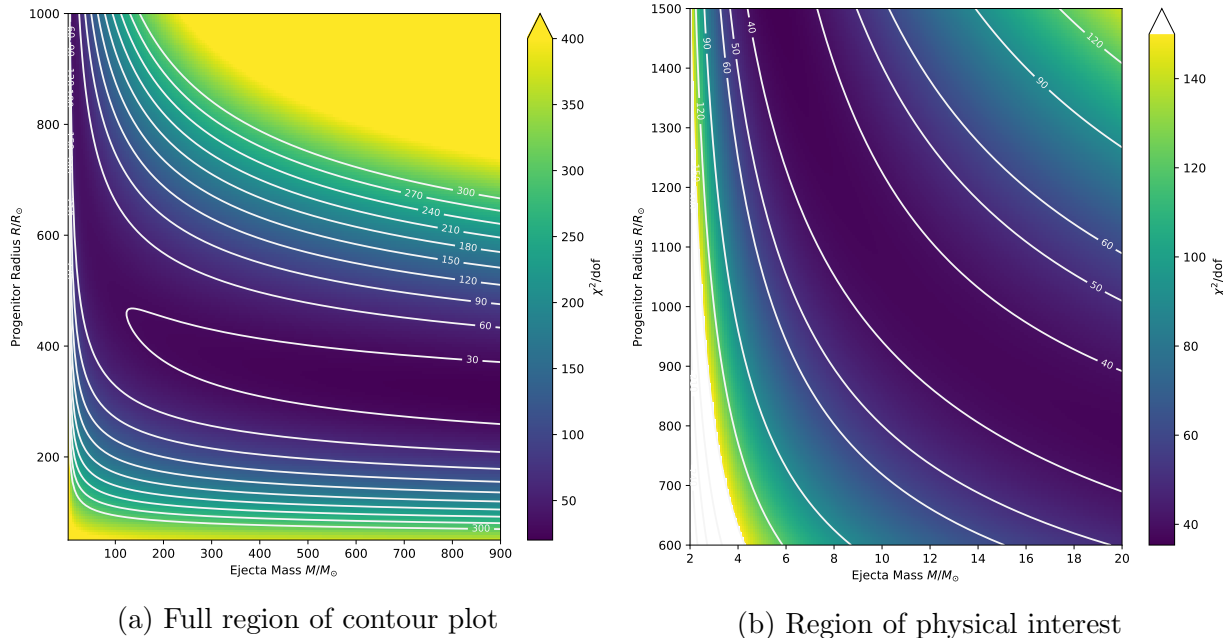


Figure 9.2: Contour plots of  $\chi^2/\text{dof}$  values when fitting the Sapir & Waxman (2017) model, with explosion time fixed at 0.191 days before first detection, to the first 10 days after first detection of KSP-ZN7090's  $B$  band light curve.

### 9.3.2 Fitting with Explosion Time as Another Fit Parameter

#### 9.3.2.1 Results of Fit

Figure 9.3 shows the result of fitting the Sapir & Waxman (2017) model to the first 10 days after first detection of KSP-ZN7090's  $B$  band light curve, with explosion time as a fit parameter. The resulting fitted parameters are  $M_{\text{ej}} = (741.485 \pm 529.969)M_{\odot}$ ,  $R_* = (302.170 \pm 32.683)R_{\odot}$ , and  $t_{\text{exp}} = 0.934 \pm 0.130$  days before first detection. The explosion time still suggests that KSP-ZN7090 was discovered  $\lesssim 1$  day after its explosion. Using Equation (9.9), this results in an ejecta energy of  $E_{\text{ej}} \sim 442 \times 10^{51}$  erg. The fitted parameters here are still unphysical, as the ejecta mass and ejecta energy are too large. Nevertheless, we see that the fit models the light curve well, with a  $\chi^2/\text{dof}$  value of 1.277. The rise of the light curve is better captured here than with the Valenti et al. (2007) model.

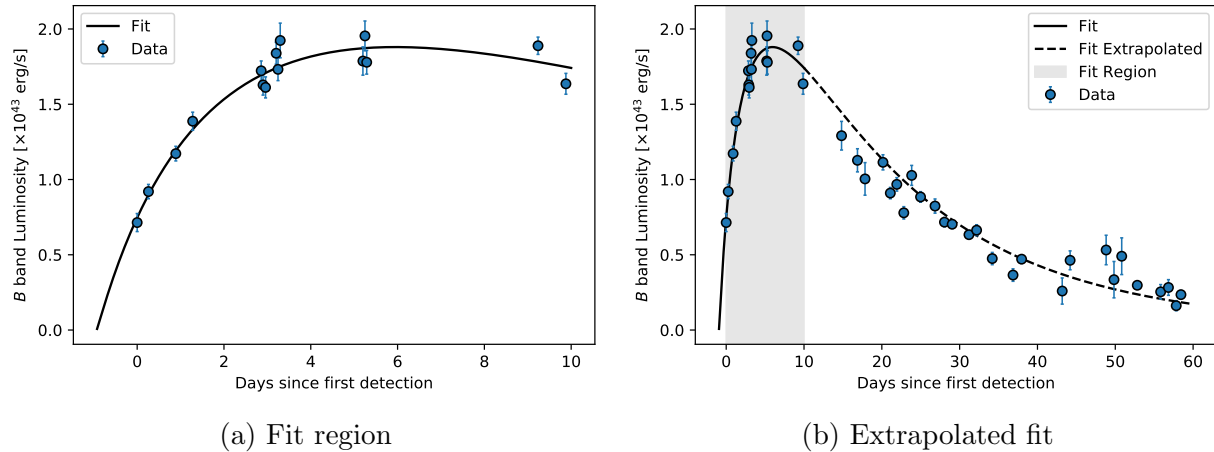


Figure 9.3: Fit of Sapir & Waxman (2017) model, with explosion time as a fit parameter, to the first 10 days after first detection of KSP-ZN7090's  $B$  band light curve. The fitted parameters are  $M_{\text{ej}} = (741.485 \pm 529.969)M_{\odot}$ ,  $R_* = (302.170 \pm 32.683)R_{\odot}$ , and  $t_{\text{exp}} = 0.934 \pm 0.130$  days before first detection. The resulting calculated ejecta energy is  $E_{\text{ej}} \sim 442 \times 10^{51}$  erg. The reduced chi-squared of the fit is  $\chi^2/\text{dof} = 1.277$ .

#### 9.3.2.2 Contour Plots and Discussion

However, upon investigating the contour plots of this fit, we notice some interesting results. There are actually many pairs of  $(M_{\text{ej}}, R_*)$  that could result in the same light curve model shape. As seen in the contour plots in Figure 9.4, there are multiple regions of minimum  $\chi^2/\text{dof}$ . One such region is where  $M_{\text{ej}}$  is relatively large and unphysical, shown in Figure 9.4b. The  $R_*$  values here do not change by too much. This region of the contour plot gives the fit shown in Figure 9.3.

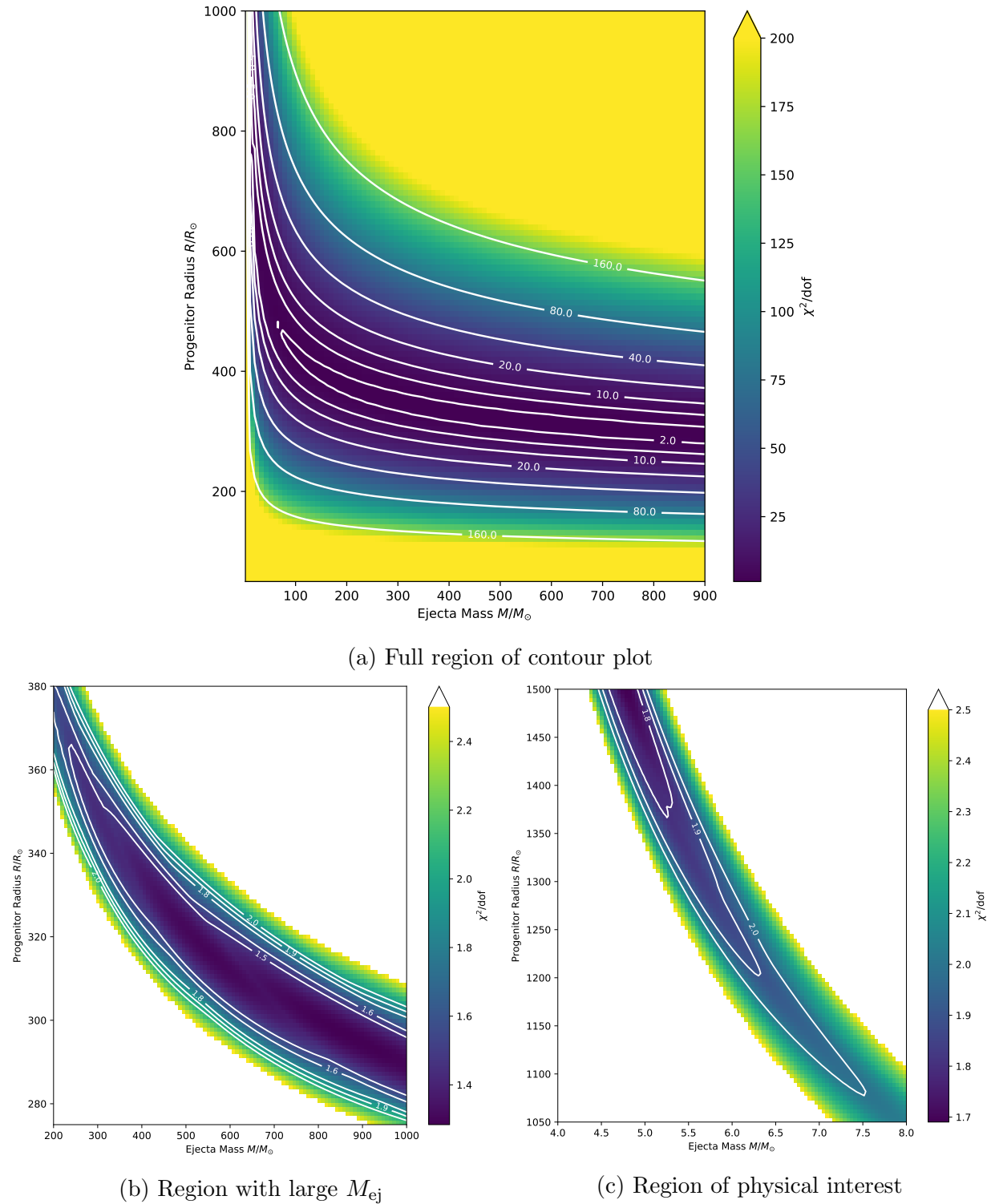


Figure 9.4: Contour plots of  $\chi^2/\text{dof}$  values when fitting the Sapir & Waxman (2017) model, with explosion time as a fit parameter, to the first 10 days after first detection of KSP-ZN7090's  $B$  band light curve.

Another region is shown in Figure 9.4c, which is the more physical regime of the contour plot. We see that the minimum  $\chi^2/\text{dof}$  can also be obtained here. This region is opposite of the region in Figure 9.4b, in that the  $M_{\text{ej}}$  values are small but the  $R_*$  values are large. The contour plot and fit was limited to  $R_* = 1500R_\odot$ , which is around the upper limit for RSGs (Levesque et al. 2005). We see that Figure 9.4 has “banana shaped”  $\chi^2/\text{dof}$  contours.

This shape of the contour plot in Figure 9.4 implies that there is degeneracy between  $M_{\text{ej}}$  and  $R_*$ . Many pairs of  $(M_{\text{ej}}, R_*)$  can create the same light curve shape. For example, Figure 9.5 shows the Sapir & Waxman (2017) model fitted to KSP-ZN7090’s  $B$  band light curve, with the progenitor radius set to the upper limit of  $R_* = 1500R_\odot$ . The resulting  $M_{\text{ej}}$  is now smaller at  $M_{\text{ej}} \sim 4.735M_\odot$ . This is a much more reasonable value for Type II-L SNe. Notice that the shape of the light curve here is similar to Figure 9.3 even though the parameters are very different and on opposite extremes. In addition, the high uncertainty in the parameters, in both Figures 9.3 and 9.5, suggests that there is degeneracy between the parameters. Hence, it is likely that if we do not know either  $M_{\text{ej}}$  or  $R_*$ , we cannot constrain the other. We need to know one of the two in order to have definite results.

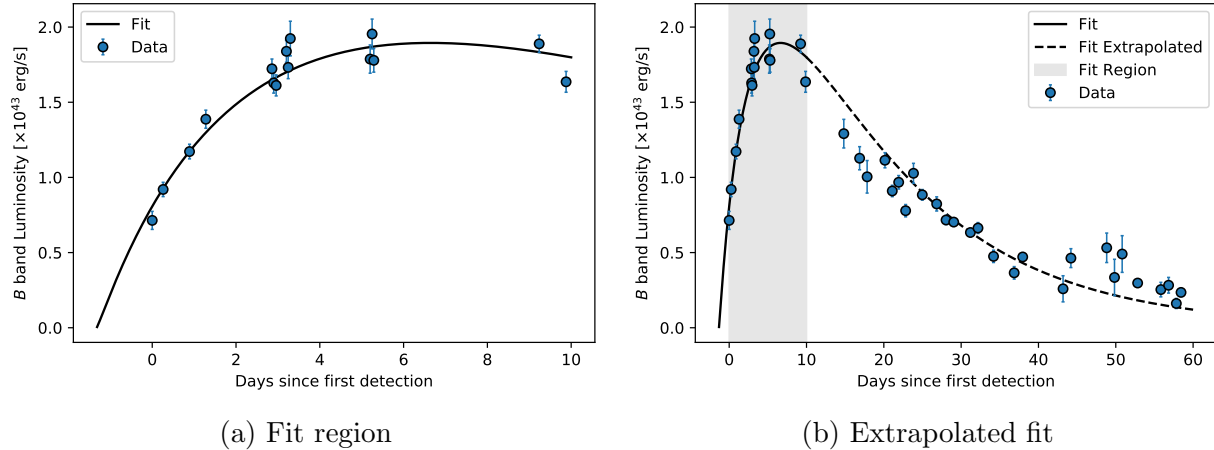


Figure 9.5: Fit of Sapir & Waxman (2017) model to the first 10 days after first detection of KSP-ZN7090’s  $B$  band light curve, with explosion time as a fit parameter and progenitor radius set to  $R_* = 1500R_\odot$ . The result is  $M_{\text{ej}} \sim 4.735M_\odot$  and  $t_{\text{exp}} \sim 1.327$  days before first detection. The uncertainties here again are high ( $\sim 50\%$ ). The resulting calculated ejecta energy is  $E_{\text{ej}} \sim 2.824 \times 10^{51}$  erg. Notice that the shape of the curve looks similar to that of Figure 9.3, because of the degeneracy between the  $M_{\text{ej}}$  and  $R_*$  parameters as seen in Figure 9.4. The reduced chi-squared here is  $\chi^2/\text{dof} = 1.676$ .

Notice that  $R_*$  changes greatly in the physical regime of the contour plot in Figure 9.5, with relatively small changes in  $M_{\text{ej}}$ . This situation makes sense, because  $L_{\text{RW}}(t)$  in Equation (9.4) is more heavily dependent on  $R_*$  than  $M_{\text{ej}}$  according to the exponents in the equation.

Physically, this also makes sense, because we should expect that the luminosity is heavily dependent on the envelope size. The area of shock breakout is approximately the surface area of the progenitor. Hence, if the progenitor has a larger radius, and hence a larger surface area, then the luminosity of the SN will be greater. The contour plots show that the luminosity is strongly dependent on the size of the progenitor. Overall, we see that the Sapir & Waxman (2017) model is more compatible with KSP-ZN7090 than the Valenti et al. (2007) model. If a reasonable value of  $M_{\text{ej}}$  is given to the Sapir & Waxman (2017) model, then the value of  $R_*$  will also likely be reasonable. We see that  $M_{\text{ej}}$  and  $R_*$  have roughly an inverse relationship.

## 9.4 Rise Time Comparison of SNe with Shock Cooling Emission Powered Rise

Let us now compare the rise times of SNe with a shock cooling emission powered rise with the rise times of KSP-ZN7090 found in Chapter 5. Rubin et al. (2016) investigated 57 Type II SNe which were powered by shock cooling emission, using the model of Rabinak & Waxman (2011). They found the rise times of these 57 Type II SNe, and reported these results in Table 3 of their paper. Taking values from this table, the mean rise time was found to be 7.739 days after the explosion with a standard deviation of 2.934 days. This mean value is consistent with the rise times of KSP-ZN7090 found in Section 5.3.2, which were about  $5.801 \pm 0.225$ ,  $7.983 \pm 0.278$ , and  $11.147 \pm 0.369$  days after first detection for the  $B$ ,  $V$ , and  $I$  bands respectively. In contrast to the rise times for SNe with radioactively powered rise in Section 8.5, the rise times here for SNe with shock cooling emission powered rise are more consistent with KSP-ZN7090.

Indeed, Rubin et al. (2016) concludes that Type II SNe are “unlikely to be powered by radioactive decay or other central-engine models at early times”. Shock cooling emission seems like the more likely source. In addition, Gonzalez-Gaitan et al. (2015) mentions that most Type II SNe have steep rise times, indicating that shock cooling emission is the more likely source than radioactive decay. To conclude, we saw that KSP-ZN7090 was more compatible with a shock cooling emission model (Sapir & Waxman 2017), and that its rise times are consistent with those of Type II SNe with rise powered by shock cooling emission. Both of these points suggest that KSP-ZN7090 is a Type II SN with a rise likely powered by shock heated cooling rather than radioactive decay.

# Chapter 10

## Conclusion

### 10.1 Summary and Significance of Work

The main conclusions of this thesis can be summarized as follows:

1. KSP-ZN7090 was first detected by KMTNet as a new point source in a  $B$  band image taken on 2020 October 12 at 14:44 UTC (MJD = 59134.61389), at the location (R.A., decl.) =  $(21^{\text{h}}31^{\text{m}}3.05, -53^{\circ}55'49.91)$  (J2000). Images of KSP-ZN7090 at important epochs are shown in Figure 3.15.
2. The  $BVI$  light curves of KSP-ZN7090 were constructed using PSF photometry with subtracted images. Early images were stacked in order to get deeper limiting magnitudes, and the post-peak data was binned using a 24 hour rolling window with inverse-variance weighting in order to reduce spread in the data. Colour corrections and interstellar extinction corrections were applied to the light curves. KSP-ZN7090's final  $BVI$  light curves are shown in Figure 3.16.
3. KSP-ZN7090's host galaxy was estimated to be located at (R.A., decl.) =  $(21^{\text{h}}31^{\text{m}}2.86, -53^{\circ}55'50.75)$  (J2000), with an uncertainty of  $1.68''$  and  $1.00''$  in the R.A. and decl. respectively. The host galaxy was relatively faint, and its  $B$ ,  $V$ , and  $I$  band apparent magnitudes were estimated to be  $22.165 \pm 0.276$  mag,  $22.943 \pm 0.283$  mag, and  $21.773 \pm 0.112$  mag respectively.
4. By fitting polynomials to KSP-ZN7090's  $BVI$  light curves using Monte Carlo simulations, the peak epochs of KSP-ZN7090 were estimated to have occurred at  $5.610 \pm 0.187$ ,  $7.792 \pm 0.248$ , and  $10.956 \pm 0.347$  days after first detection for the  $B$ ,  $V$ , and  $I$  bands respectively.

5. By fitting a single power law simultaneously to KSP-ZN7090’s *BVI* light curves, KSP-ZN7090’s epoch of first light was estimated to have occurred at  $0.191 \pm 0.126$  days before the first detection, implying that KSP-ZN7090 was discovered  $< 1$  day after its explosion. The fitted power index was  $n = 0.285 \pm 0.068$ , which suggests that the rise of KSP-ZN7090’s light curve is likely powered by shock cooling emission.
6. Based on KSP-ZN7090’s *V* band light curve, KSP-ZN7090 can be photometrically classified as a Type II-L SN, according to the definition in [Faran et al. \(2014\)](#) for Type II-L SNe.
7. The method of blackbody fitting for constructing the bolometric light curve of KSP-ZN7090 was found to be unsuitable for KSP-ZN7090, due to observations in a limited number of bands.
8. The method of bolometric corrections was ultimately used to construct the bolometric light curve of KSP-ZN7090. This method works better than blackbody fitting. Bolometric correction coefficients from [Lyman et al. \(2013\)](#) produced better results than those from [Martinez et al. \(2021\)](#).
9. By comparing the slope of KSP-ZN7090’s *V* band light curve with values in the literature, it was concluded that KSP-ZN7090’s light curve has not reached nebular phase yet at the time of this work. As a result, most of the models in Section 2.8 could not be used yet to fit KSP-ZN7090’s bolometric light curve, and some analytic models had to be used instead. In addition, the comparison suggests that KSP-ZN7090’s light curve is in a cooling phase.
10. The analytic model from [Valenti et al. \(2007\)](#), for SNe with rise powered by radioactive decay, is incompatible with KSP-ZN7090. The resulting fitted physical parameters are inconsistent with Type II-L SNe.
11. The analytic model from [Sapir & Waxman \(2017\)](#), for SNe with rise powered by shock cooling emission, is more compatible with KSP-ZN7090. However, there is degeneracy between the ejecta mass and progenitor radius parameters as shown in the  $\chi^2/\text{dof}$  contour plots. The ejecta mass must be constrained first in order extract physical results from this model.
12. The rise times of KSP-ZN7090’s *BVI* light curves suggest that KSP-ZN7090’s early light curve is likely being powered primarily by shock cooling emission, and not by radioactive decay.

In this thesis, the *BVI* light curves and bolometric light curve of KSP-ZN7090 were constructed. The temporal parameters of KSP-ZN7090, such as the peak epoch and epoch of first light, were estimated. Estimates were made for the physical parameters of KSP-ZN7090, such as its Nickel-56 mass, ejecta mass, ejecta energy, and progenitor radius, but the analysis is not complete yet due to a lack of nebular phase data and spectroscopic analysis at the time of this work. Nevertheless, from the results, we can conclude that it is likely for KSP-ZN7090’s early light curve to be powered primarily by shock cooling emission, rather than the radioactive decay of Nickel-56. Ultimately, the work in this thesis has added another SN to the limited sample of Type II-L SNe. This information, in and of itself, is very valuable and is collectively useful in allowing other researchers to develop and constrain explosion models for CCSNe.

## 10.2 Future Work

The work in this thesis has laid a strong foundation for future analyses of KSP-ZN7090. One next step of this project would be to analyze the spectra of KSP-ZN7090 in order to confirm the redshift and photospheric velocity of KSP-ZN7090. In this work, only a rough inspection of the spectra was conducted, and the redshift was roughly estimated. With the redshift confirmed, the luminosity distance to KSP-ZN7090, and hence the bolometric light curve, would be more accurate. The photospheric velocity was used in both the [Valenti et al. \(2007\)](#) and [Sapir & Waxman \(2017\)](#) analytic models in this work, but was only assumed since the spectra was not yet analyzed. Obtaining a more accurate estimate of this value is a step that needs to be taken in order to determine the physical parameters of KSP-ZN7090.

Another next step of this project would be to extend KSP-ZN7090’s light curve into the nebular phase. Since it has been over 1.5 years (at the time of this work) since KSP-ZN7090 was first detected, KSP-ZN7090 is likely in its nebular phase. At this point, KSP-ZN7090 could appear very faint in images, but the nebular phase data could still be made useful by stacking images to get deeper limiting magnitudes and by binning data points together, as in the procedure in Section 3.6. The bolometric light curve could then be constructed with this nebular phase data, using the radiatively-/recombination-powered phase of [Lyman et al. \(2013\)](#) or the nebular/tail phase from [Martinez et al. \(2021\)](#). Once a bolometric light curve with the nebular phase is obtained, the models from Section 2.8 could then be fitted to the bolometric light curve in order to obtain the Nickel-56 mass, ejecta mass, and ejecta kinetic energy. Using these values, the [Sapir & Waxman \(2017\)](#) model could then be used to estimate the progenitor radius more accurately.

# Bibliography

- Afsariardchi, N., Moon, D.-S., Drout, M. R., et al. 2019, The Astrophysical Journal, 881, 22, doi: [10.3847/1538-4357/ab2be6](https://doi.org/10.3847/1538-4357/ab2be6)
- Anderson, J., & King, I. R. 2000, Publications of the Astronomical Society of the Pacific, 112, 1360, doi: [10.1086/316632](https://doi.org/10.1086/316632)
- Anderson, J. P., González-Gaitán, S., Hamuy, M., et al. 2014, The Astrophysical Journal, 786, 67, doi: [10.1088/0004-637x/786/1/67](https://doi.org/10.1088/0004-637x/786/1/67)
- Arcavi, I., Hosseinzadeh, G., Brown, P. J., et al. 2017, The Astrophysical Journal, 837, L2, doi: [10.3847/2041-8213/aa5be1](https://doi.org/10.3847/2041-8213/aa5be1)
- Arnett, W. D. 1980, The Astrophysical Journal, 237, 541, doi: [10.1086/157898](https://doi.org/10.1086/157898)
- Arnett, W. D., & Fu, A. 1989, The Astrophysical Journal, 340, 396, doi: [10.1086/167402](https://doi.org/10.1086/167402)
- Arnett, W. D. 1982, The Astrophysical Journal, 253, 785, doi: [10.1086/159681](https://doi.org/10.1086/159681)
- Barbon, R., Ciatti, F., & Rosino, L. 1979, Astronomy & Astrophysics, 72, 287
- Baron, E., & Cooperstein, J. 1990, The Astrophysical Journal, 353, 597, doi: [10.1086/168649](https://doi.org/10.1086/168649)
- Bazin, G., Palanque-Delabrouille, N., Rich, J., et al. 2009, Astronomy & Astrophysics, 499, 653, doi: [10.1051/0004-6361/200911847](https://doi.org/10.1051/0004-6361/200911847)
- Becker, A. 2015, HOTPANTS: High Order Transform of PSF ANd Template Subtraction.  
<http://ascl.net/1504.004>
- Ben-Ami, S., Gal-Yam, A., Filippenko, A. V., et al. 2012, The Astrophysical Journal, 760, L33, doi: [10.1088/2041-8205/760/2/133](https://doi.org/10.1088/2041-8205/760/2/133)
- Bersten, M. C., Benvenuto, O., & Hamuy, M. 2011, The Astrophysical Journal, 729, 61, doi: [10.1088/0004-637x/729/1/61](https://doi.org/10.1088/0004-637x/729/1/61)

## BIBLIOGRAPHY

---

- Bersten, M. C., & Hamuy, M. 2009, *The Astrophysical Journal*, 701, 200, doi: [10.1088/0004-637x/701/1/200](https://doi.org/10.1088/0004-637x/701/1/200)
- Bertin, E. 2006, Automatic Astrometric and Photometric Calibration with SCAMP, Tech. rep. <http://terapix.iap.fr>
- Bertin, E., Mellier, Y., Radovich, M., et al. 2002, in *Astronomical Society of the Pacific Conference Series*, Vol. 281, *Astronomical Data Analysis Software and Systems XI*, ed. D. A. Bohlender, D. Durand, & T. H. Handley, 228
- Bessell, M. S. 2005, *Annual Review of Astronomy and Astrophysics*, 43, 293, doi: [10.1146/annurev.astro.41.082801.100251](https://doi.org/10.1146/annurev.astro.41.082801.100251)
- Bessell, M. S., Castelli, F., & Plez, B. 1998, *Astronomy & Astrophysics*, 333, 231
- Bethe, H. A., & Wilson, J. R. 1985, *The Astrophysical Journal*, 295, 14, doi: [10.1086/163343](https://doi.org/10.1086/163343)
- Blinnikov, S. I., & Bartunov, O. S. 1993, *Astronomy & Astrophysics*, 273, 106
- Bose, S., Kumar, B., Misra, K., et al. 2015a, *Monthly Notices of the Royal Astronomical Society*, 455, 2712, doi: [10.1093/mnras/stv2351](https://doi.org/10.1093/mnras/stv2351)
- Bose, S., Sutaria, F., Kumar, B., et al. 2015b, *The Astrophysical Journal*, 806, 160, doi: [10.1088/0004-637x/806/2/160](https://doi.org/10.1088/0004-637x/806/2/160)
- Bose, S., Dong, S., Kochanek, C. S., et al. 2018, *The Astrophysical Journal*, 862, 107, doi: [10.3847/1538-4357/aacb35](https://doi.org/10.3847/1538-4357/aacb35)
- Calzavara, A. J., & Matzner, C. D. 2004, *Monthly Notices of the Royal Astronomical Society*, 351, 694, doi: [10.1111/j.1365-2966.2004.07818.x](https://doi.org/10.1111/j.1365-2966.2004.07818.x)
- Cano, Z. 2013, *Monthly Notices of the Royal Astronomical Society*, 434, 1098, doi: [10.1093/mnras/stt1048](https://doi.org/10.1093/mnras/stt1048)
- Carroll, B. W., & Ostlie, D. A. 2017, *An Introduction to Modern Astrophysics*, 2nd edn. (Cambridge, United Kingdom: Cambridge University Press), doi: [10.1017/9781108380980](https://doi.org/10.1017/9781108380980)
- Clocchiatti, A., & Wheeler, J. C. 1997, *The Astrophysical Journal*, 491, 375, doi: [10.1086/304961](https://doi.org/10.1086/304961)
- Colgate, S. A., & McKee, C. 1969, *The Astrophysical Journal*, 157, 623, doi: [10.1086/150102](https://doi.org/10.1086/150102)

## BIBLIOGRAPHY

---

- Colgate, S. A., & White, R. H. 1966, *The Astrophysical Journal*, 143, 626, doi: [10.1086/148549](https://doi.org/10.1086/148549)
- Copeland, E. J., Sami, M., & Tsujikawa, S. 2006, *International Journal of Modern Physics D*, 15, 1753, doi: [10.1142/s021827180600942x](https://doi.org/10.1142/s021827180600942x)
- Couch, S. M. 2017, *Philosophical Transactions of the Royal Society A: Mathematical, Physical and Engineering Sciences*, 375, 20160271, doi: [10.1098/rsta.2016.0271](https://doi.org/10.1098/rsta.2016.0271)
- Davis, T. M., & Lineweaver, C. H. 2004, *Publications of the Astronomical Society of Australia*, 21, 97, doi: [10.1071/as03040](https://doi.org/10.1071/as03040)
- Dessart, L., & Hillier, D. J. 2020, *Astronomy & Astrophysics*, 642, A33, doi: [10.1051/0004-6361/202038148](https://doi.org/10.1051/0004-6361/202038148)
- Elias-Rosa, N., Dyk, S. D. V., Li, W., et al. 2011, *The Astrophysical Journal*, 742, 6, doi: [10.1088/0004-637x/742/1/6](https://doi.org/10.1088/0004-637x/742/1/6)
- Faran, T., Nakar, E., & Poznanski, D. 2017, *Monthly Notices of the Royal Astronomical Society*, 473, 513, doi: [10.1093/mnras/stx2288](https://doi.org/10.1093/mnras/stx2288)
- Faran, T., Poznanski, D., Filippenko, A. V., et al. 2014, *Monthly Notices of the Royal Astronomical Society*, 445, 554, doi: [10.1093/mnras/stu1760](https://doi.org/10.1093/mnras/stu1760)
- Fassia, A., Meikle, W. P. S., Vacca, W. D., et al. 2000, *Monthly Notices of the Royal Astronomical Society*, 318, 1093, doi: [10.1046/j.1365-8711.2000.03797.x](https://doi.org/10.1046/j.1365-8711.2000.03797.x)
- Firth, R. E., Sullivan, M., Gal-Yam, A., et al. 2014, *Monthly Notices of the Royal Astronomical Society*, 446, 3895, doi: [10.1093/mnras/stu2314](https://doi.org/10.1093/mnras/stu2314)
- Fitzpatrick, E. L. 1999, *Publications of the Astronomical Society of the Pacific*, 111, 63, doi: [10.1086/316293](https://doi.org/10.1086/316293)
- Foglizzo, T., Kazeroni, R., Guilet, J., et al. 2015, *Publications of the Astronomical Society of Australia*, 32, doi: [10.1017/pasa.2015.9](https://doi.org/10.1017/pasa.2015.9)
- Foley, R. J., Fox, O. D., McCully, C., et al. 2014, *Monthly Notices of the Royal Astronomical Society*, 443, 2887, doi: [10.1093/mnras/stu1378](https://doi.org/10.1093/mnras/stu1378)
- Fukugita, M., Ichikawa, T., Gunn, J. E., et al. 1996, *The Astronomical Journal*, 111, 1748, doi: [10.1086/117915](https://doi.org/10.1086/117915)

## BIBLIOGRAPHY

---

- Gal-Yam, A., Arcavi, I., Ofek, E. O., et al. 2014, *Nature*, 509, 471, doi: [10.1038/nature13304](https://doi.org/10.1038/nature13304)
- Gall, E. E. E., Polshaw, J., Kotak, R., et al. 2015, *Astronomy & Astrophysics*, 582, A3, doi: [10.1051/0004-6361/201525868](https://doi.org/10.1051/0004-6361/201525868)
- Gonzalez-Gaitan, S., Tominaga, N., Molina, J., et al. 2015, *Monthly Notices of the Royal Astronomical Society*, 451, 2212, doi: [10.1093/mnras/stv1097](https://doi.org/10.1093/mnras/stv1097)
- Green, G. 2018, *The Journal of Open Source Software*, 3, 695, doi: [10.21105/joss.00695](https://doi.org/10.21105/joss.00695)
- Gutiérrez, C. P., Anderson, J. P., Hamuy, M., et al. 2017, *The Astrophysical Journal*, 850, 89, doi: [10.3847/1538-4357/aa8f52](https://doi.org/10.3847/1538-4357/aa8f52)
- Hamuy, M. 2003, *The Astrophysical Journal*, 582, 905, doi: [10.1086/344689](https://doi.org/10.1086/344689)
- Henden, A. A., Templeton, M., Terrell, D., et al. 2016, *VizieR Online Data Catalog*, II/336
- Hirata, K., Kajita, T., Koshiba, M., et al. 1987, *Physical Review Letters*, 58, 1490, doi: [10.1103/physrevlett.58.1490](https://doi.org/10.1103/physrevlett.58.1490)
- Hogg, D. W. 1999, Distance measures in cosmology, arXiv, doi: [10.48550/ARXIV.ASTRO-PH/9905116](https://arxiv.org/abs/astro-ph/9905116)
- Janka, H.-T. 2012, *Annual Review of Nuclear and Particle Science*, 62, 407, doi: [10.1146/annurev-nucl-102711-094901](https://doi.org/10.1146/annurev-nucl-102711-094901)
- Janka, H.-T., Langanke, K., Marek, A., Martínez-Pinedo, G., & Müller, B. 2007, *Physics Reports*, 442, 38, doi: <https://doi.org/10.1016/j.physrep.2007.02.002>
- Jerkstrand, A., Fransson, C., Maguire, K., et al. 2012, *Astronomy & Astrophysics*, 546, A28, doi: [10.1051/0004-6361/201219528](https://doi.org/10.1051/0004-6361/201219528)
- Joye, W. A., & Mandel, E. 2003, in *Astronomical Society of the Pacific Conference Series*, Vol. 295, *Astronomical Data Analysis Software and Systems XII*, ed. H. E. Payne, R. I. Jedrzejewski, & R. N. Hook, 489
- Kasen, D., & Woosley, S. E. 2009, *The Astrophysical Journal*, 703, 2205, doi: [10.1088/0004-637x/703/2/2205](https://doi.org/10.1088/0004-637x/703/2/2205)
- Kim, S. L., Lee, C. U., Park, B. G., et al. 2016, *Journal of the Korean Astronomical Society*, 49, 37, doi: [10.5303/JKAS.2016.49.1.37](https://doi.org/10.5303/JKAS.2016.49.1.37)

## BIBLIOGRAPHY

---

- Kirchner, J. 2006, Data Analysis Toolkit #12: Weighted averages and their uncertainties.  
[http://seismo.berkeley.edu/~kirchner/Toolkits/Toolkit\\_12.pdf](http://seismo.berkeley.edu/~kirchner/Toolkits/Toolkit_12.pdf)
- Komatsu, E., Dunkley, J., Nolta, M. R., et al. 2009, The Astrophysical Journal Supplement Series, 180, 330, doi: [10.1088/0067-0049/180/2/330](https://doi.org/10.1088/0067-0049/180/2/330)
- Laher, R. R., Gorjian, V., Rebull, L. M., et al. 2012, Publications of the Astronomical Society of the Pacific, 124, 737, doi: [10.1086/666883](https://doi.org/10.1086/666883)
- Larson, K. A. 2014, Publications of the Astronomical Society of the Pacific, 126, 27, doi: [10.1086/675071](https://doi.org/10.1086/675071)
- Lasker, B. M., Lattanzi, M. G., Mclean, B. J., et al. 2008, The Astronomical Journal, 136, 735, doi: [10.1088/0004-6256/136/2/735](https://doi.org/10.1088/0004-6256/136/2/735)
- Levesque, E. M., Massey, P., Olsen, K. A. G., et al. 2005, The Astrophysical Journal, 628, 973, doi: [10.1086/430901](https://doi.org/10.1086/430901)
- Li, W., Leaman, J., Chornock, R., et al. 2011, Monthly Notices of the Royal Astronomical Society, 412, 1441, doi: [10.1111/j.1365-2966.2011.18160.x](https://doi.org/10.1111/j.1365-2966.2011.18160.x)
- Lyman, J. D., Bersier, D., & James, P. A. 2013, Monthly Notices of the Royal Astronomical Society, 437, 3848, doi: [10.1093/mnras/stt2187](https://doi.org/10.1093/mnras/stt2187)
- Lyman, J. D., Bersier, D., James, P. A., et al. 2016, Monthly Notices of the Royal Astronomical Society, 457, 328, doi: [10.1093/mnras/stv2983](https://doi.org/10.1093/mnras/stv2983)
- Mamajek, E. E., Torres, G., Prsa, A., et al. 2015, IAU 2015 Resolution B2 on Recommended Zero Points for the Absolute and Apparent Bolometric Magnitude Scales, arXiv, doi: [10.48550/ARXIV.1510.06262](https://doi.org/10.48550/ARXIV.1510.06262)
- Martinez, L., Bersten, M. C., Anderson, J. P., et al. 2021, Astronomy & Astrophysics, doi: [10.1051/0004-6361/202142075](https://doi.org/10.1051/0004-6361/202142075)
- Matzner, C. D., & McKee, C. F. 1999, The Astrophysical Journal, 510, 379, doi: [10.1086/306571](https://doi.org/10.1086/306571)
- Mazzali, P. A., Ropke, F. K., Benetti, S., & Hillebrandt, W. 2007, Science, 315, 825, doi: [10.1126/science.1136259](https://doi.org/10.1126/science.1136259)
- Moffat, A. F. J. 1969, Astronomy & Astrophysics, 3, 455

## BIBLIOGRAPHY

---

- Moon, D.-S., Kim, S. C., Lee, J.-J., et al. 2016, in Society of Photo-Optical Instrumentation Engineers (SPIE) Conference Series, Vol. 9906, Ground-based and Airborne Telescopes VI, ed. H. J. Hall, R. Gilmozzi, & H. K. Marshall, 99064I, doi: [10.1117/12.2233921](https://doi.org/10.1117/12.2233921)
- Moon, D.-S., Ni, Y. Q., Drout, M. R., et al. 2021, *The Astrophysical Journal*, 910, 151, doi: [10.3847/1538-4357/abe466](https://doi.org/10.3847/1538-4357/abe466)
- Nagy, A. P., Ordasi, A., Vinkó, J., & Wheeler, J. C. 2014, *Astronomy & Astrophysics*, 571, A77, doi: [10.1051/0004-6361/201424237](https://doi.org/10.1051/0004-6361/201424237)
- Nakar, E., & Sari, R. 2010, *The Astrophysical Journal*, 725, 904, doi: [10.1088/0004-637x/725/1/904](https://doi.org/10.1088/0004-637x/725/1/904)
- Olivares E., F., Hamuy, M., Pignata, G., et al. 2010, *The Astrophysical Journal*, 715, 833, doi: [10.1088/0004-637x/715/2/833](https://doi.org/10.1088/0004-637x/715/2/833)
- Park, H. S., Moon, D.-S., Zaritsky, D., et al. 2017, *Astrophysical Journal*, 848, 19, doi: [10.3847/1538-4357/aa88ab](https://doi.org/10.3847/1538-4357/aa88ab)
- Parrag, E., Inserra, C., Schulze, S., et al. 2021, *Monthly Notices of the Royal Astronomical Society*, 506, 4819, doi: [10.1093/mnras/stab2074](https://doi.org/10.1093/mnras/stab2074)
- Patriarchi, P., Morbidelli, L., Perinotto, M., & Barbaro, G. 2001, *Astronomy & Astrophysics*, 372, 644, doi: [10.1051/0004-6361:20010496](https://doi.org/10.1051/0004-6361:20010496)
- Pejcha, O. 2020, in *Reviews in Frontiers of Modern Astrophysics* (Springer International Publishing), 189–211, doi: [10.1007/978-3-030-38509-5\\_7](https://doi.org/10.1007/978-3-030-38509-5_7)
- Piro, A. L., Haynie, A., & Yao, Y. 2021, *The Astrophysical Journal*, 909, 209, doi: [10.3847/1538-4357/abe2b1](https://doi.org/10.3847/1538-4357/abe2b1)
- Piro, A. L., & Nakar, E. 2013, *The Astrophysical Journal*, 769, 67, doi: [10.1088/0004-637x/769/1/67](https://doi.org/10.1088/0004-637x/769/1/67)
- Pogson, N. 1856, *Monthly Notices of the Royal Astronomical Society*, 17, 12, doi: [10.1093/mnras/17.1.12](https://doi.org/10.1093/mnras/17.1.12)
- Prša, A., Harmanec, P., Torres, G., et al. 2016, *The Astronomical Journal*, 152, 41, doi: [10.3847/0004-6256/152/2/41](https://doi.org/10.3847/0004-6256/152/2/41)
- Rabinak, I., & Waxman, E. 2011, *The Astrophysical Journal*, 728, 63, doi: [10.1088/0004-637x/728/1/63](https://doi.org/10.1088/0004-637x/728/1/63)

## BIBLIOGRAPHY

---

- Reynolds, T. M., Fraser, M., Mattila, S., et al. 2020, Monthly Notices of the Royal Astronomical Society, 493, 1761, doi: [10.1093/mnras/staa365](https://doi.org/10.1093/mnras/staa365)
- Riess, A. G., Filippenko, A. V., Challis, P., et al. 1998, The Astronomical Journal, 116, 1009, doi: [10.1086/300499](https://doi.org/10.1086/300499)
- Riess, A. G., Macri, L. M., Hoffmann, S. L., et al. 2016, The Astrophysical Journal, 826, 56, doi: [10.3847/0004-637x/826/1/56](https://doi.org/10.3847/0004-637x/826/1/56)
- Rubin, A., Gal-Yam, A., Cia, A. D., et al. 2016, The Astrophysical Journal, 820, 33, doi: [10.3847/0004-637x/820/1/33](https://doi.org/10.3847/0004-637x/820/1/33)
- Sanders, N. E., Soderberg, A. M., Gezari, S., et al. 2015, The Astrophysical Journal, 799, 208, doi: [10.1088/0004-637x/799/2/208](https://doi.org/10.1088/0004-637x/799/2/208)
- Sapir, N., & Waxman, E. 2017, The Astrophysical Journal, 838, 130, doi: [10.3847/1538-4357/aa64df](https://doi.org/10.3847/1538-4357/aa64df)
- Schlafly, E. F., & Finkbeiner, D. P. 2011, The Astrophysical Journal, 737, 103, doi: [10.1088/0004-637x/737/2/103](https://doi.org/10.1088/0004-637x/737/2/103)
- Schlegel, D. J., Finkbeiner, D. P., & Davis, M. 1998, The Astrophysical Journal, 500, 525, doi: [10.1086/305772](https://doi.org/10.1086/305772)
- Schultz, G. V., & Wiemer, W. 1975, Astronomy & Astrophysics, 43, 133
- Shappee, B. J., et al. 2018, The Astrophysical Journal, 870, 13, doi: [10.3847/1538-4357/aaec79](https://doi.org/10.3847/1538-4357/aaec79)
- Shussman, T., Waldman, R., & Nakar, E. 2016, Type II supernovae Early Light Curves. <https://arxiv.org/abs/1610.05323>
- Smartt, S. J. 2009, Annual Review of Astronomy and Astrophysics, 47, 63, doi: [10.1146/annurev-astro-082708-101737](https://doi.org/10.1146/annurev-astro-082708-101737)
- Smartt, S. J., Eldridge, J. J., Crockett, R. M., & Maund, J. R. 2009, Monthly Notices of the Royal Astronomical Society, 395, 1409, doi: [10.1111/j.1365-2966.2009.14506.x](https://doi.org/10.1111/j.1365-2966.2009.14506.x)
- Soumagnac, M. T., Ganot, N., Irani, I., et al. 2020, The Astrophysical Journal, 902, 6, doi: [10.3847/1538-4357/abb247](https://doi.org/10.3847/1538-4357/abb247)
- Spiro, S., Pastorello, A., Pumo, M. L., et al. 2014, Monthly Notices of the Royal Astronomical Society, 439, 2873, doi: [10.1093/mnras/stu156](https://doi.org/10.1093/mnras/stu156)

## BIBLIOGRAPHY

---

- Stetson, P. B. 1987, Publications of the Astronomical Society of the Pacific, 99, 191, doi: [10.1086/131977](https://doi.org/10.1086/131977)
- Sukhbold, T., Ertl, T., Woosley, S. E., Brown, J. M., & Janka, H.-T. 2016, The Astrophysical Journal, 821, 38, doi: [10.3847/0004-637x/821/1/38](https://doi.org/10.3847/0004-637x/821/1/38)
- Suntzeff, N. B., Phillips, M. M., Depoy, D. L., Elias, J. H., & Walker, A. R. 1991, The Astronomical Journal, 102, 1118, doi: [10.1086/115938](https://doi.org/10.1086/115938)
- Tartaglia, L., Fraser, M., Sand, D. J., et al. 2017, The Astrophysical Journal, 836, L12, doi: [10.3847/2041-8213/aa5c7f](https://doi.org/10.3847/2041-8213/aa5c7f)
- Tartaglia, L., Sand, D. J., Groh, J. H., et al. 2021, The Astrophysical Journal, 907, 52, doi: [10.3847/1538-4357/abca8a](https://doi.org/10.3847/1538-4357/abca8a)
- Terreran, G., Jerkstrand, A., Benetti, S., et al. 2016, Monthly Notices of the Royal Astronomical Society, 462, 137, doi: [10.1093/mnras/stw1591](https://doi.org/10.1093/mnras/stw1591)
- Terreran, G., Jacobson-Galán, W. V., Groh, J. H., et al. 2022, The Astrophysical Journal, 926, 20, doi: [10.3847/1538-4357/ac3820](https://doi.org/10.3847/1538-4357/ac3820)
- Tiesinga, E., Mohr, P. J., Newell, D. B., & Taylor, B. N. 2021, Reviews of Modern Physics, 93, doi: [10.1103/revmodphys.93.025010](https://doi.org/10.1103/revmodphys.93.025010)
- Toy, V. L., Cenko, S. B., Silverman, J. M., et al. 2016, The Astrophysical Journal, 818, 79, doi: [10.3847/0004-637x/818/1/79](https://doi.org/10.3847/0004-637x/818/1/79)
- Triggs, B., McLauchlan, P. F., Hartley, R. I., & Fitzgibbon, A. W. 2000, in Vision Algorithms: Theory and Practice (Springer Berlin Heidelberg), 298–372, doi: [10.1007/3-540-44480-7\\_21](https://doi.org/10.1007/3-540-44480-7_21)
- Trujillo, I., Aguerri, J., Cepa, J., & Gutiérrez, C. 2001, Monthly Notices of the Royal Astronomical Society, 328, 977, doi: [10.1046/j.1365-8711.2001.04937.x](https://doi.org/10.1046/j.1365-8711.2001.04937.x)
- Truran, J. W., Glasner, A. S., & Kim, Y. 2012, Journal of Physics: Conference Series, 337, 012040, doi: [10.1088/1742-6596/337/1/012040](https://doi.org/10.1088/1742-6596/337/1/012040)
- Turatto, M. 2003, in Supernovae and Gamma-Ray Bursters (Springer Berlin Heidelberg), 21–36, doi: [10.1007/3-540-45863-8\\_3](https://doi.org/10.1007/3-540-45863-8_3)
- Ugliano, M., Janka, H.-T., Marek, A., & Arcones, A. 2012, The Astrophysical Journal, 757, 69, doi: [10.1088/0004-637x/757/1/69](https://doi.org/10.1088/0004-637x/757/1/69)

## BIBLIOGRAPHY

---

Valenti, S., Benetti, S., Cappellaro, E., et al. 2007, Monthly Notices of the Royal Astronomical Society, 383, 1485, doi: [10.1111/j.1365-2966.2007.12647.x](https://doi.org/10.1111/j.1365-2966.2007.12647.x)

Weaver, T. A., Zimmerman, G. B., & Woosley, S. E. 1978, The Astrophysical Journal, 225, 1021, doi: [10.1086/156569](https://doi.org/10.1086/156569)

Willmer, C. N. A. 2018, The Astrophysical Journal Supplement Series, 236, 47, doi: [10.3847/1538-4365/aabfdf](https://doi.org/10.3847/1538-4365/aabfdf)

Woosley, S. E., Heger, A., & Weaver, T. A. 2002, Reviews of Modern Physics, 74, 1015, doi: [10.1103/revmodphys.74.1015](https://doi.org/10.1103/revmodphys.74.1015)

Zheng, W., Kelly, P. L., & Filippenko, A. V. 2017, The Astrophysical Journal, 848, 66, doi: [10.3847/1538-4357/aa8b19](https://doi.org/10.3847/1538-4357/aa8b19)

This page intentionally left blank.

